ALMA MATER STUDIORUM - UNIVERSITÀ DI BOLOGNA

SCUOLA DI INGEGNERIA E ARCHITETTURA

DIPARTIMENTO di
INGEGNERIA DELL'ENERGIA ELETTRICA E DELL'INFORMAZIONE
"Guglielmo Marconi"
DEI

CORSO DI LAUREA MAGISTRALE IN TELECOMMUNICATIONS ENGINEERING

TESI DI LAUREA
in
Technologies and Applications of Wireless Power Transfer M

PRECISE NEAR-FIELD FOCUSING EXPLOITING BESSEL BEAM LAUNCHERS FOR WIRELESS POWER TRANSFER AT MILLIMETER WAVES

CANDIDATO

Augello Elisa

RELATORE

Chiar.ma Prof.ssa Alessandra Costanzo

CORRELATORI

Prof. Ing. Diego Masotti
Dott. Ing. Francesca Benassi
Dott. Enrico Fazzini

Anno Accademico
2020/2021

Sessione
III

Chapter 1: Introduction

The 19th century was marked by the emergence of many theories regarding electrical energy transmission. The Ampère's circuital law dated 1862 states that an electric current flowing through a closed loop generates a magnetic field. Michael Faraday in 1831 defined the law of induction, showing how a magnetic field, interacting with an electric circuit, gives rise to an electromotive force. Many other experiments were conducted in the field of wireless energy transmission, but it was only in 1864 that James Clerk Maxwell with his Maxwell's equations lays the foundation of the electromagnetism by unifying the laws of electricity and magnetism. Maxwell's equations are the keystones of the electromagnetism, explaining the electromagnetic wireless energy transfer through the electromagnetic induction.

At the end of the century, Nikola Tesla started some experiments regarding wireless transmission of power for large distances, building the so-called Tesla coils. Meanwhile, while Tesla was focused on the transmission of energy, Guglielmo Marconi started experimenting the wireless propagation to perform the first transmission of information introducing the "wireless telegraphy". It was only in the second half of the 20th century that the technology improvements allowed the development of real-world applications. Wireless Power Transfer has the objective of overcoming the limits of wired solutions, resulting to be more effective in many applications, more economical and easier to maintain. Nowadays, thanks to its multiple advantages Wireless Power Transfer is one of the technologies that will impact most the next years. The range of applications is broad, spacing from sensor networks in IoT systems, where WPT solves the problem of energy supply, to military or industrial applications. The wireless charge of vehicles, drones, and other electronics devices is also a hot topic nowadays. Wireless Power Transfer is of fundamental importance also in the medical field, in particular when related to biomedical wearable and implantable devices. In fact, the major drawback of medical implantable devices, is their battery

life, which is limited in time. Differently from wearable medical devices that may be designed to have a replaceable battery, for implantable devices the embedded battery needs to be surgically removed in order to be replaced. This represents a risky medical procedure for the patient and a cost for the sanitary system. In this optic, WPT can be exploited for the energy recharge without the necessity of an invasive intervention. For this kind of applications, miniaturization of the implanted device must be a key point to be addressed, but also the impact of the biological tissues on the electromagnetic propagation, and vice-versa, must be accounted. Furthermore, when exploiting electromagnetic waves for powering wearable or implantable devices, the entire design must be in compliance with the safety regulations.

Within this framework, the objective of this thesis is to study a Wireless Power Transfer link involving a particular type of antenna working in near-field, which is able to generate focused energy beams providing good energy transfer properties.

This master thesis has been conducted in the framework of the Research Project of National Relevance (PRIN) WPT4WID ("Wireless Power Transfer for Wearable and Implantable Devices'), and has led to two scientific articles:

- F. Benassi, W. Fuscaldo, D. Masotti, A. Galli and A. Costanzo, "Wireless Power Transfer in the Radiative Near-field Through Resonant Bessel-Beam Launchers at Millimeter Waves," *2021 IEEE Wireless Power Transfer Conference (WPTC)*, 2021, pp. 1-4, doi: 10.1109/WPTC51349.2021.9458226.
- F. Benassi, F. Walter, N. Edoardo, P. Giacomo, A. Elisa, M. Diego, B. Paolo, G. Alessandro, and C. Alessandra, "Comparison between Hybrid and TM-polarized Bessel-beam launchers for wireless power transfer in the radiative near-field at millimeter waves," in *Eur. Microw. Conf. (EuMC 2021)*, 2022, p. [Accepted paper]

1.1 Wireless Power Transfer

A generic Wireless Power Transfer link implies the transmission of energy from source to load without the support of any conductive wire. Depending on the distance between the transmitting and receiving part the functioning principles are different, therefore a first classification of WPT systems can be made in terms of Far-Field and Near-field systems.

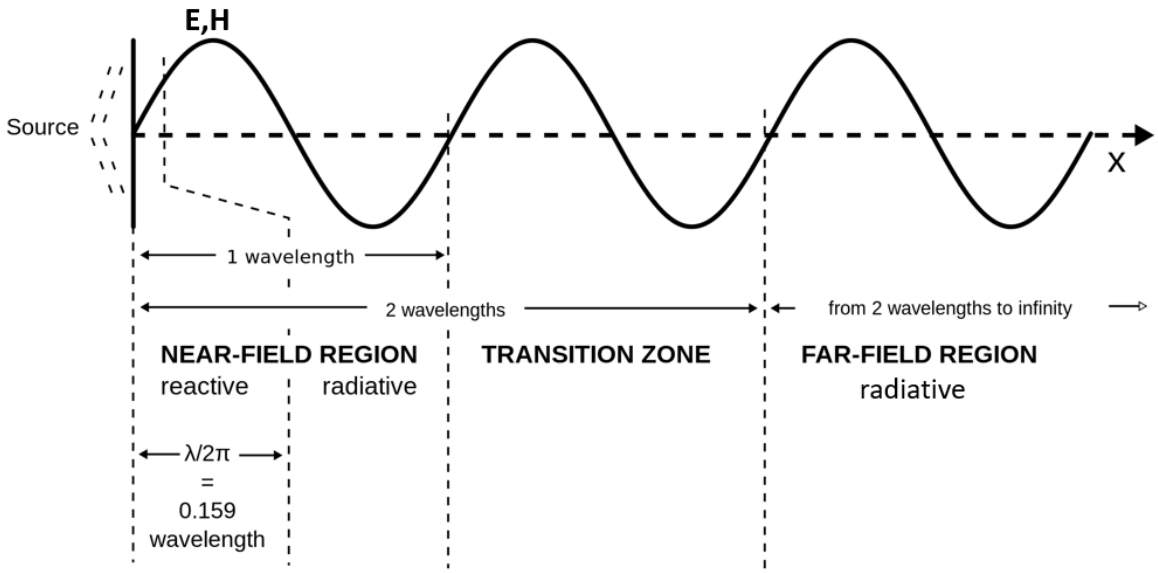

***Figure 1.1.1**: Region of electromagnetic field around the antenna.*

For electromagnetically short antennas (shorter than half of the operating wavelength), the limit between Near Field and Far Field can be expressed in terms of distance d from the radiating source with respect to the wavelength λ as in Fig. 1.1.1. The near field reactive region is for $d \ll \lambda$ and this is the region in close proximity to the antenna, whereas up to $d = \lambda$ the near-field is radiative (Fresnel region). The transition between near-field and far field happens in a smooth way, with $d = 2\lambda$ delimiting the starting region of Far-Field.

In the reactive near-field zone, the power transfer is achieved through electromagnetic induction, generally using two coils that couple to each other generating a strong magnetic flux between them. The links are based on a strong interaction between transmitting and receiving coils and, being a purely reactive region, the power is sent back if the receiver is absent. The oscillating fields remain confined close to the coupling devices and the power generated is usually non-directive, subject to an amplitude decay of $1/d^3$.

In radiative Far-Field WPT the energy is carried by the electromagnetic propagation of the fields, and, differently from near-field reactive links, there is no interaction between transmitting and receiving antenna. The presence of the receiver does not affect the electromagnetic situation. The amplitude decay of EM fields in this region is less sharp, going as $1/d$, therefore these links are used for larger distances at the expense of lower received power.

Most WPT systems in literature are designed for far-field or reactive near-field, that are respectively limited by efficiency and by reached distance.

The radiative near-field, also called Fresnel region, is the region where reactive fields components are no longer present since the distance from the antenna is large enough, and radiating fields starts to emerge. This is the operating region of the WPT system design and analyzed in this thesis.

A Wireless Power Transfer system is usually characterized in terms of efficiency, with the main goal of maximizing the DC power delivered to the load.

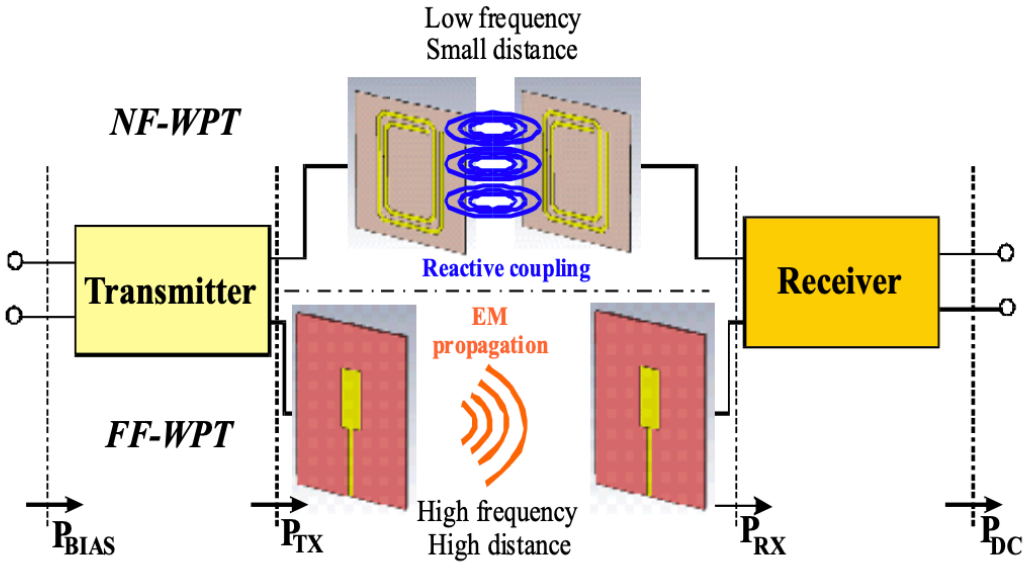

***Figure 1.1.2**: Block scheme of a Wireless Power Transfer link [1].*

The WPT system can be seen as the composition of three blocks, each of which has its definition of efficiency, as reported in Figure 1.1.2 [1];

- η_{DC-RF} quantify the efficiency of the transmitter to convert the DC power provided by the generator in RF power to be transmitted. It is the ratio between P_{TX} power available at transmitting antenna (for far-field) or coil (for near-field) and P_{BIAS} DC power provided.
- η_{RF-RF} is the efficiency of the wireless link. In wireless power transfer links, the channel may be very different depending on the specific application, therefore, it must be properly characterized. It is the ratio between P_{RX} power received by the receiving antenna/coil and P_{TX}.
- η_{RF-DC} is the conversion efficiency of the rectifying circuit and is defined as the ratio between the P_{DC} , DC-power delivered to the load, and P_{RX}. It is important to specify that a system that embeds the receiving antenna together with the matching circuit and the rectifier is called “Rectenna”, showed in Figure 1.1.3. The rectifier is composed of nonlinear components, that are fundamental in WPT system since their non-linearities are exploited to generate the DC output, but at

the same time produce some losses, thus the overall circuit, including the matching network, needs to be accurately designed and optimized.

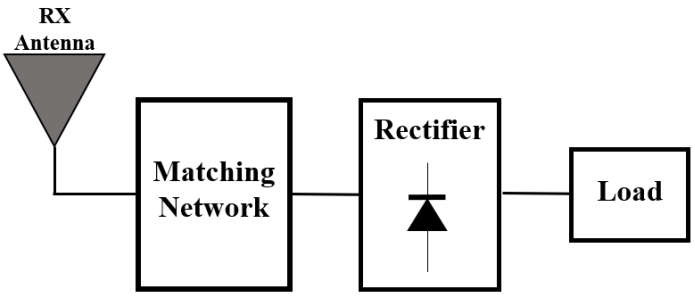

***Figure 1.1.3**: Rectenna block scheme.*

The total efficiency of the link, also known as Power Transfer Efficiency (PTE), will be the combination of these, taking into account the losses coming from the different blocks [1]:

$$\eta_{LINK} = \eta_{DC-RF} \cdot \eta_{RF-RF} \cdot \eta_{RF-DC} = \frac{P_{TX}}{P_{BIAS}} \cdot \frac{P_{RX}}{P_{TX}} \cdot \frac{P_{LOAD}}{P_{RX}}. \qquad (1.1)$$

Among different ways to perform wireless power transfer, one that has been investigated and implemented in the last years makes use of non-diffractive beams.
It is known from the Huygens-Fresnel principle that dispersion and diffraction affect any kind of wave. This results to be a problem any time the goal is to maintain the wave spatially confined along the transverse direction for a given distance, as required in wireless power transfer applications where the majority of the power must be delivered to the receiver. With the increasing progress in the electromagnetic fields area, some solutions that are less affected by dispersion and diffraction have been found and extensively studied. Indeed, even if it is possible to limit these phenomena, having a completely diffraction-free solution is physically impossible. A non-diffractive wave (also known as localized wave) is a solution that exists from a theoretical point of view, but it would require an infinite source of energy to be realized. Among the non-

diffractive solutions one of particular interest is related to Bessel Beams, that are ideal beam-like solutions of the Helmholtz equation, with remarkable properties that make them suitable for near-field wireless power transfer applications. They became widely used in the early 1990s when their generation from finite apertures was demonstrated. Bessel beams in their ideal form are non-diffractive, meaning that they never diverge during propagation, but this characteristic will be possible only in the presence of an infinite power source, making this unfeasible in real-case solutions. In practical realizations Bessel Beams are generated over finite apertures and they are able stay focused over a large, but limited, range called diffraction-free range.

Another important property is their self-healing capability, even when the wave is partially obstructed by an obstacle it will regenerate itself after a given distance.

To better understand the properties of Bessel Beams it is possible to make a comparison with another widespread class of beams, such as Gaussian Beams. In contrast to Bessel Beams, Gaussian Beams are non-localized and diffractive solutions. Gaussian Beams stay focused over a given propagation range after which they diverge.

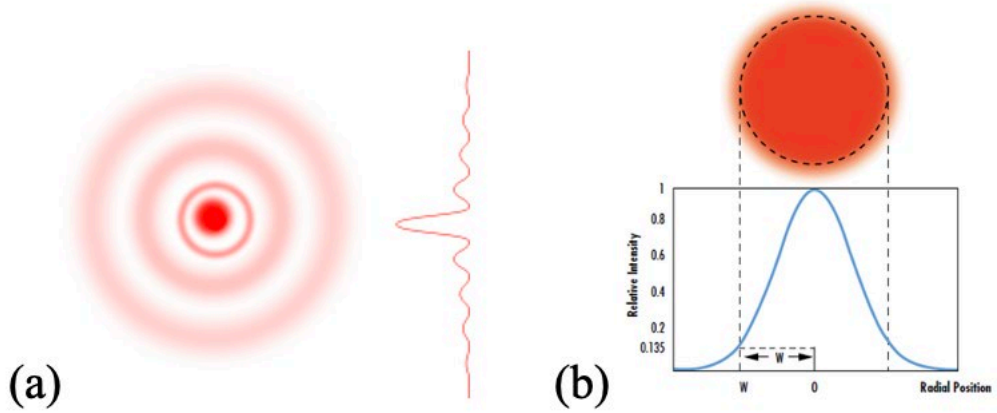

Figure 1.1.4*: Cross section of the energy distribution of (a) Bessel Beams (non diffractive) and (b) Gaussian Beams (diffractive)*

From the cross section of the energy distribution, in Figure 1.1.4, it can be observed that Bessel Beams are composed of concentric rings, each ring theoretically carrying the same amount of energy. This is the reason why the energy carried in the central

lobe is a small portion of the total energy, while boasting efficient focusing capabilities Gaussian Beams instead carry most of the energy in the main lobe, but even if their initial distribution is more efficient, due to diffractive spreading, they can cover smaller distances. Bessel beams are able to cover much larger distances at the expense of lower power efficiency.

1.2 State of the Art

WPT applications in millimeter-wave (mm-Wave) attract a significant interest for different reasons, one of which is the broad spectrum available. Systems realized at mm-Wave allow a remarkable miniaturization which is highly required on the market, especially at the receiver side [2]. Operating at 30-300 GHz the antenna can have dimensions comparable to its wavelength and behave efficiently, ensuring, at the same time, compactness, and miniaturization. The necessity of power supplies of compact dimensions regards not only wearable solutions, but also a variety of applications such as sensors of future Internet of Things (IoT) networks, whose dimensions are in the order of mm [2]. However, the challenge of working at these frequencies is related to the rectifying circuit: most of diodes are close to their cut-off frequency, and there are relevant parasitic losses coming from package and other components limiting the power conversion efficiency of the rectifier [2].

One example of mm-Wave antenna used for power charge of devices is presented in [3]. The antenna proposed has a grid structure and works at 60GHz, allowing high levels of miniaturization. In transmission, a 2x2 array is used. The array is integrated with a chip and prototype is shown in Figure 1.2.1. On the receiver side, the single antenna is used to keep the dimension of the receiver smaller.

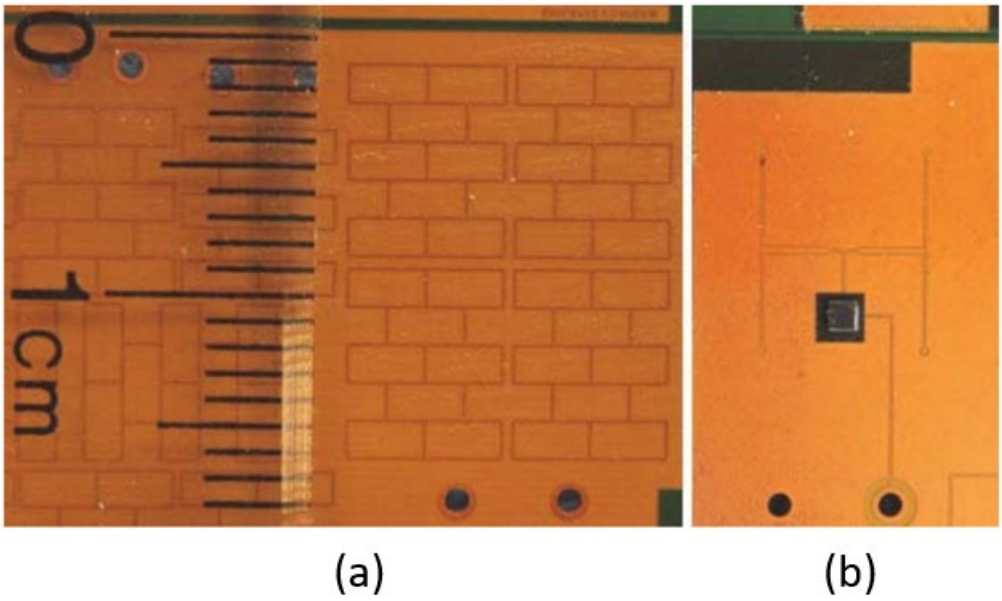

***Figure 1.2.1**: Front (a) and back (b) view of the 2x2 array transmitting antenna [3].*

Working at such high frequencies allows for using arrays of antennas that reach high gain and high directivity, while keeping a very compact size. The antenna is able to charge devices that consume up to 1mW and it demonstrates to reach a good trade-off between efficiency and dimensions [3]. However, the link is designed to work up to 4 cm that, for this specific antenna, is already considered far-field region, therefore constrained by Friis equation.

A variety of works both for Far-field and Near-Field applications are reported in [4]. Far-field WPT links typically shows very low efficiencies, and the allowed power density is limited by stringent safety standards. They are suitable for applications where very low received power is required, as sensor networks, or where large dimensions of the antenna can be accepted, for instance solar panels. Because of these limitations, the focus is moved to Near-Field applications. The systems implemented in reactive Near-Field typically imply the use of two coils both in transmission and reception. The reachable distance however is greatly limited. In this work [4], an example of coils operating in the midrange with a self-resonance frequency of 1.53 MHz is presented and the setup is shown in Figure 1.2.2.

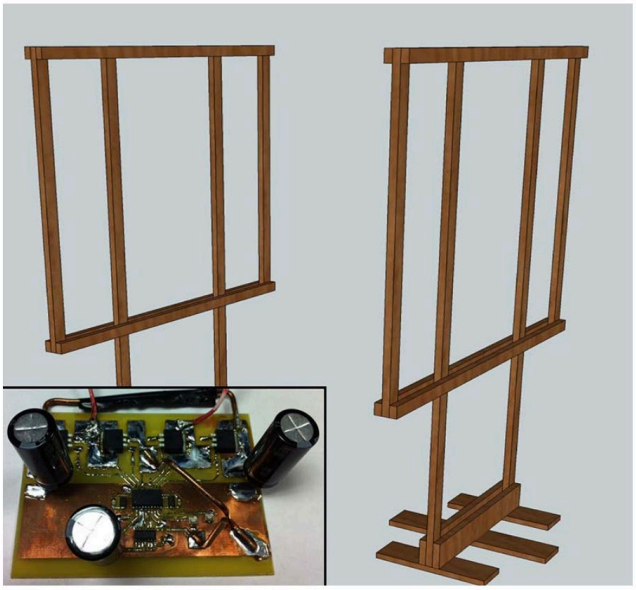

***Figure 1.2.2**: Setup of the WPT link with two 1 m square coils [4].*

The coils have dimension of 1 m^2 and are wounded around two wooden forms. They show good performances transmitting 100 W of power in 1 m air gap, however, to reach these results, dimensions are significantly increased. This solution is not feasible for many applications, such as wearable systems where a high level of miniaturization is required, at least for the receiver side

Working instead in the radiative near-field shows twofold advantages: the range of operating distance is larger with respect to coil-based links, and the safety regulations are not as stringent as in far-field links, reaching higher efficiencies with respect to the latter ones.

One example of application in the Fresnel zone is reported in [5]. Here a metasurface aperture is used, controlling the phase and amplitude of each radiating element to simulate the functionality of a diffractive optical lens to generate a focused beam. Metasurface antennas are passive devices, therefore consume very low power. However, the beam generated in this work still has a diffractive nature.

In the literature, several works describing Wireless Power Transfer implementations exploiting non-diffractive Bessel Beams are present. However, most of them use lower frequencies with respect to millimeter waves. For the sake of an efficient analysis in

the frequencies of interest, the vectorial nature of the electromagnetic field must be taken into account; for this reason, all the techniques to realize Bessel Beams for optics purposes using lens, holograms, etc. are not investigated. This thesis work is focused on applications at microwaves, useful for our field of application.

In [6], a WPT link with planar Bessel Beam Launchers is validated and realized through an electrically thin radial waveguide covered by an impedance sheet and excited by a coaxial feed. The resonant system is based on leaky modes and works at the operating frequency of 10 GHz. A similar structure is further analyzed in [7] and represented in Figure 1.2.3.

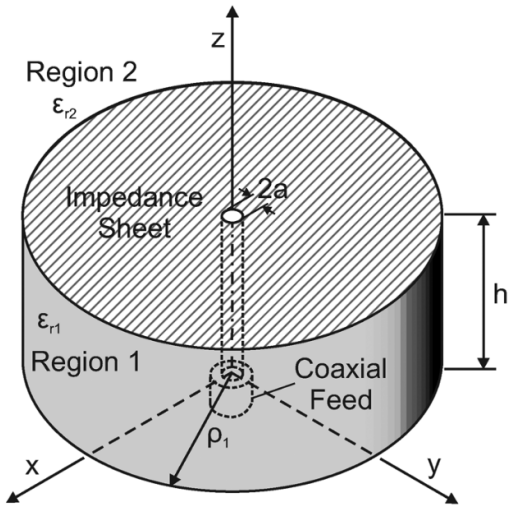

***Figure 1.2.1**: Bessel Beam Launcher realized with radial waveguide and coaxial cable feeding [7].*

The excited mode is a TM and, even in this case, the frequency of operation is 10 GHz. Such frequencies, however, do not allow to reach the targeted level of miniaturization. Another problem of this kind of structures is that, working in single mode operation, their system thickness, intended as separation between the ground plane and the impedance sheet, is much smaller than the operating wavelength. This is not a problem working in the X-band (8-12 GHz), but it leads to some problem when the structure is scaled at mm-Waves: the waveguide thickness becomes extremely small leading to high ohmic losses and to mechanical challenges for the implementation [8]. To overcome these limits in [8] a different type of structure is presented working in the

frequency range of 38-39.5 GHz. The Bessel Beam Launcher proposed is still based on a leaky radial waveguide but with a larger thickness separating the impedance sheet and the ground plane, keeping a coaxial cable as feeder. The thickness of the order of half wavelength allows the excitation of higher – order TM leaky modes. A prototype of this BB Launcher is reported in Figure 1.2.4 (a), fabricated by means of PCB (Printed Circuit Board) process.

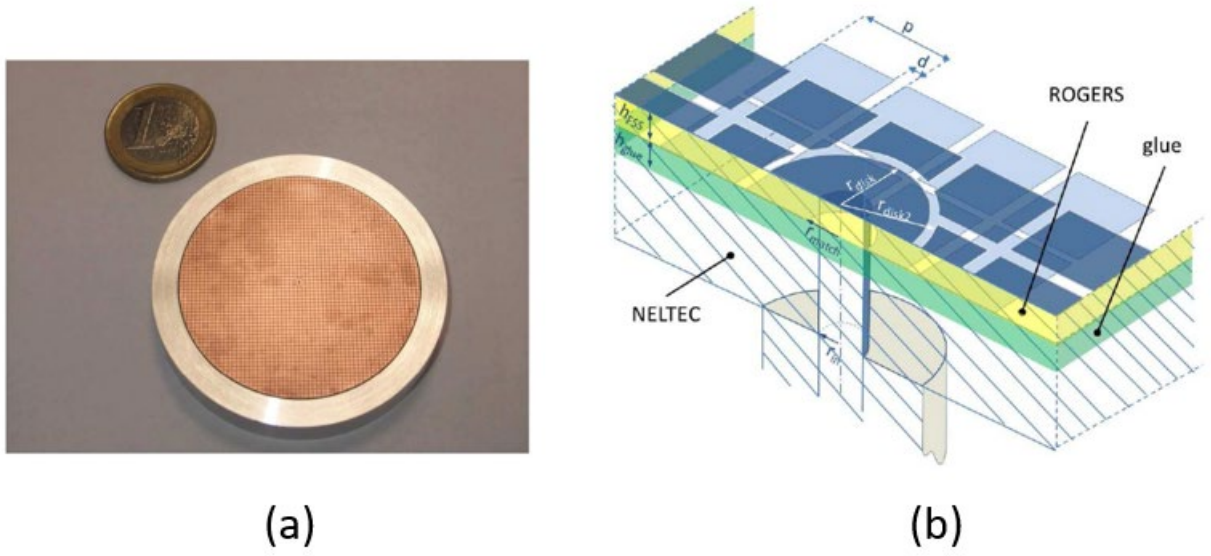

***Figure 1.2.2**: Prototype of the Bessel Beam Launcher at 60 GHz (a) and details of the impedance surface (b) [8].*

The impedance sheet is realized with a 2D array of squared metallic patches, represented in Figure 1.2.4 (b), with an antenna radius of 22.3 mm. This structure radiates a z-component of the electric field following the zeroth- order Bessel function, showing a diffraction range of approximately 1.5 cm, as reported in Fig.1.2.5.

The link budget of this kind of structure, as well as the conversion efficiency of the rectifying circuitry, is furtherly examined in [9], showing satisfying results up to a distance of 4 cm between the transmitter and the receiver. One way to generate Bessel Beams is to use an aperture antenna, as described in [10]: when the aperture distribution is described by a real-argument cylindrical function then it gives rise to classical Bessel Beams. On the other hand, when the argument is complex, meaning that there is some attenuation, we talk about Leaky-Wave Bessel-Beams. The aperture distribution for an

ideal Bessel Beam is proportional to $H_0^{(1)}(k_\rho \rho)$ zeroth-order Hankel function with ρ radial coordinate and k_ρ the real positive radial wavenumber [10].

Hankel functions are solutions of the Bessel's differential equation, representing outward and inward propagating cylindrical waves.

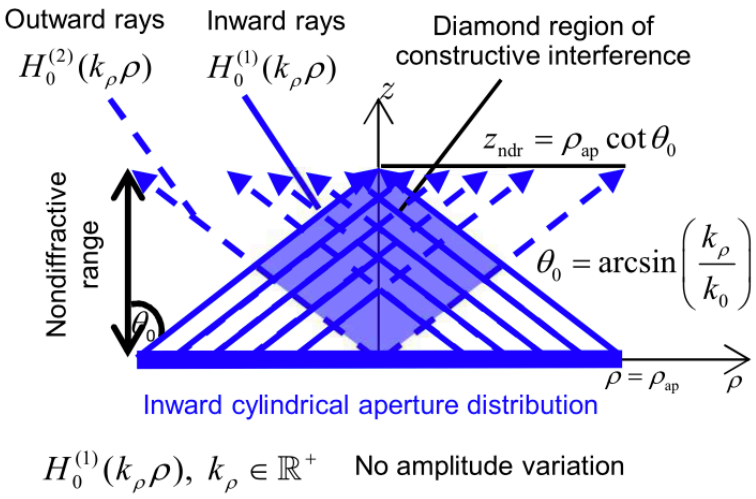

***Figure 1.2.5**: Ray-optics representation of classical Bessel Beams [10].*

Through constructive interference of rays, the Bessel Beam is created over a diamond-shaped region whose vertices define the non-diffractive range, as showed in Figure 1.2.5. Zeroth-order Hankel functions of first kind represent the wanted inward waves along which there is no amplitude variation. In [10], together with traditional Bessel Beams, also Leaky Waves Bessel Beams and Bessel Gauss Beams are analyzed. The aperture distribution in this case has an additional term describing an exponential decay of the amplitude [10], varying radially with an attenuation of the field in the direction of propagation. The advantage of using leaky waves is that the aperture distribution can be modulated in amplitude to reach the desired one.

Bessel Gauss Beams are realized as a trade-off between classical Bessel Beams and classical Gauss Beams, to combine their advantages in terms of power efficiency and covered distances. Bessel Gauss Beams provide a reduced oscillation of the electric field on the z-axis as well as reduced side lobes intensity. These advantages come at the expense of a lower non-diffraction range, compared to the one obtained with Bessel

Beams. To investigate the properties of these beams the source proposed in this work [10] is a Vertical Electrical Dipole (VED) exciting a TM mode. Subsequently, by placing a specific type of radially periodic grating on top, the backward waves are excited to have a Gauss Bessel Leaky Wave aperture. The periodicity of the gratings is relaxed according to a Gaussian decay along the radial section, to generate Bessel Gauss beam. Structure reported in Fig. 1.2.6.

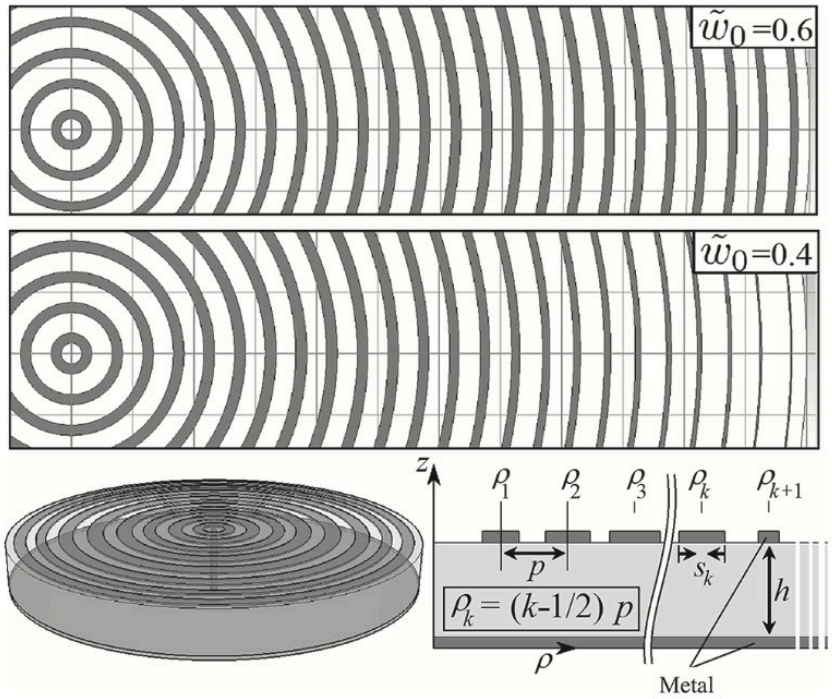

Figure 1.2.6*: Planar Leaky Wave structure that radiates a Bessel Gauss Beam. Different periodicity for different beam waist of the beam radiated [10].*

The operating frequency is set to 18 GHz with a radius of the antenna of 234 mm and 24 microstrip rings. Another way to generate Bessel Beam is through a grid structure printed on a dielectric substrate as reported in [11]. In this work the operating frequency is 5.8 GHz, and a TE-polarized cylindrical leaky wave is excited, so that the magnetic field along the direction of propagation will present the typical shape of a zero-order Bessel function while the other non-null components of electric and magnetic field will behave as first-order Bessel function. Also, being these fields composed of leaky

waves, there is an attenuation factor along the z-axis. In Figure 1.2.7 is reported the structure of the antenna:

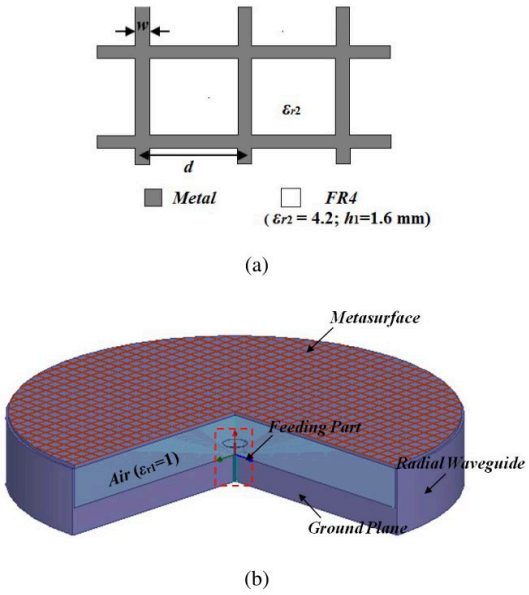

Figure 1.2.7: *(a) Top view of the grid structure for the sheet. (b) Antenna structure [11].*

The impedance sheet must be properly designed with closed formulas to work at a given radial wavenumber, and it has to be a capacitive sheet if a TM mode is wanted, otherwise an inductive sheet for the case of TE mode. The excitation is done with a quasi-loop shaped structure capable of exciting a TE polarization. The radial waveguide shows a grid metasurface representing the inductive sheet, made of FR-4 substrate with a permittivity of 4.2. Under the metasurface, there is a part which is air-filled and successively the ground plane. By using the transverse resonance approach, the dispersion equation can be derived [11], from which a closed expression that relates the reactance and the cavity height is obtained [11]. In this way, the height that ensures a proper surface impedance with real reactance results to be 30.6 mm. The choice of the antenna radius is fundamental for the distribution of the Bessel function over the z-component of the magnetic field. By choosing a truncation of the zeroth-order Bessel function at third zero, the radius is 139 mm, resulting in a theoretical non diffractive range of 186 mm ($3.6\lambda_0$) and a Null-To-Null Beamwidth of 66 mm ($1.28\lambda_0$). Periodicity and width of the grid structure are adjusted through electromagnetic

simulations with HFSS to achieve the required radial wavenumber. The prototype is realized, showed in Figure 1.2.8 with a quasi-loop excitation placed at an offset distance from the center to obtain a better distribution of the magnetic field.

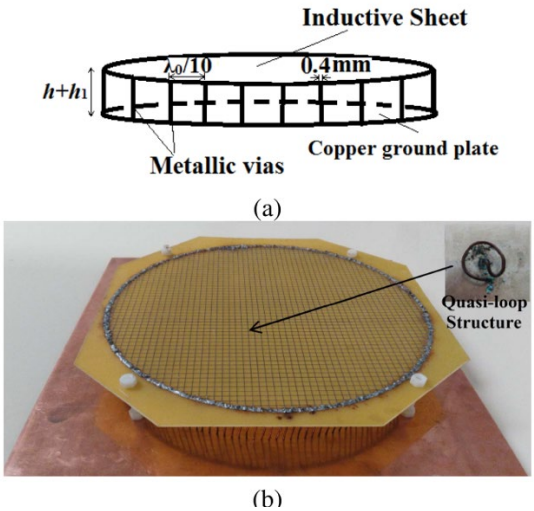

***Figure 1.2.8**:(a) External profile of the antenna. (b) Prototype of the fabricated antenna [11].*

Finally, in the literature research activities focused on transforming a Bessel Gauss Beam in a Bessel Beam that fulfills some requirements are present [12].
Here low-profile metasurfaces are fabricated using printed-circuit-board processes in order to control phase and polarization, rather than involving bulky technologies such as lenses. Two metasurfaces are used [12]:

- Linear – to – Bessel: transform a linearly polarized Gaussian beam in a TE/TM-polarized Bessel beam.
- Circular – to – Bessel: transform a left-hand circularly polarized Gaussian beam in a TM-polarized Bessel beam.

To realize the required phase and polarization control, the metasurfaces behave as anisotropic sheet admittances varying their properties along the radial direction, piled up in the direction of propagation of the beam.

Chapter 2: Bessel Beam Launchers Design

In the last years, diffraction-free beams have become popular in different fields of application thanks to their remarkable properties like focusing, self-healing, and limited diffraction. Bessel Beam Launchers can definitely be exploited in the field of wireless power transfer, especially when high-focusing and precision are required. through the realization of. In this chapter, a brief introduction on Leaky wave antennas delineates the theoretical framework in which the project is developed, subsequently the mathematical procedure to design these structures is reported, paving the way for a detailed description of the realized antenna.

2.1 Theoretical Framework

Before starting the analytical description that lies behind Bessel Beam Launchers, some basic concepts regarding Leaky wave Antennas are needed.

Leaky waves became popular over the second half of the 20th century, especially in the field of microwave applications. A.A. Oliner in the 60's defines rigorously the leaky wave theory, giving an important contribution to the development of the mathematical description of this kind of structures. Generally speaking, guided-wave structures can be categorized as *open* and *closed*, but also intermediate cases, such as *partially open,* can be counted. The *open* or *partially open* structures are characterized by a progressive wave leakage along the propagation direction. This leakage strictly depends on the antenna geometry and structure, on the frequency, on the material used and on the operation mode. Although in physics energy oscillation is often seen as a loss, when an open structure is considered, the energy leakage is used to explain the radiation toward an open region. Leaky wave antennas take advantage of this concept and are defined as waveguiding structures characterized by some mechanisms that allow to leak power along their longitudinal direction [13]. Leaky wave antennas (LWA) boast some remarkable properties like beam-scanning, high directivity, etc. and

have become particularly interesting in microwave applications thanks to their simple fabrication compared to other antennas like phased arrays.

The main difference between a leaky wave antenna and a guided wave structure is that, due to the open nature of the LWA, the attenuation constant that describes the leakage must be considered, as showed in Figure 2.1.1.

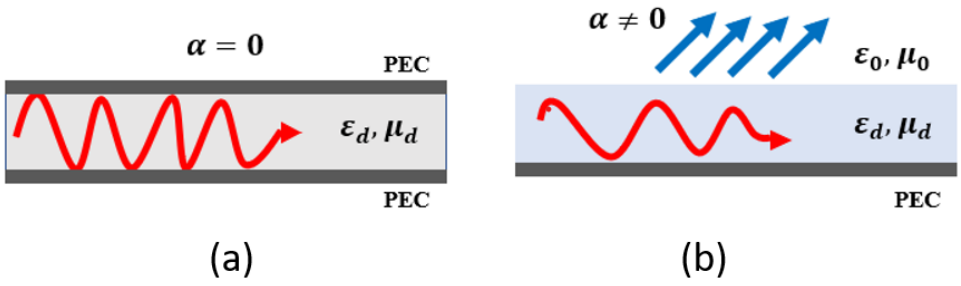

***Figure 2.1.1**: Guided wave structure (a) and leaky wave structure (b).*

Due to the leakage the propagation wavenumber has a complex nature:

$$k = \beta - j\alpha \tag{2.1}$$

where β is the phase constant and α is the leakage constant related to the amplitude attenuation. The wavenumber has this expression in the direction along which the leakage happens. A large leakage constant α implies a vast leakage that corresponds to a wide beamwidth. To have instead a long effective aperture, that corresponds to a more directive beam, a low leakage constant is needed [13]. In the case of fixed and finite aperture, the beam dimension is mostly affected by the fixed aperture, whereas the leakage constant will strongly influence the antenna radiation efficiency. The radiation efficiency is maximized with a leakage constant as high as possible, so that most of the power is leaked before the wave reaches the end of the antenna. The phase constant β changes with frequency and it's the one responsible for beam scanning. To describe the physical principle behind Leaky Waves, the earliest example of LWA is considered. As shown in Fig 2.1.2, a rectangular waveguide with a continuous slit along the length of one side is considered.

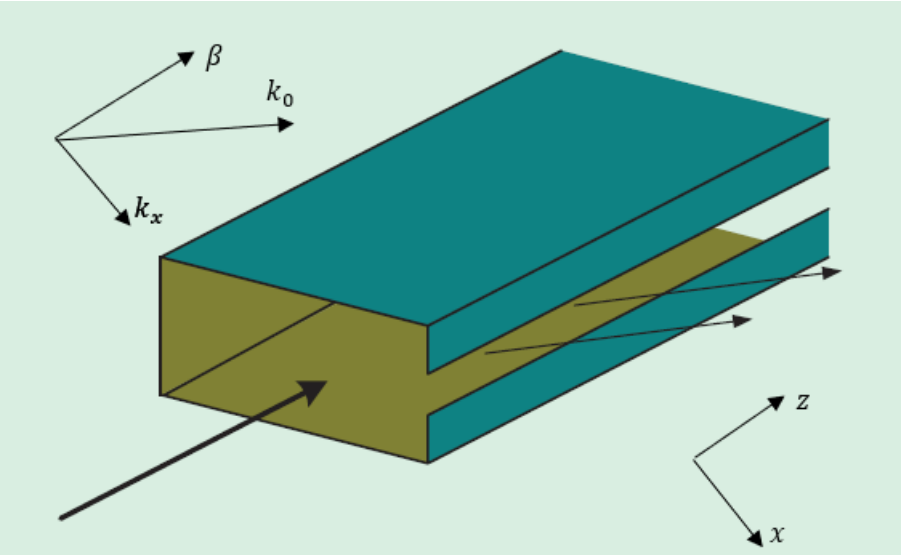

***Figure 2.1.2**: Rectangular waveguide with a cut along the length. [13],[14]*

Leaky waves find their origin in the guided waves theory, meaning that there are certain conditions for a guided wave that have to be fulfilled in order to produce a leakage. A closed non-dissipative structure supports eigenmodes with purely real, corresponding to propagating waves of constant amplitude, or purely imaginary wavenumbers, corresponding to evanescent waves. In the case of losses, the wavenumber becomes complex. Open structures, instead, support only complex eigenmodes that are originated due to radiation losses, even when the structure is non-dissipative.

The structure in Fig. 2.1.2 is a simple guided wave ($e^{-j\beta z}$) , travelling along the +z direction and described by a phase constant β [14]. The aperture on one side generates a leaky wave with wavevector k_x such that:

$$k_x^2 = k_0^2 - \beta^2, \tag{2.2}$$

meaning the k_x must be a real number in order to have a leaky wave. This results in a necessary condition to generate a leaky wave: $\beta < k_0$. As soon as a leaky wave is generated the field is subject to an attenuation as it propagates in the +z direction, so the leaky wave goes as $e^{-j\gamma z}$ with

$$\gamma = \alpha + j\beta. \tag{2.3}$$

The leaky wave in the x-direction instead will have a given α_x attenuation and it is described by the following equation:

$$k_0^2 = (\beta - j\alpha)^2 + (k_x - j\alpha_x)^2. \tag{2.4}$$

Since $\alpha > 0$ due to passivity, the equation is fulfilled only if $\alpha_x < 0$. This is the second condition that allows the generation of a leaky wave. It may appear that this result has no physical meaning since the leaky wave should raise exponentially to infinity along the transversal direction. In reality, the structure of leaky-wave antennas has finite size, so the wave grows exponentially only in a limited region close to the antenna, after which it decays. The so-called shadow boundaries set the limit of this region.

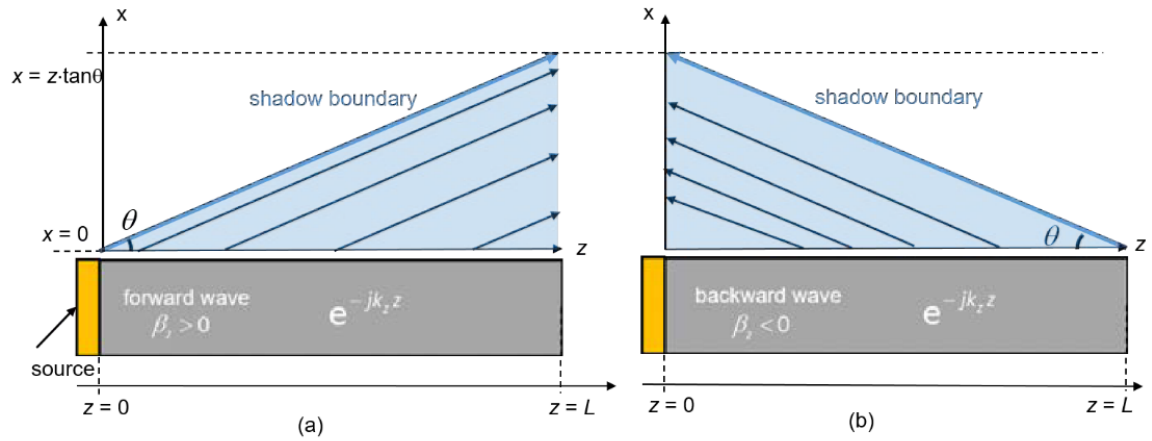

***Figure 2.1.3**: Ray-optics representation of inward (a) and backward leaky waves (b) [15].*

It's useful to introduce another concept regarding the physics of leaky waves that will be clarifying for following part. As said, the condition to have a leaky wave can be expressed as $|\beta| < k_0$. In the case of $\beta > 0$, we are in presence of forward waves, which are able to leak power in a region far from the source. If instead $\beta < 0$ we are in the case of backward waves, that own the remarkable property of being able to focus the leakage in the near field, the region closest to the antenna [15], as Figure 2.1.3.

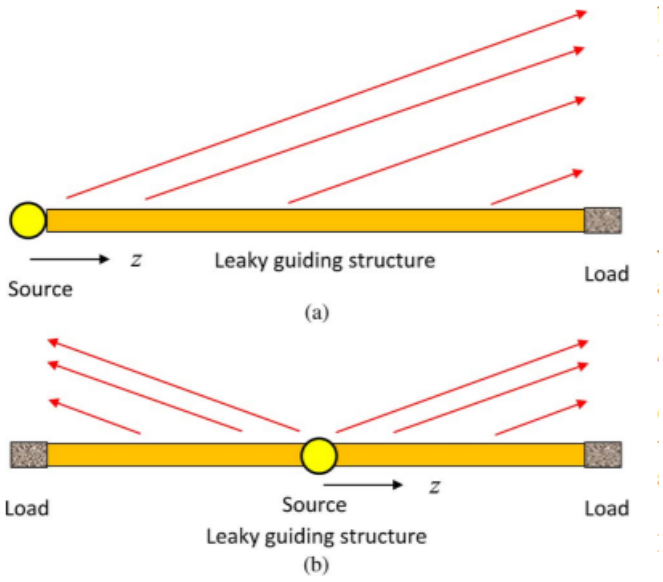

***Figure 2.1.4**: Unidirectional (a) and bidirectional (b) mode of operation of a LWA [16].*

A first classification of Leaky-Wave Antennas can be based on the position of the source [16]:

- *Unidirectional Leaky Wave Antennas* have a source at one end of the guiding structure and radiate (through energy leakage) waves only in one direction at which end partially open is usually present , as shown in Figure 2.1.4 (a).
- *Bidirectional Leaky Wave Antennas* have a source in the middle of the guiding structure. This way, the radiation happens in two different directions. The matched load is located at both side of the guiding structure, as shown in Figure 2.1.4 (b).

Then, based on the geometry of the structure, LWA can be classified in *uniform* and *periodic*:

- *Uniform leaky-wave antennas* are uniform along the length of the guiding structure [13]. An example of uniform 1D-LWA is the rectangular waveguide in Fig.2.1.2. Usually, in closed waveguides, a fast wave ($\beta < k_0$) travels, disturbed by some cuts along the structure that allows the generation of the

leaky wave. In case of open structures only slow waves travels in the structure ($\beta > k_0$) and to reach a leaky wave some asymmetry or geometrical modification must be introduced. [14]

- *Periodic Leaky Wave Antennas* shows a periodicity in the structure. Differently from uniform antennas, the dominant mode in the structure is a slow wave, therefore it is not able to radiate. What allows the leakage of energy is a periodical modulation of the guided-wave structure. An example of periodic LWA is reported in Figure 2.1.5, a rectangular dielectric waveguide on which the periodicity is given by a printed or placed metal strips array.

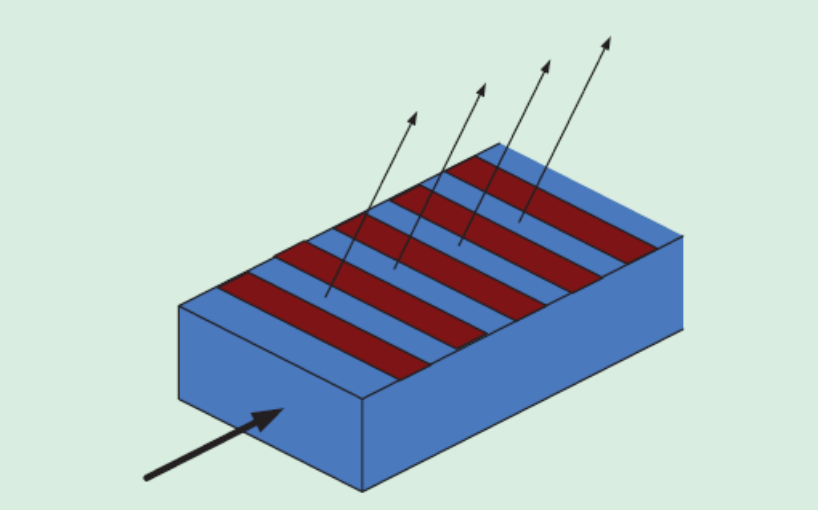

***Figure 2.1.5**: Rectangular guided dielectric slab with a periodic array of metal strips [14].*

When the periodicity of the array strips is added it produces an infinite number of space harmonics, that are related to each other by the Floquet's theorem [14]:

$$\beta_n d = \beta_0 d + 2n\pi, \tag{2.4}$$

where β_n is the characteristic phase constant of each harmonic and d is the length of the period, while β_0 is the phase constant of the fundamental space harmonic. Usually in periodic LWA a single beam is generated, and the

relevant design becomes the one of the first space harmonic ($n = -1$). The phase constant of this harmonic is [14]:

$$\beta_{-1} = \beta_0 - \frac{2\pi}{d}, \tag{2.5}$$

and in order to have a fast wave in the first space harmonic the condition $\beta_{-1} < k_0$ must be respected.

Our attention will be devoted to periodical LWA, since the developed Bessel Beam Launcher relies on this category of antennas. In particular, we consider 2D-LWA that are also known as Fabry-Perot Cavity (FPC) Leaky-Wave Antennas and will allow the generation of the desired Bessel Beam function. A leaky radial waveguide allows a strict connection between leaky waves and non-diffractive waves, since the solutions that satisfy the wave equation of these waveguide will contain functions useful for the generation of non-diffractive beams.

Bessel Beams are a non-diffractive solutions of the scalar wave equation. The generic wave equation in a homogeneous medium with a cylindrical reference system (ρ, ϕ, z) is [17]:

$$\left(\frac{\partial^2}{\partial\rho^2} + \frac{1}{\rho}\frac{\partial}{\partial\rho} + \frac{1}{\rho^2}\frac{\partial^2}{\partial\phi^2} + \frac{\partial^2}{\partial z^2} - \frac{1}{c^2}\frac{\partial}{\partial t^2}\right)\psi(\rho, \phi, \mathrm{z}, \mathrm{t}) = 0 \tag{2.6}$$

With c the speed of light in the vacuum and $\psi(\rho, \phi, \mathrm{z}, \mathrm{t})$ the scalar function that can be replaced by a field or a vector potential component.

Bessel Beams are axially symmetric solutions with $\frac{\partial}{\partial\phi} = 0$, so independent from ϕ variable:

$$\left(\frac{\partial^2}{\partial\rho^2} + \frac{1}{\rho}\frac{\partial}{\partial\rho} + \frac{\partial^2}{\partial z^2} - \frac{1}{c^2}\frac{\partial}{\partial t^2}\right)\psi(\rho, \mathrm{z}, \mathrm{t}) = 0. \tag{2.7}$$

The solution that allows to have Bessel Beam generation is of the form:

$$\psi(\rho, \mathrm{z}, \mathrm{t}) = J_0(k_\rho \rho) e^{-jk_z z} e^{j\omega_0 t}, \tag{2.8}$$

with J_0 the zeroth-order Bessel function and k_ρ, k_z the wavenumbers.

They support modes with normal electric field (TM) or normal magnetic field (TE) behaving as a zeroth-order Bessel function. In their ideal form, Bessel Beams are constituted by a conical superposition of plane waves.

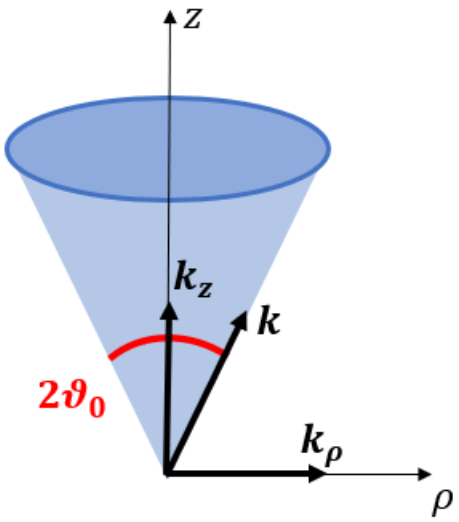

***Figure 2.1.6**: Wavevectors lying on the surface of a cone.*

Wavevectors are of the form $k = k_\rho \hat{\rho} + k_z \hat{z}$ (2.9), with (ρ, z) coordinates of a cylindrical reference system. They lie on the surface of a cone with a given axicon angle ϑ_0 such that $0 \leq \vartheta_0 \leq \frac{\pi}{2}$, as showed in Fig. 2.1.6. It follows that wavenumbers are linked by the following relations [15]:

$$k_0^2 = k_\rho^2 + k_z^2 , \tag{2.10}$$

$$k_\rho = k_0 \sin(\vartheta_0) = \frac{\omega_0}{c} \sin(\vartheta_0) , \tag{2.11}$$

$$k_z = k_0 \cos(\vartheta_0) = \frac{\omega_0}{c} \cos(\vartheta_0) . \tag{2.12}$$

As anticipated, ideal Bessel Beams carry an infinite amount of energy, and the propagation distance does not affect the transverse intensity distribution:

$$\psi(\rho, \mathrm{z} \geq 0, \mathrm{t}) = \psi(\rho, \mathrm{z} = 0, \mathrm{t}). \tag{2.13}$$

Indeed, ideal Bessel Beams are not physically implementable, instead, what can be actually obtained are truncated Bessel Beams with a limited non-diffractive range defined as [15]:

$$z_{ndr} = \rho_{ap} \cot(\vartheta_0) = \rho_{ap} \frac{k_z}{k_\rho} . \tag{2.14}$$

The nondiffractive range z_{ndr} is directly proportional to ρ_{ap} radius of the aperture through which the beam is generated. At the expence of a larger antenna the diffraction-free zone can be extended for longer distances. The nondiffractive range, defined in this way, represents the maximum distance at which the Bessel Beam maintains its non-diffractive behaviour. Beyond the nondiffractive range, the beam is no longer described by a zeroth-order Bessel function and its intensity rapidly decreases.

Another important quantity used to describe Bessel Beams properties is the null-to-null beamwidth, defined as [15]:

$$NNBW = 2\rho_{NN} = \frac{2j_{0,1}}{k_\rho} \cong \frac{4.81}{k_\rho}, \tag{2.15}$$

with $k_\rho \rho_{NN} = j_{0,1}$ and $j_{0,1} = 2.4048$ the first null of the zeroth-order Bessel function. This means that, for fixed k_ρ and ϑ_0 axicon angle, there is a trade-off between the achievable nondiffractive range and the directivity of the beam described by the NNBW. A narrower NNBW can be achieved at the expense of a lower non-diffractive range.

This parameter is of fundamental importance in near field focusing. In some works, the analysis is conducted following the scalar-wave theory and applying the paraxial approximation. This kind of analysis is reliable only when the size of the aperture

generating the beam is much larger than the wavelength at which it operates. As a result, scalar wave approximation focuses only on Bessel Beams with beamwidth (NNBW) much larger than the operating wavelength. For our purposes, this approximation cannot be applied since the NNBW will have dimensions comparable to the operating wavelength. A full-wave simulation is needed to properly take into account the vectorial nature of the beam.

The proposed Bessel Beam Launcher is based on Leaky Radial Waveguide that is a parallel plate waveguide, that may be air-filled or containing dielectric. Over the grounded dielectric slab there is a partially reflective sheet (PRS) to improve directivity. What differentiates this structure from a classical 2D leaky-wave antenna is the presence of a metallic rim around the resonant cavity, whose dimension will be of fundamental importance. Since the objective is to create a resonant structure, the presence of the metallic rim allows to have the propagation inward and backward leaky waves that combined form a resonant mode.

As anticipated, the scalar approximation cannot be applied in the analysis of Bessel Beam launchers. One way to proceed is to resort to Maxwell's equations, obtaining the solutions for electric (*E*) and magnetic (*H*) fields by means of magnetic (*A*) and electric (*F*) vector potentials. These are functions defined in order to simplify the computation of the solution.

The project carried out within this thesis activity is focused on the excitation of a transverse-electric (TE) mode that shows the zeroth-order Bessel function in the longitudinal component of the magnetic field, such that:

$$H_z = J_0\left(k_\rho \rho\right) e^{-jk_z z}. \tag{2.16}$$

The TE mode is fully described by the z-component of the electric vector potential *F*, that satisfies the Helmholtz equation in a homogeneous medium in cylindrical coordinates [17]:

$$\frac{\partial^2 F_z}{\partial \rho^2} + \frac{1}{\rho}\frac{\partial F_z}{\partial \rho} + \frac{1}{\rho^2}\frac{\partial^2 F_z}{\partial \phi^2} + \frac{\partial^2 F_z}{\partial z^2} + k^2 F_z = 0. \tag{2.17}$$

The vector potential that solves this expression will be expressed in cylindrical coordinates with azimuthal, radial, and longitudinal dependences. The solution may take various forms and it is different depending on the region that is considered.
Inside the circular waveguide the electric vector potential that satisfies the Helmholtz equation has the following form [17]:

$$F_z = \cos(k_z z)\, e^{jn\phi} \left[C_1 H_0^{(1)}(k_\rho \rho) + C_2 H_0^{(2)}(k_\rho \rho) \right], \tag{2.18}$$

where $H_0^{(1)}(k_\rho \rho)$ and $H_0^{(2)}(k_\rho \rho)$ represent the Hankel functions of first and second kind, respectively, whereas C_1, C_2 are the coefficients to be determined depending on the boundary conditions. The radial wavenumber is $k_\rho = \beta_\rho - j\alpha_\rho$ with $\beta_\rho, \alpha_\rho > 0$ whereas the normal wavenumber is $k_z = \beta_z + j\alpha_z$ with $\beta_z, \alpha_z > 0$ since the structure supports leaky wave modes. The dependency along the *z*-direction is expressed through a cosine or sine function because this is the region inside the circular waveguide where fields are confided. It will be a different kind of function for the region outside the waveguide. The Hankel functions are defined as:

$$H_a^{(1)}(x) = J_a(x) + \mathrm{j}\, Y_a(x), \tag{2.19}$$

$$H_a^{2}(x) = J_a(x) - \mathrm{j}\, Y_a(x), \tag{2.20}$$

where $J_a(x)$ is the Bessel function of first kind and $Y_a(x)$ is the Bessel function of the second kind. Hankel functions of first and second kind are two linearly independent solution of Bessel's differential equation. From the expression of the electric vector potential component F_z (2.18) it is possible to find the electric and magnetic fields components for a TE mode by substituting [17]:

$$E_\rho = -\frac{1}{\varepsilon\rho}\frac{\partial F_z}{\partial \Phi} \quad (2.21) \qquad H_\rho = -j\frac{\eta}{k}\frac{\partial^2 F_z}{\partial\rho\,\partial z} \quad (2.22)$$

$$E_\Phi = \frac{1}{\varepsilon}\frac{\partial F_z}{\partial\rho} \quad (2.23) \qquad H_\Phi = -j\frac{\eta}{k\rho}\frac{\partial^2 F_z}{\partial\Phi\,\partial z} \quad (2.24)$$

$$E_z = 0 \quad (2.25) \qquad H_z = -j\frac{\eta}{k}\left(\frac{\partial^2}{\partial z^2} + k^2\right)F_z \quad (2.26)$$

With η the characteristic impedance inside the circular waveguide. In the case of axially symmetric field $\frac{\partial}{\partial\phi} = 0$ and n=0, so the expression of the vector potential becomes:

$$F_z = \cos(k_z z)\left[C_1 H_0^{(1)}(k_\rho\rho) + C_2 H_0^{(2)}(k_\rho\rho)\right]. \quad (2.27)$$

Such that some components of the field will be null: $E_z = H_\Phi = E_\rho = 0$.
The other components are:

$$E_\Phi = k_\rho \cos(k_z z)\left[C_1 H_1^{(1)}(k_\rho\rho) + C_2 H_1^{(2)}(k_\rho\rho)\right], \quad (2.28)$$

$$H_\rho = -j\frac{\eta k_z k_\rho}{k}\sin(k_z z)\left[C_1 H_1^{(1)}(k_\rho\rho) + C_2 H_1^{(2)}(k_\rho\rho)\right], \quad (2.29)$$

$$H_z = -j\frac{\eta k_\rho^2}{k}\cos(k_z z)\left[C_1 H_0^{(1)}(k_\rho\rho) + C_2 H_0^{(2)}(k_\rho\rho)\right]. \quad (2.30)$$

The H_z component (2.30) will be a combination of Hankel functions that represent the outward $H_0^{(2)}(k_\rho\rho)$ and inward $H_0^{(1)}(k_\rho\rho)$ cylindrical waves inside the waveguide. The operating principle to generate Bessel Beams is based on the fact that the source generates at the centre of the antenna outward travelling Hankel waves (incident waves). These are then reflected back by the circular metallic rim, becoming Hankel inward travelling waves. The constructive interference of these two kinds of waves give rise to a structure that is resonant in the radial direction, as showed in Fig.2.1.7.

The presence of a metallic rim that enforces the resonance is the main difference between a classical 2D LWA and a Bessel Beam Launcher.

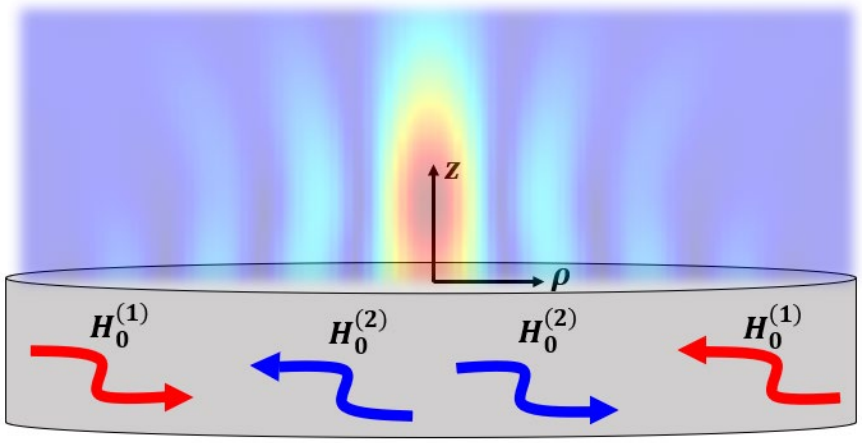

***Figure 2.1.7**: Grounded dielectric slab covered with PRS. Hankel inward waves are generated and reflected back from the metallic rim in form of backward Hankel waves, generating a resonant Bessel Beam Launcher.*

Indeed, this mechanism generates the wanted Bessel Beam if some conditions are fulfilled. The H_z field assumes the zeroth-order Bessel function distribution if $C_1 = C_2$, that practically correspond to the placement of the metallic rim in a specific position. The metallic rim must have radius $\rho = \rho_{ap}$ and it must be placed in one of the zeros of the Bessel function $J_0(k_\rho \rho_{ap})$. This is necessary to have the incident wave reflected back with almost the same coefficient. In order to satisfy $C_1 = C_2$ [15]:

$$\beta_\rho \rho_{ap} = j_{0,n} \quad , \quad n \in \mathbb{N} \tag{2.31}$$

$$\alpha_\rho \rho_{ap} \ll 1. \tag{2.32}$$

The first condition (2.31) set the correct position of the metallic rim in the n – th zero of the zeroth- order Bessel function. The position of the rim is changed depending on the wanted number of zeros in the Bessel Beam generated outside the circular

waveguide. The second condition (2.32) corresponds to a limit in the attenuation of the incident wave: if the incident wave is too much attenuated as it goes from the source at the centre of the antenna to the metallic wall of the rim then the reflected wave won't present the same coefficient. If the condition $C_1 = C_2$ is satisfied, then the expressions of the fields become the following:

$$E_{\Phi} = k_{\rho} \cos(k_z z) J_1(k_{\rho}\rho), \tag{2.33}$$

$$H_{\rho} = -j \frac{\eta k_z k_{\rho}}{k} \sin(k_z z) J_1(k_{\rho}\rho), \tag{2.34}$$

$$H_z = -j \frac{\eta k_{\rho}^2}{k} \cos(k_z z) J_0(k_{\rho}\rho). \tag{2.35}$$

The transversal fields (2.33, 2.34) will behave as a first-order Bessel function, whereas the longitudinal component H_z (2.35) behaves as a zeroth-order Bessel function.

These fields are referred to the region inside the circular waveguide, whereas in the region outside, to reach the desired exponential dependence, the electric vector potential assumes a different form [6]:

$$F_z = e^{-jk_z z} e^{jn\phi} \left[C_1 H_0^{(1)}(k_{\rho}\rho) + C_2 H_0^{(2)}(k_{\rho}\rho) \right]. \tag{2.36}$$

By repeating the same procedure, the electromagnetic fields of the propagating TE-polarized Bessel Beams outside the structure are obtained with $E_z = H_{\Phi} = E_{\rho} = 0$:

$$E_{\Phi} = J_1(k_{\rho}\rho) e^{-jk_z z}, \tag{2.37}$$

$$H_{\rho} = -\frac{k_z}{k\eta} J_1(k_{\rho}\rho) e^{-jk_z z}, \tag{2.38}$$

$$H_z = j \frac{\eta k_{\rho}}{k} J_0(k_{\rho}\rho) e^{-jk_z z}. \tag{2.39}$$

Both the fields inside the radial waveguide and the fields outside of it will differ for a multiplicative constant that mainly depends on the excitation. It will be verified that the fields found with our developed structure are in agreement with the above-discussed distributions.

2.2 Bull-Eye LWA Bessel Beam Launcher

Wireless Power Transfer applications at millimetre waves, that lie in the frequency range of 30-300 GHz, is a matter of paramount interest for nowadays' research activities, both in the far-field and in in reactive (non-radiative) near-field. However, mm-waves applications operating in the radiative near-field still need to be thoroughly investigated, and in particular, most of them make use of focused diffractive beams. For this reason, the purpose of this thesis work is to investigate the possibility of exploiting the nondiffractive properties of Bessel Beal launchers in the radiative near-field (Fresnel region) for wireless power transfer applications
The proposed antenna belongs to the class of resonant Fabry-Perot cavities (FPC), whose physical principles have been explained in the previous chapter. A remarkable property of Fabry-Perot cavities is that they have a small thickness, in this case a $\lambda/2$- thick profile. Our interest is devoted to the excitation of a TE field that shows a z-component of the magnetic field with the typical zeroth-order Bessel function profile. Indeed, this type of excitation has not been fully investigated in literature, in fact most of the research activities are mainly focused on design TM-polarized Bessel Beam launcher, for which the excitation is provided through a coaxial cable. Furthermore, having a TE-polarized Bessel Beam implies the use of a planar loop as excitation source, which would allow a miniaturization of the overall rectification circuitry through planar technology, creating a more compact structure of the overall antenna. The project described in this thesis has the main goal to be applied in the context of wireless power transfer for wearable applications, thus the design should

be carried out in such a way that the decoupling with the human body is guaranteed. Furthermore, miniaturization is also a fundamental characteristic that need to be accounted for, though working at millimetre waves establish a trade-off between miniaturization and energy transfer efficiency [19]. The frequency of application of our Bessel Beam Launcher is approximately 30 GHz. Regardless the polarization of the field that we want to radiate, the structure of the FPC BB Launcher is made of a grounded dielectric slab, a metallic rim enforcing the resonance, and a partially reflecting sheet (PRS) placed on top. The principles behind the development, as well as the numerical results obtained for this particular Bessel Beam Launcher, are explained in [18] and reported in the following.

To select the polarization of the excited mode what changes is the source placed in the middle of the dielectric slab: theoretically a vertical electric dipole (VED) excites a TM leaky mode with an electric field component E_z going as a zeroth order Bessel function, while a vertical magnetic dipole (VMD) excites a TE leaky mode with the wanted Bessel profile over H_z. In reality, while a coaxial cable excites a pure TM mode, it's not easy to find a source able to excite a pure TE mode. The operative steps to achieve a correct design can be summarize as follows:

- Identify some constraint on both the nondiffractive range z_{ndr} and the antenna aperture radius ρ_{ap}, which are related to the axicon angle ϑ_0 through the formula:

$$z_{ndr} = \rho_{ap}\, cot\, \vartheta_0. \tag{2.40}$$

- Select the number of zeros that will figure in the distribution of the radiated Bessel Beam profile j_{0n} ($n \in \mathbb{N}$). As previously discussed, the circular metallic rim must be placed in one of the zeros of the Bessel function, leading to the relation:

$$\beta \rho_{ap} = j_{0n}. \tag{2.41}$$

- From the aforementioned equation (2.41), and by knowing that the radial wavenumber is equal to $k_\rho = \beta - j\alpha$ (2.42) ,with β the phase constant and α the attenuation (leakage) constant, β and α can be determined in order to generate a beam that fulfils the requirements over the nondiffractive range and the dimension of the antenna.

- Determine the cavity thickness h and the PRS reactance X_S necessary to have the proper phase and attenuation constant at the given frequency of operation. This is done through the equivalent loss tangent model for the cavity, deeply explained in [20].

Another relation that links phase constant to the axicon angle is $\beta = k_0 sin\vartheta_0$ (2.43) with k_0 the free space wavenumber. It follows that the radius, the nondiffractive range, and the order of radial resonance of the structure can be related through:

$$\bar{z}_{ndr} = \bar{\rho}_{ap} \sqrt{\left(\frac{\bar{\rho}_{ap}}{\bar{\rho}_n}\right)^2 - 1}\,, \tag{2.44}$$

with all the quantities normalized with respect to wavelength λ_0 and $\bar{\rho}_n = j_{0n}/2\pi$. The phase and attenuation constants are normalized as $\hat{\beta} = \beta/k_0$ and $\hat{\alpha} = \alpha/k_0$. After the computation of the phase constant, the amplitude constant can be found by assuming a plane-wave approximation inside the cavity, such that the constraint to fulfil is $\hat{\alpha} < -\ln a_r/(4\pi\,\bar{\rho}_{ap})$ with $0 < a_r < 1$. The constant a_r represents the ratio of the inward and outward waves power amplitude. Since the resonance inside the cavity is maximized if the reflected wave returns with almost the same amplitude of the incident one, the value of a_r should be as close as possible to 1. This comes at the expense of a trade-off between the quality factor of the cavity Q and the accuracy of the beam profile, so a reasonable value is $a_r = 0.95$ to avoid the implementation of a

cavity with too high Q. The initial constraint set for the radius and the nondiffractive range considers the possible application of the launcher for near-field and wearable devices: the distance covered must be at least 2 cm and the radius of the antenna 1.5 cm. The number of zeros in the distribution of Bessel function (radial resonance of the structure) is set to $n = 2$, since exploiting an $n = 1$ would generate a excessively truncated beam.

With all these requirements and supposing 30 GHz as frequency of operations, $\hat{\beta} \simeq 0.5857$ (2.41) with an axicon angle of $\vartheta_0 \simeq 36°$(2.43), and $\hat{\alpha} \simeq 0.0027$ (2.42). Then, assuming an air-filled cavity, $X_S = 26.7\Omega$ and $h = 6.04mm$. These are the preliminary numerical computations necessary to define all the parameters needed to build the FPC-like Bessel Beam Launcher.

The realized antenna is simulated by means full wave EM analysis, using CST Microwave Studio, and a schematic representation is reported in Fig. 2.2.1.

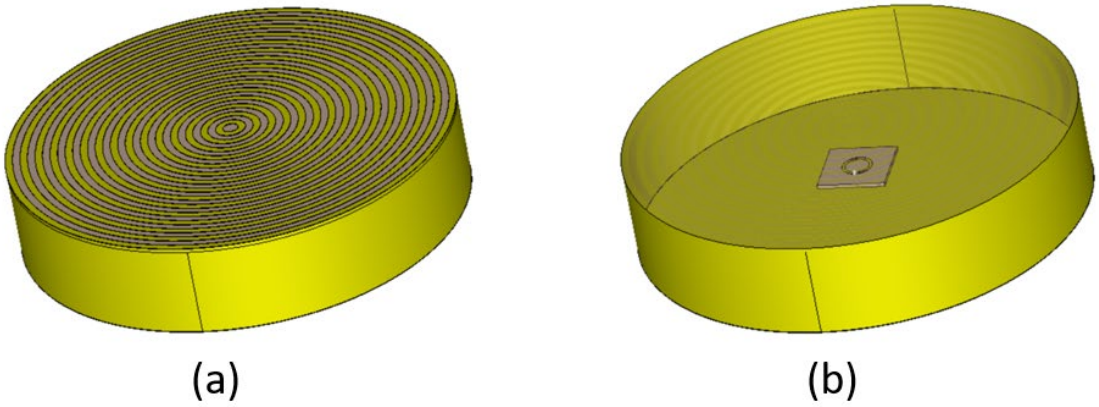

Figure 2.2.1*: Bessel Beam Launcher of radius 1.5cm realized in CST Microwave Studio. External view (a) and internal view (b).*

The surface printed on top of the grounded dielectric slab is made of concentric microstrip rings that are driven by a source placed at the centre of the antenna.

This kind of antenna belongs to the so-called 'bull-eye' antennas, a class of annular structures , showed in Figure 2.2.2. The annular strip gratings surface shows satisfactory results in the case of a TE polarization.

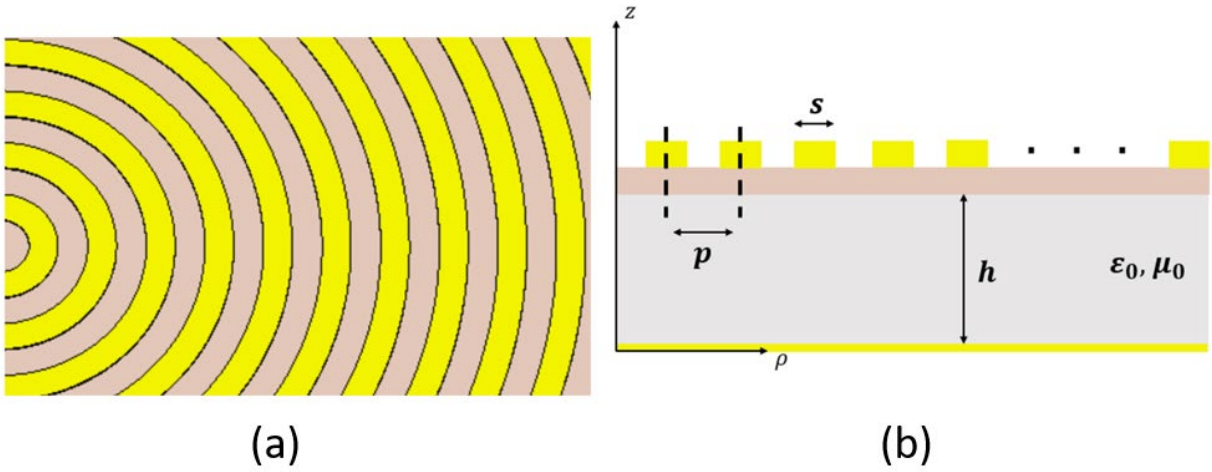

***Figure 2.2.2**: Details of the Bull-Eye surface with annular metallic rings (a) and representation along the radial direction (b).*

The annular strip gratings are realized in copper and placed over a dielectric substrate Rogers RO3003 with relative permittivity $\varepsilon_r = 3$ and $\tan\delta = 0.001$. In this structure with $\rho_{ap} = 1.5\ cm$ there is a total number of 15 annular strip gratings, each large $s = 0.5\ mm$, with distance among their centres $p = 1\ mm$ and having a thickness of $0.254\ mm$. It is worth noticing that since the relation $s \ll p$ is not valid in fact $\frac{s}{p} = \frac{1}{2}$, the theory of annular strip gratings is not reliable. Regarding the feeding, to excite a TE mode a full wave planar loop antenna is used. Its radius is 1 mm such that $2\pi R \simeq \lambda$, the microstrip width is 0.2 mm, realized on a 0.254mm-thick substrate, the Rogers 3003. The antenna is excited by a 50 Ω- discrete port and placed halfway through the air-filled resonant cavity height, to enforce the resonance coming from incident and reflected waves.

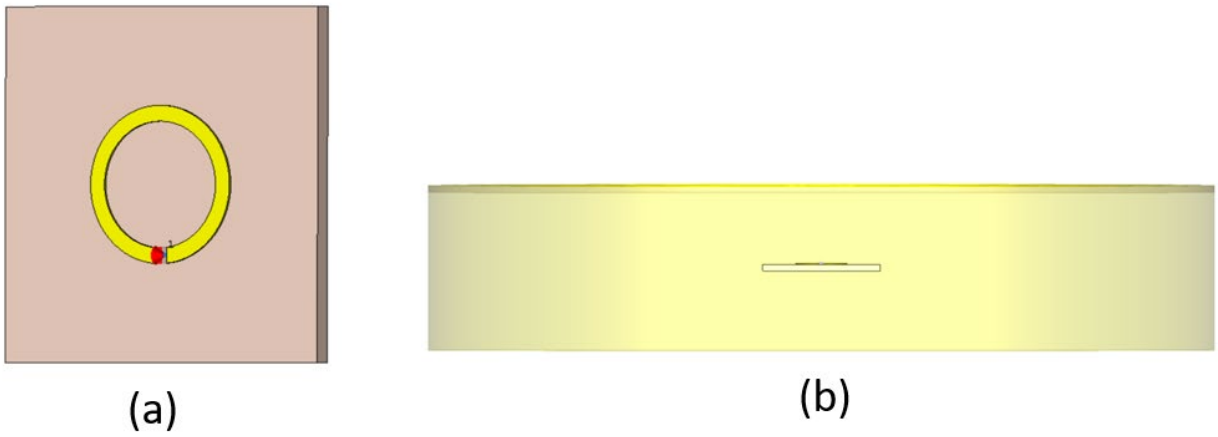

***Figure 2.2.3**: Loop antenna exciting the structure (a) and its position at the centre of the FPC (b).*

Unfortunately, the loop antenna, as a matter of fact, does not represent a perfect vertical magnetic dipole (VMD). For this reason, the excited mode is not a pure TE but an hybrid-TE, showing a z-component of the electric field not exactly equal to zero. In any case the amplitude of E_z is small enough to have the generated mode falling in the category of hybrid -TE. The fields generated by this Bull-Eye LWA will be further presented and discussed in the next chapter. From the results of the full-wave analysis, it is observed that the antenna resonates at 32.42 GHz , as reported in Figure 2.2.4, with an inductive input impedance of $Z_A = 24.8 + j5.3\Omega$, as reported in Figure 2.2.5.

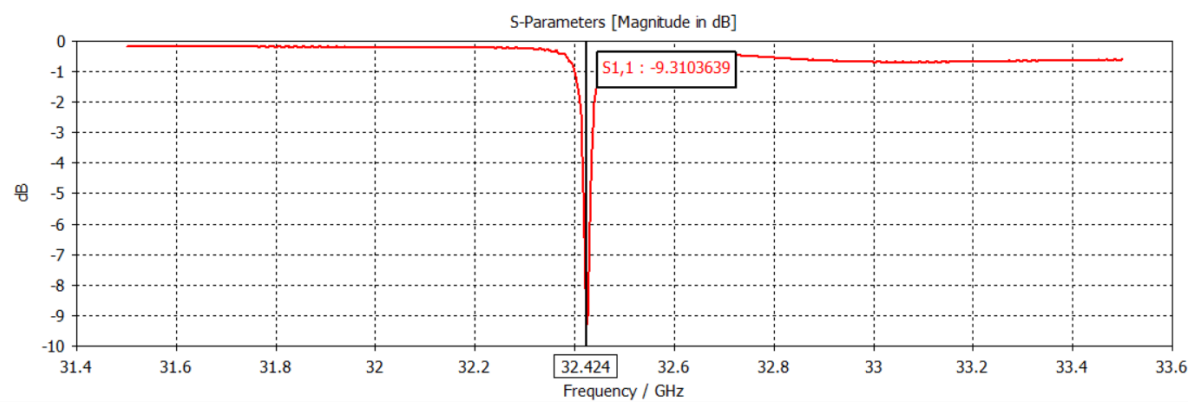

***Figure 2.2.4**: Frequency of resonation of the BB Launcher of radius 1.5cm (from CST Microwave Studio).*

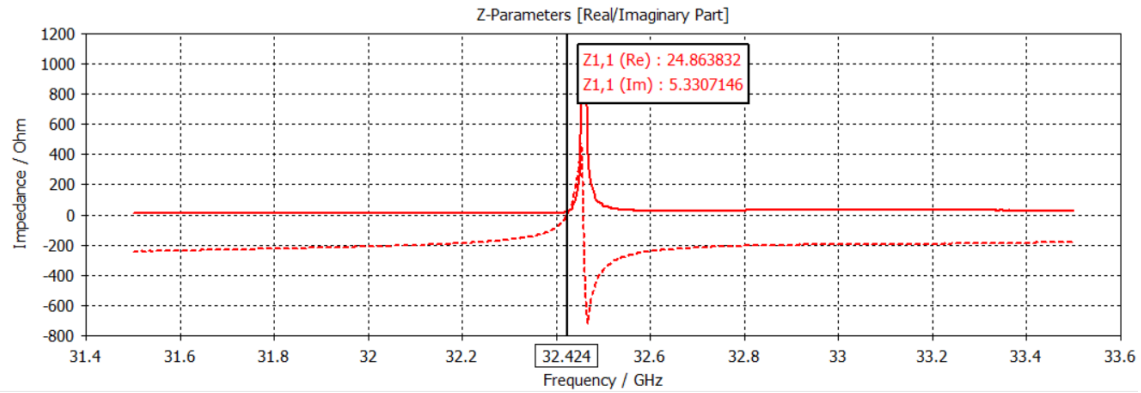

***Figure 2.2.5**: Impedance of the BB Launcher of radius 1.5cm (from CST Microwave Studio).*

After the realization of this launcher, the ρ_{ap} of the antenna is roughly doubled, to observe the improvement in the radiation characteristics, such as the non-diffraction range. All the other parameters are left unchanged both for the loop antenna and for the FPC-like structure. The structure is showed in Figure 2.2.6.

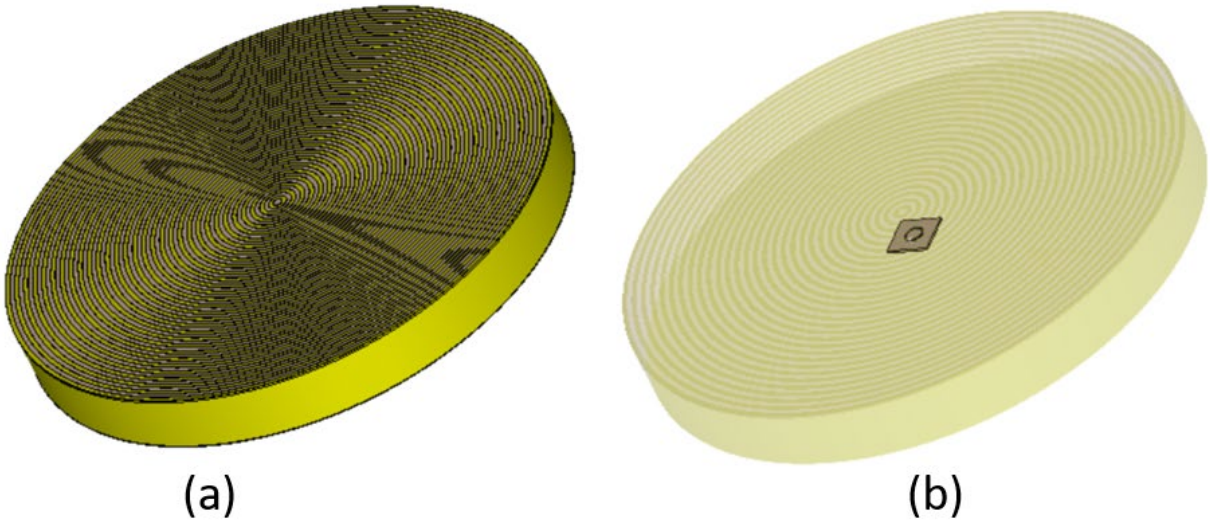

***Figure 2.2.6**: Bessel Beam Launcher with a radius of 3 cm realized in CST Microwave Studio. External view (a) and internal view (b).*

The radius of the aperture becomes $\rho_{ap} = 3\ cm$ with a total number of annular strip gratings of 30. The resonant frequency is slightly changed to 31.67 GHz, as showed in Figure 2.2.7, since the radius is roughly doubled without following again the

design procedure. The impedance becomes $Z_A = 67.9 + j1.9\Omega$, reported in Figure 2.2.8.

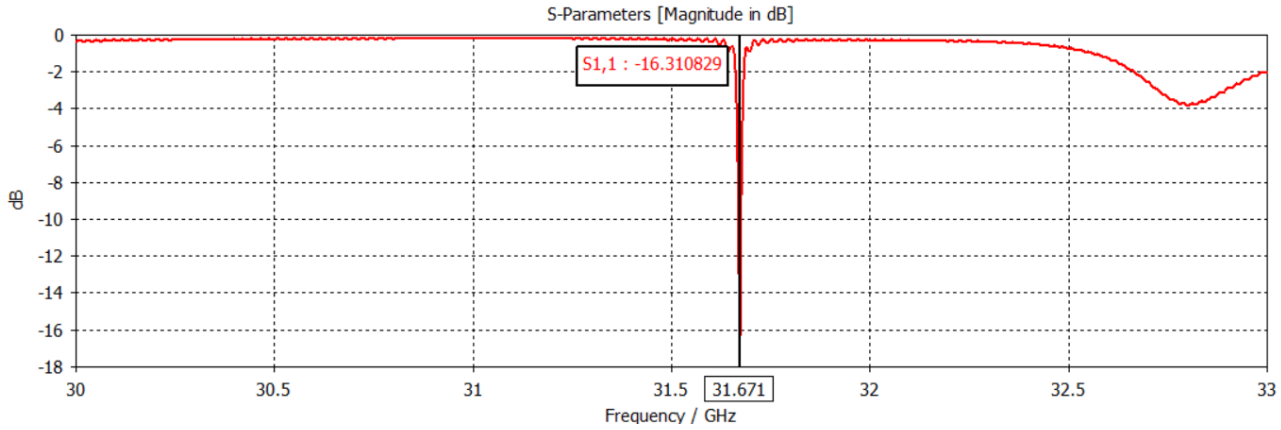

***Figure 2.2.7**: Frequency of resonation of the BB Launcher of radius 3cm (from CST Microwave Studio).*

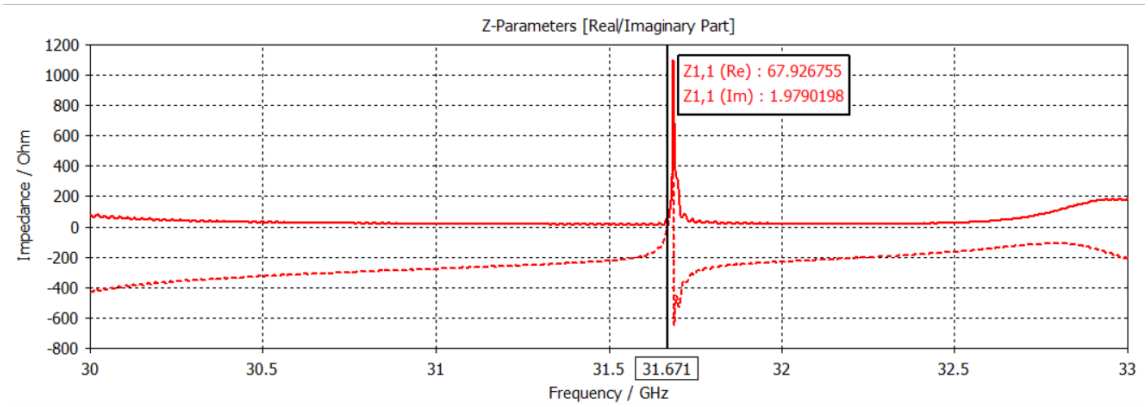

***Figure 2.2.8**: Impedance of the BB Launcher of radius 3cm (from CST Microwave Studio).*

For the sake of comparison, the numerical properties of the two Bull-Eye LWA Bessel Beam Launchers are reported:

- Bull-Eye LWA BB Launcher of smaller radius:

$$f = 32.424GHz$$

$$\lambda = 0.93\ cm$$

$$\rho_{ap} = 1.5\ cm$$

$$J_{02} = 5.5201$$

$$\beta = J_{02}/\rho_{ap}$$

$$\theta_0 = 32°$$

$$z_{ndr} = 2.5cm$$

$$NNBW = \frac{2x_{01}}{\beta} = 1.31cm$$

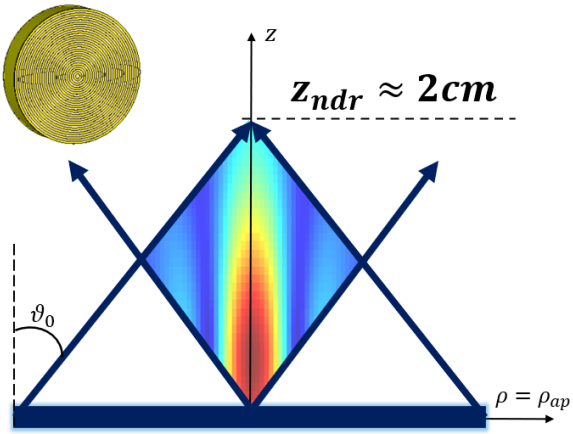

***Figure 2.2.9**: Visual representation of Bessel Beam Launcher of radius 1.5cm and its non-diffractive range.*

- Bull-Eye LWA BB Launcher of larger radius:

$$f = 31.67GHz$$

$$\lambda = 0.95\ cm$$

$$\rho_{ap} = 3\ cm$$

$$J_{04} = 11.7915$$

$$\beta = j_{04}/\rho_{ap}$$

$$\theta_0 = 36°$$

$$z_{ndr} = 4.3cm$$

$$NNBW = \frac{2x_{01}}{\beta} = 1.22cm$$

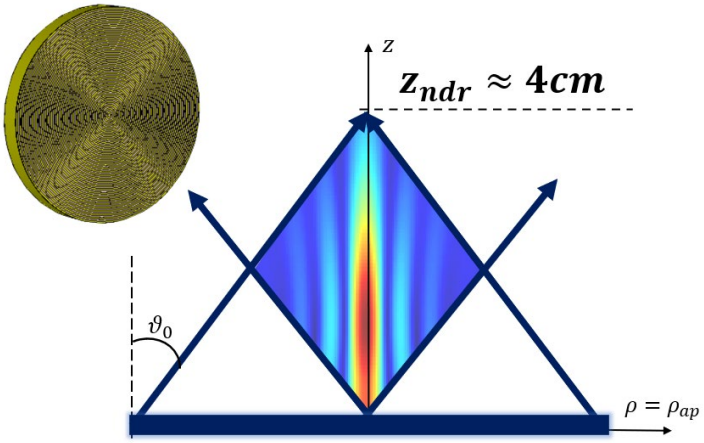

***Figure 2.2.10**: Visual representation of Bessel Beam Launcher of radius 3 cm and its non-diffractive range.*

As can be inferred by the comparison of the two antennas, when the radius is roughly doubled while the other parameters are left unchanged, the nondiffractive range, that is directly proportional to the radius of the antenna, increases, and in particular, when ρ_{ap} is doubled also the z_{ndr} becomes 4 cm. The axicon angle remains almost

unchanged, as well as the phase constant that experiences almost no drastic variations, due to the fact that, except for the radius, the other structural properties of the launcher have not been modified. The launcher with a radius of 3 cm supports a zeroth-order Bessel profile with n=4 radial resonance, showing four zeros in the radial direction. The null-to-null beamwidth is similar for the two launchers: the larger antennas is slightly more directive with a narrower beam, at the expense of more secondary rings. This preliminary analysis and comparison of the two antennas set the bases for the following chapter, in which the power budget of the wireless link, made by the Bull-Eye LWA launchers, will be investigated and rigorously evaluated.

Chapter 3: Power Transfer Properties

In the previous chapter, a detailed description of the structural properties of Bessel Beam Launchers based on Fabry-Perot cavities has been reported, together with the numerical procedure to determine the fundamental parameters of this kind of antenna, as well as the design rules that must be fulfilled. In order for these antennas to be useful in Wireless Power Transfer applications, their power transport properties must be analysed. This chapter is organized as follows: first, the procedure exploited to compute the received power is explained. Subsequently, an investigation of how the power is distributed among the different rings of a Bessel Function is conducted, by taking into account the two Bull-Eye LWA Resonators of different radius exciting an Hybrid -TE mode.

3.1 Procedure to evaluate Received Power

In a generic Wireless Power Transfer System, the RF power is received by a harvesting antenna and rectified to DC. The received RF power must be appropriately estimated with respect to the position and the orientation of the antennas involved in the link. Moreover, when the applications of interest regard wearable or implantable devices, the source is usually in the near-field of the harvesting antenna; for this reason, the far-field approximation cannot be applied. The basic circuit of a rectenna is composed of a harvesting receiving antenna followed by a rectifying circuit. Figure 3.1.1 schematically represents the Norton equivalent circuit of a rectenna, that is, as the name suggests, an antenna equipped with a rectification circuit [21].

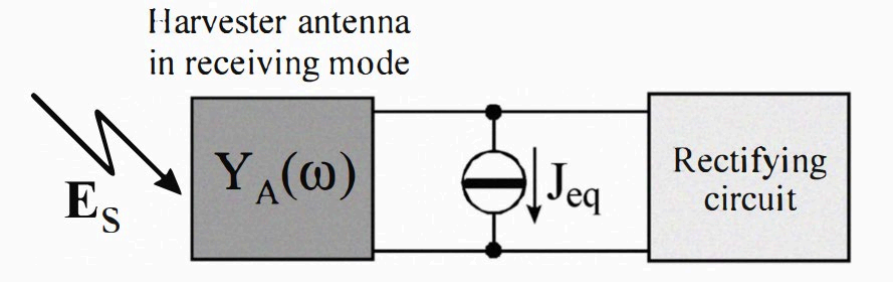

***Figure 3.1.1**: Rectenna equivalent circuit [21].*

In the presence of an incident electromagnetic field, the receiving antenna can be described by its Norton equivalent circuit, since it behaves as a linear active system, and it is analyzed exploiting EM theory principles and full-wave analysis performed in our case with CST Microwave Studio. The harvesting antenna is represented through its admittance at the operating frequency $Y_A(\omega)$, obtained with the mentioned full-wave simulation, and the Norton equivalent current source J_{eq}.

To compute the equivalent current the reciprocity theorem is exploited in two steps [21],[22]:

- First, the antenna is made operate in receiving mode when connected to a passive load with a resistance R_0. An independent transmitting source of volume V_S , described by an electric current density J_S , generates the fields E_S, H_S incident on the receiving antenna. The antenna used in the receiving mode is represented by its Norton equivalent circuit reported in Figure 3.1.2, with the current generator that is equivalent to the incident field coming from the transmitting antenna.

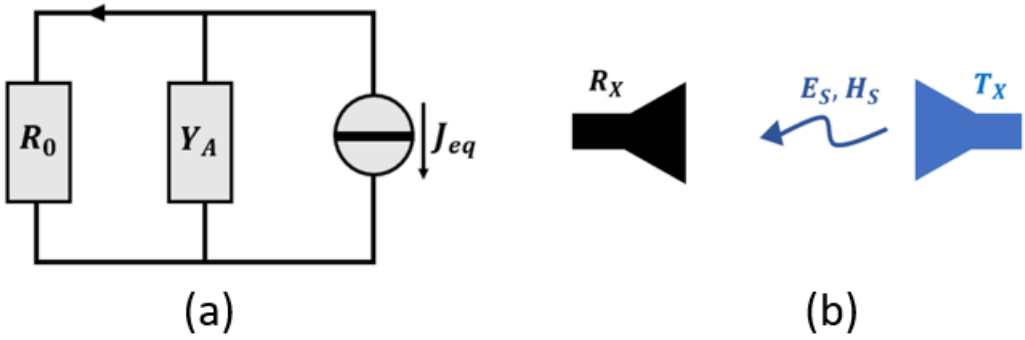

***Figure 3.1.2**: Norton equivalent circuit of the receiving antenna in receiving mode (a). The transmitting antenna is on and generates E_S, H_S (b).*

- Secondly, the receiving antenna is made operate in transmitting mode and connected to a sinusoidal voltage source of electromagnetic force U and an internal resistance R_0. The antenna generates the harvested fields E_H, H_H. This fictitious case is represented with the Norton equivalent circuit, showed in Figure 3.1.3.

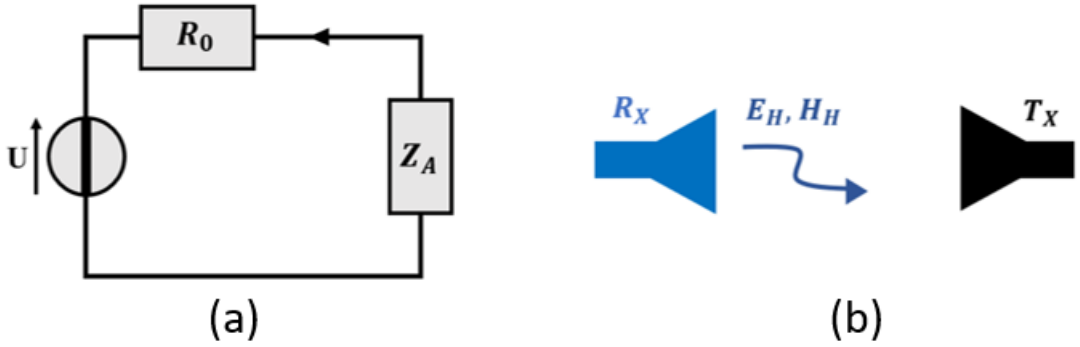

***Figure 3.1.3**: Thevenin equivalent circuit of the receiving antenna used in transmitting mode (a). The receiving antenna generate the fields E_H, H_H (b).*

The expression for the equivalent current density can be written by applying the reciprocity theorem is [21],[22]:

$$J_{eq}(\omega) = \frac{1 + R_0 Y_A(\omega)}{U} \int_{V_S} J_S(P_S) \cdot E_H(P_S)\, dV_S \,. \tag{3.1}$$

This expression is difficult to be computed directly, for this reason usually a uniform plane wave approximation is done. The approximation is reliable if the antennas are in their direction of maximum radiation and if they lie in the far-field region of each other. Such conditions could represent a problem for WPT applications since the operative context may lead the antennas to operate in the near-field or, in some cases, the mutual location and position may be unknown and thus not in the direction of maximum radiation. A way to exactly compute the equivalent current density regardless of the location and direction of the antenna is required. To do this in a simpler way, the equivalence theorem can be exploited.

A plane is placed in the middle of the two antennas and the transmitting antenna is substituted by the electric and magnetic equivalent surface currents evaluated on the plane, as in Fig. 3.1.4.

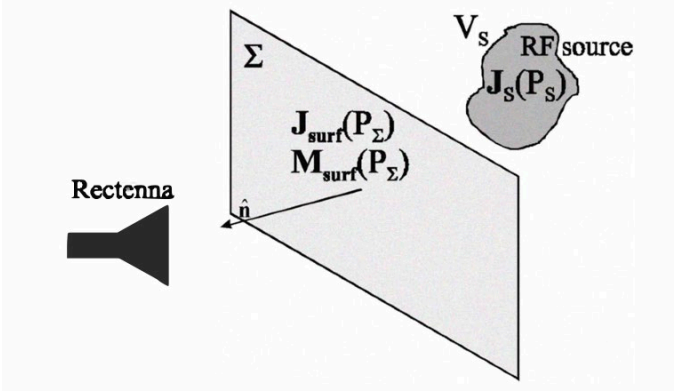

Figure 3.1.4*: Considered scenario for the evaluation of the equivalent surface current [21].*

The expressions for these on the plane are [21]:

$$J_{surf}(P_\Sigma) = \hat{n} \times H_S(P_\Sigma) \tag{3.2}$$

$$M_{surf}(P_\Sigma) = E_S(P_\Sigma) \times \hat{n}\,. \tag{3.3}$$

The volume source is then replaced in the expression of the equivalent current density [21],[22]:

$$J_{eq}(\omega) = \frac{1 + R_0 Y_A(\omega)}{U} \cdot \hat{n} \cdot \int_{\Sigma} [E_S(P_{\Sigma}) \times H_H(P_{\Sigma}) - E_H(P_{\Sigma}) \times H_S(P_{\Sigma})] d\Sigma \tag{3.4}$$

This can be easily evaluated by extracting the fields E_S, E_H, H_S, H_H from the electromagnetic simulations. This represents a scalable solution since it allows to simulate the transmitter and the receiver independently, extract the correspondent EM fields and then combine them to evaluate the $J_{eq}(\omega)$. This approach allows for halving the computational time that is usually requires to perform full-wave simulations of a wireless link. In fact, if the same antenna is used both in transmission and in reception, a single full-wave simulation is enough to have the necessary fields. Through a numerical algorithm, the scattered and harvested fields are generated from the fields extracted by the EM simulator with the proper reference system:

$$E_S = \begin{bmatrix} E_{Sx} \\ E_{Sy} \\ E_{Sz} \end{bmatrix} = \begin{bmatrix} E_{Sx}Re + jE_{Sx}Im \\ E_{Sy}Re + jE_{Sy}Im \\ E_{Sz}Re + jE_{Sz}Im \end{bmatrix} \quad , \quad H_S = \begin{bmatrix} H_{Sx} \\ H_{Sy} \\ H_{Sz} \end{bmatrix} = \begin{bmatrix} H_{Sx}Re + jH_{Sx}Im \\ H_{Sy}Re + jH_{Sy}Im \\ H_{Sz}Re + jH_{Sz}Im \end{bmatrix}$$

$$E_H = \begin{bmatrix} E_{Hx} \\ E_{Hy} \\ E_{Hz} \end{bmatrix} = \begin{bmatrix} -E_{Hx}Re - jE_{Hx}Im \\ E_{Hy}Re + jE_{Hy}Im \\ -E_{Hz}Re - jE_{Hz}Im \end{bmatrix} \quad , \quad H_H = \begin{bmatrix} H_{Hx} \\ H_{Hy} \\ H_{Hz} \end{bmatrix} = \begin{bmatrix} -H_{Hx}Re - jH_{Hx}Im \\ H_{Hy}Re + jH_{Hy}Im \\ -H_{Hz}Re - jH_{Hz}Im \end{bmatrix}$$

From these the equivalent surface current and its magnitude are rigorously computed after the specification of some parameters:

- Position of the integration plane.
- Area of integration.
- Resolution.

The resolution refers to the spatial discretization and it must be adjusted to have the proper integration area, as close as possible to the real one.

The evaluation plane is always orthogonal to the two antennas, as can be inferred by looking at the schematization in Fig. 3.1.4, and it is located exactly in the middle of the separation distance between the two, whereas the area of integration is chosen according to the dimension of the largest antenna present in the link.
Since the current source is linear, it does not depend on the load, so the available RF power delivered under conjugate match condition will be [21],[22]:

$$P_{AV} = \frac{|J_{eq}|^2}{8Re[Y_A(\omega)]}. \tag{3.5}$$

After this result, the entire system is analyzed with nonlinear analysis techniques like harmonic balance.
To see how the fields are effectively combined the integrand of the expression for J_{eq} is considered:

$$E_S \times H_H = \det\begin{bmatrix} \hat{\imath} & \hat{\jmath} & \hat{k} \\ E_{Sx} & E_{Sy} & E_{Sz} \\ H_{Hx} & H_{Hy} & H_{Hz} \end{bmatrix} =$$

$$= \left(E_{Sy}H_{Hz} - E_{Sz}H_{Hy}\right)\hat{\imath} + \left(E_{Sz}H_{Hx} - E_{Sx}H_{Hz}\right)\hat{\jmath} + \left(E_{Sx}H_{Hy} - E_{Sy}H_{Hx}\right)\hat{k}.$$

$$E_H \times H_S = \det\begin{bmatrix} \hat{\imath} & \hat{\jmath} & \hat{k} \\ E_{Hx} & E_{Hy} & E_{Hz} \\ H_{Sx} & H_{Sy} & H_{Sz} \end{bmatrix} =$$

$$= \left(E_{Hy}H_{Sz} - E_{Hz}H_{Sy}\right)\hat{\imath} + \left(E_{Hz}H_{Sx} - E_{Hx}H_{Sz}\right)\hat{\jmath} + \left(E_{Hx}H_{Sy} - E_{Hy}H_{Sx}\right)\hat{k}.$$

Since $\hat{n} \equiv \hat{k}$:

$$\hat{n} \cdot [E_S \times H_H - E_H \times H_S] = \left(E_{Sx}H_{Hy} - E_{Sy}H_{Hx}\right) - \left(E_{Hx}H_{Sy} - E_{Hy}H_{Sx}\right).$$

Having this result means that in the computation of the equivalent current all the fields contributing are transversal fields, hence distributed like a first-order Bessel function with a zero at the very center of the antenna. The evaluation of the equivalent current is further examined for different configuration of antennas.

3.2 Power Distribution

Once the procedure to efficiently compute the received power is illustrated, an analysis of the power distribution is performed for the different kind of antennas that have been previously described. Theoretically, Bessel Beams have a characteristic energy distribution such that each of the concentric ring carries approximately the same amount of energy. This means that for a Bessel Beam Launcher generating a zeroth-order Bessel function with a larger number of zeros, the energy contained in the main lobe is lower. Even if part of power is lost in the secondary rings, Bessel Beams show the same power efficiency of Gaussian Beams thanks to their focusing capabilities, for this reason, it is worth studying in depth this kind of non-diffractive solutions.
Here, the two configurations of Hybrid-TE-polarized Bessel Beam Launchers (1.5 and 3 cm radius) are considered and examined for different distances.
For each antenna configuration all the components of the field are analyzed to investigate the shape and power transport properties, both in terms of combined contributions and as singular ones.

3.2.1 Hybrid-TE Bull-Eye Leaky Wave Antenna with a radius of 1.5 cm

The H_z field has a J_0 distribution with two zeros and shows the maximum amplitude at the center of the antenna, as displayed in Figure 3.2.1. The E_z should have zero amplitude to have a pure TE mode, unfortunately this does not happen: with the loop antenna excitation it is not possible to represent a perfect Vertical Magnetic Dipole (VMD), so the resulting polarization of the mode is a hybrid-TE. All the other

components, for both electric and magnetic field, have a J_1 distribution as predicted, exhibiting a zero at the center of the antenna.

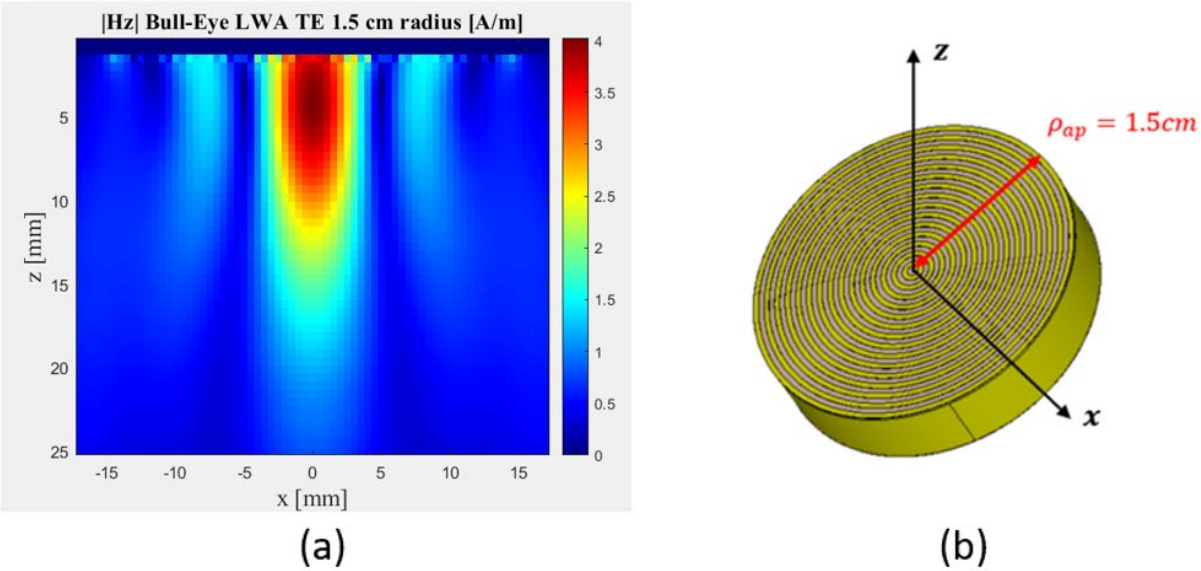

***Figure 3.2.1**: Profile of the z-component of magnetic field over the xz-plane (a). Considered antenna of radius 1.5cm (b).*

The z-component of the magnetic field has a relevant amplitude up to approximately a distance of 20 mm from the antenna radiating aperture, in agreement with the predicted non-diffractive range. H_z shows a peak in the range of 2-7 mm after which the amplitude decreases progressively as reported in Figure 3.2.1.

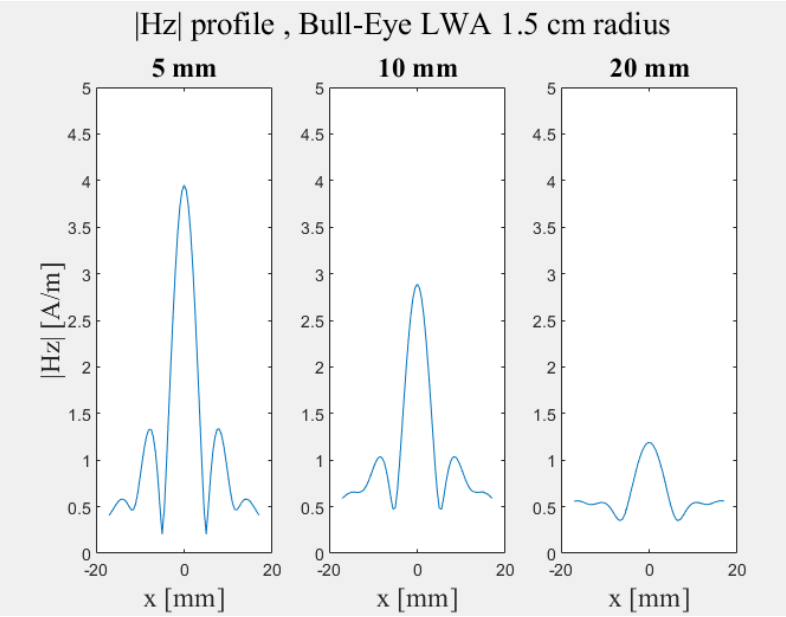

***Figure 3.2.2**: Hz profile for different distances from the antenna.*

The transversal and longitudinal components of the field are reported in Fig 3.2.3 and 3.2.4 at an arbitrary distance of 5 mm from the antenna, meaning we are in the non-diffraction range and the fields have the typical Bessel function distribution of zeroth or first order. By observing the z-component of the electric field, it is clear that the mode excited is a hybrid-TE. In fact, this component has an amplitude that is one order of magnitude lower with respect to E_t

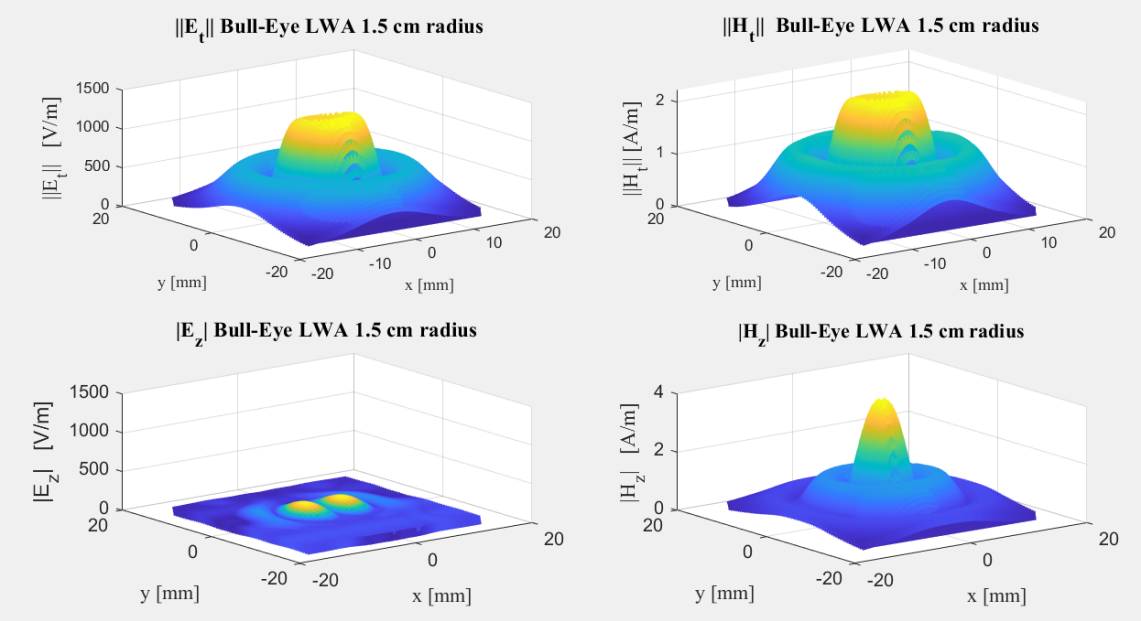

Figure 3.2.3- *Transversal and Longitudinal fields of BE-LWA of 1.5 cm radius at 5mm distance (perspective view).*

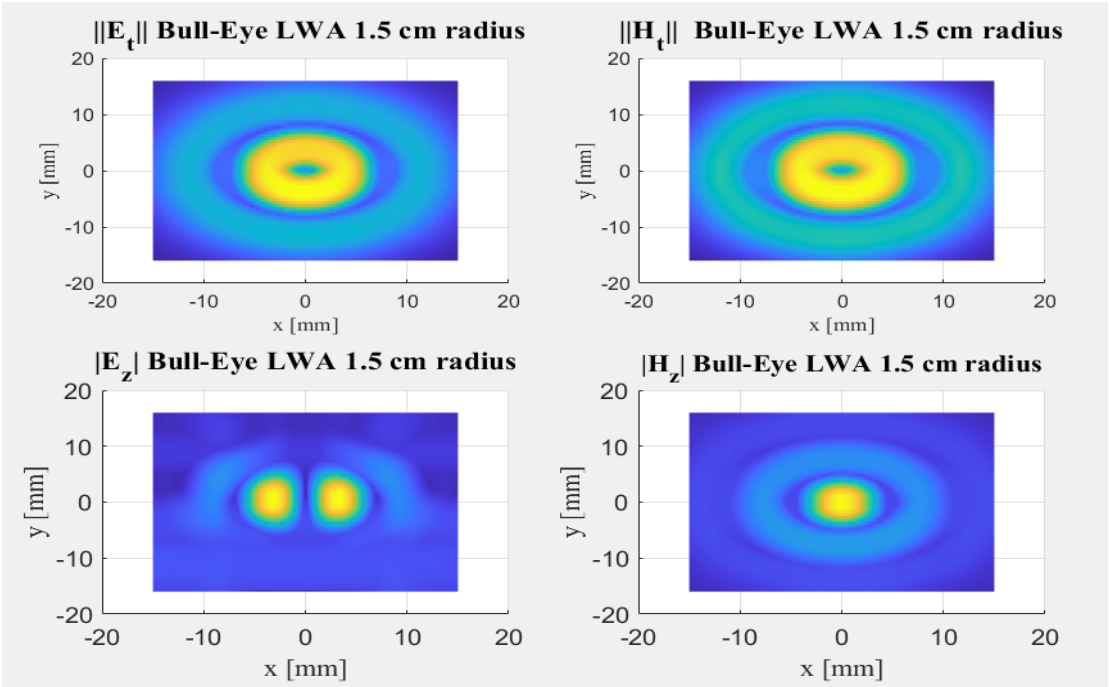

Figure 3.2.4- *Transversal and Longitudinal fields of BE-LWA of 1.5 cm radius at 5 mm distance (top view).*

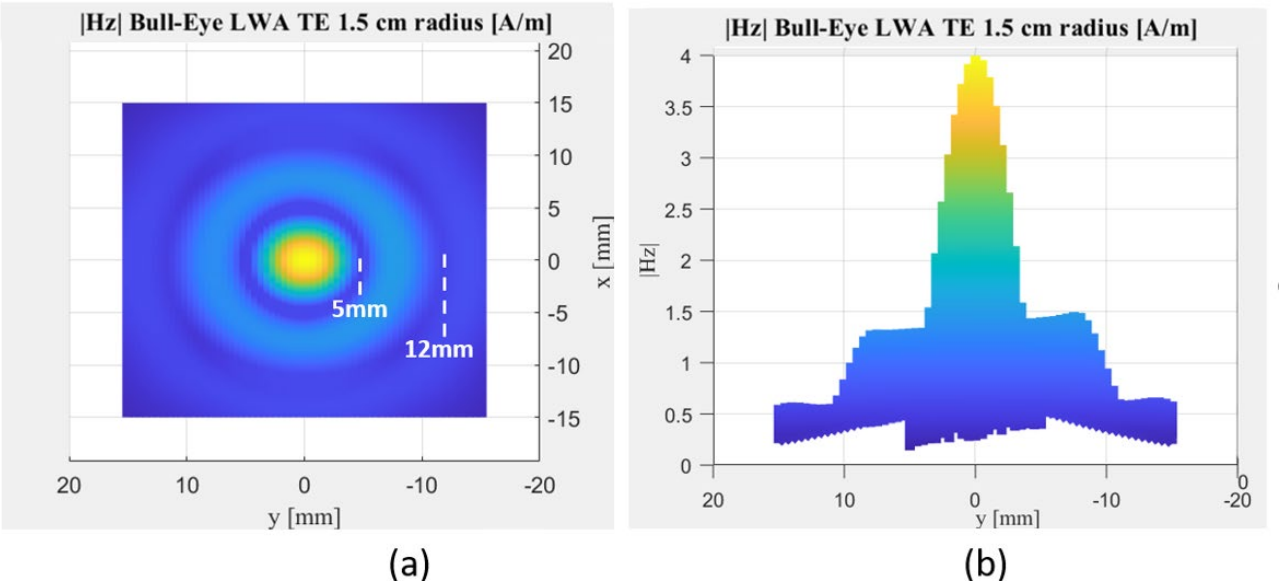

***Figure 3.2.5**: Hz component top view with position of the zeros (a) and front view (b).*

The magnetic field has the typical shape of a zeroth-order Bessel function with two zeros, showing a central beam with a diameter of 5 mm and a secondary ring of 12 mm, as shown in Figure 3.2.5.

Once the different components of the fields are observed, it is necessary to analyze how they combine each other. The equivalent surface current showed in Figure 3.2.6 has a zero in the center, in agreement with the distribution of the transversal components of the fields that follows a first-order Bessel function. When the fields are combined in the J_{eq} computation (3.4), the resulting field shows four main lobes. These four main lobes lie in the x-z and y-z planes, as shown by the equivalent current distribution plotted in Figure 3.2.6. The main lobe is considered the aggregation of these four lobes, because that is where most of the power is concentrated. It has an overall diameter of approximately 7 mm in the non-diffraction range, whereas it enlarges becoming less and less focused as soon as the 20 mm of non-diffraction range are exceeded. After the end of the non-diffraction range the directivity is completely lost. The dimension of the J_{eq} main lobe is almost the same of the H_z main lobe

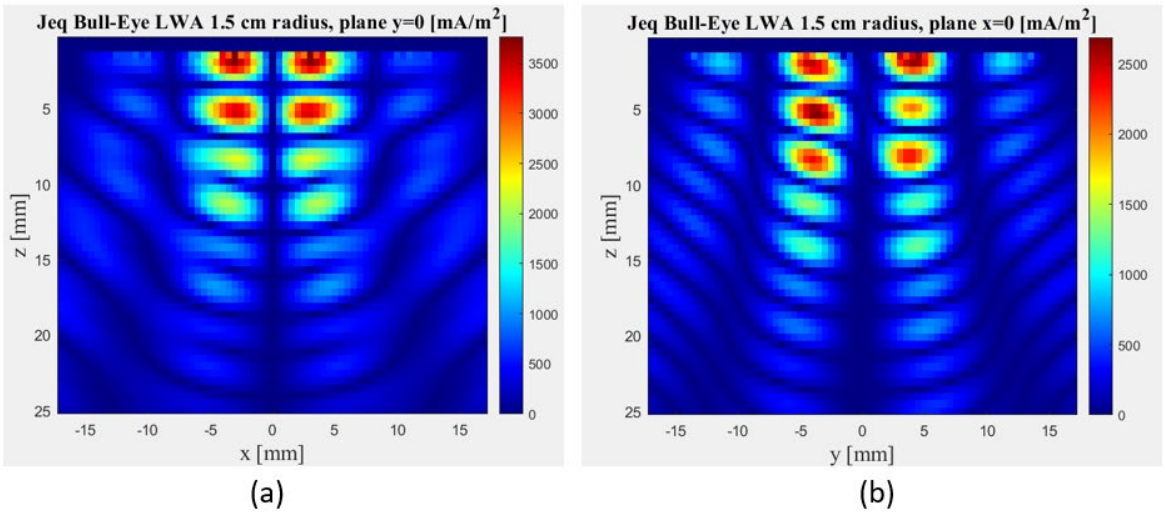

***Figure 3.2.6**: Equivalent current distribution of the BE-LWA with 1.5 cm radius over the xz-plane (a) and yz-plane (b).*

By considering the different components coming from the integrand in the expression (3.4) for the equivalent surface current it is possible to evaluate the contribution in terms of power coming from the different lobes.

In Figure 3.2.7, the components of J_{eq} are represented, showing a clear first-order Bessel distribution. The only component that is relevant for the computation of the equivalent current is the z-component.

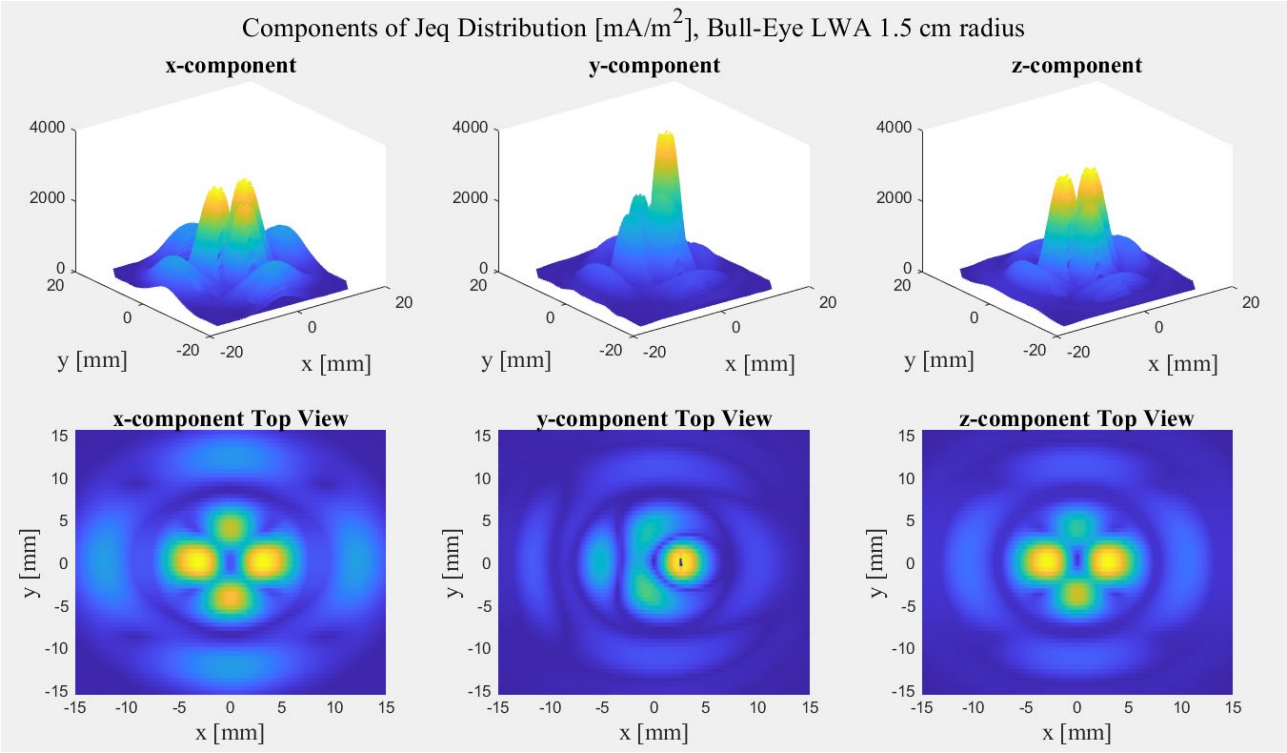

***Figure 3.2.7**: Equivalent current distribution components of BE-LWA 1.5cm radius from perspective and frontal view at z=5mm distance.*

These plots in Figure 3.2.7 are computed for a distance of 5 mm from the antenna aperture. The four main lobes are compact enough, exhibiting zero intensity in the center, with a spot of about 1mm. To evaluate the power distribution, four different distances between transmitter and receiver are considered, from 5 to 20 mm. In all the following measurements, a transmitting antenna input power of 27 dBm is considered.

To evaluate the received power, computation of the equivalent current is conducted, following the same procedure that has been previously explained. It is observed in Fig. 3.2.6 that four lobes are present: two distributed along the x-axis (a), two along the y-axis.

The general procedure to evaluate the power coming from the different lobes of the surface current distribution exploits the above-described method based on the reciprocity theorem. The principle is to modify the integration area depending on the dimension of the beam:

- The four lobes coming from the J1 distribution of transversal fields are considered as main lobe The integration area has a given side, according to the position of the first zero, such that only the contribution of the main lobes is considered. At this point, the power contribution from the main lobes is known.
- The procedure is then repeated for the second ring. The position of the second zero determines the integration area that now includes the main lobes and the secondary ones. After the integration and the computation of the received power, the contribution coming from the main lobes is subtracted. This way, the received power contribution only belongs to the secondary lobes.
- Same procedure for other secondary rings, each time removing the contribution of internal lobes.

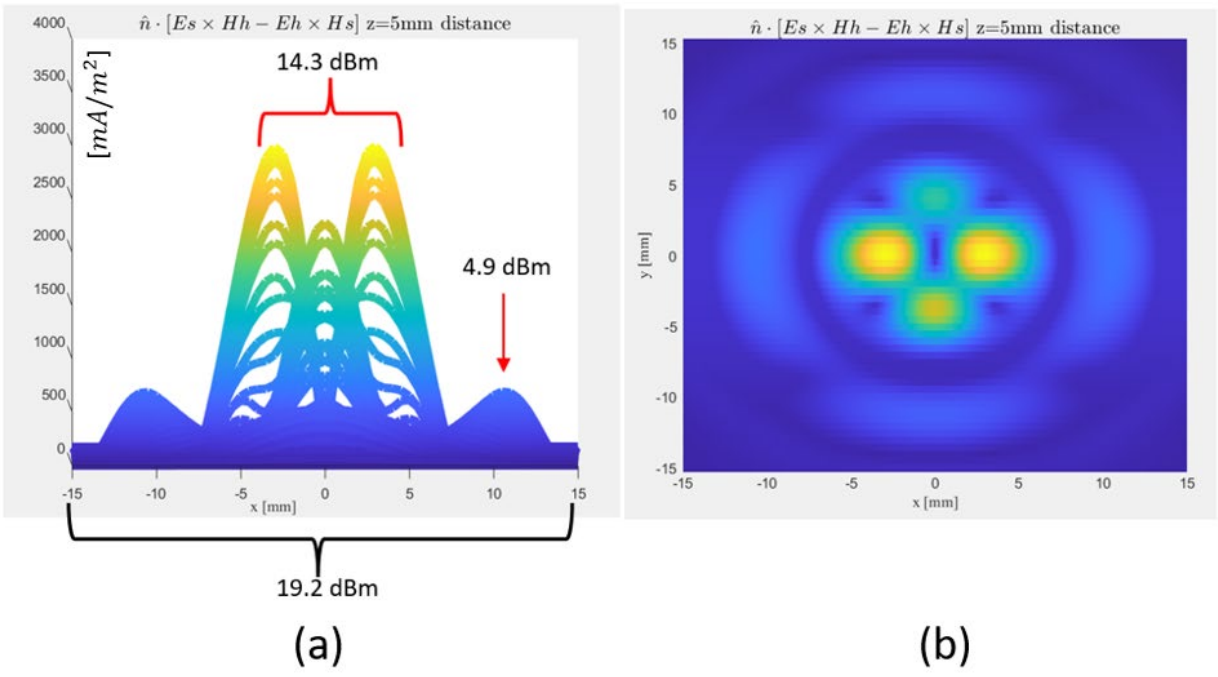

***Figure 3.2.8**: Power distribution at 5mm distance from the antenna (a) and top view of Jeq distribution at 5mm distance from the antenna (b) for input power of 27 dBm.*

In Figure 3.2.8, the distribution of power among the different lobe is reported: at 5 mm distance from the antenna, the overall received power is 19.2 dBm. 14.3 dBm

comes from the main four lobes, whereas the remaining 4.9 dBm comes from the secondary ring.

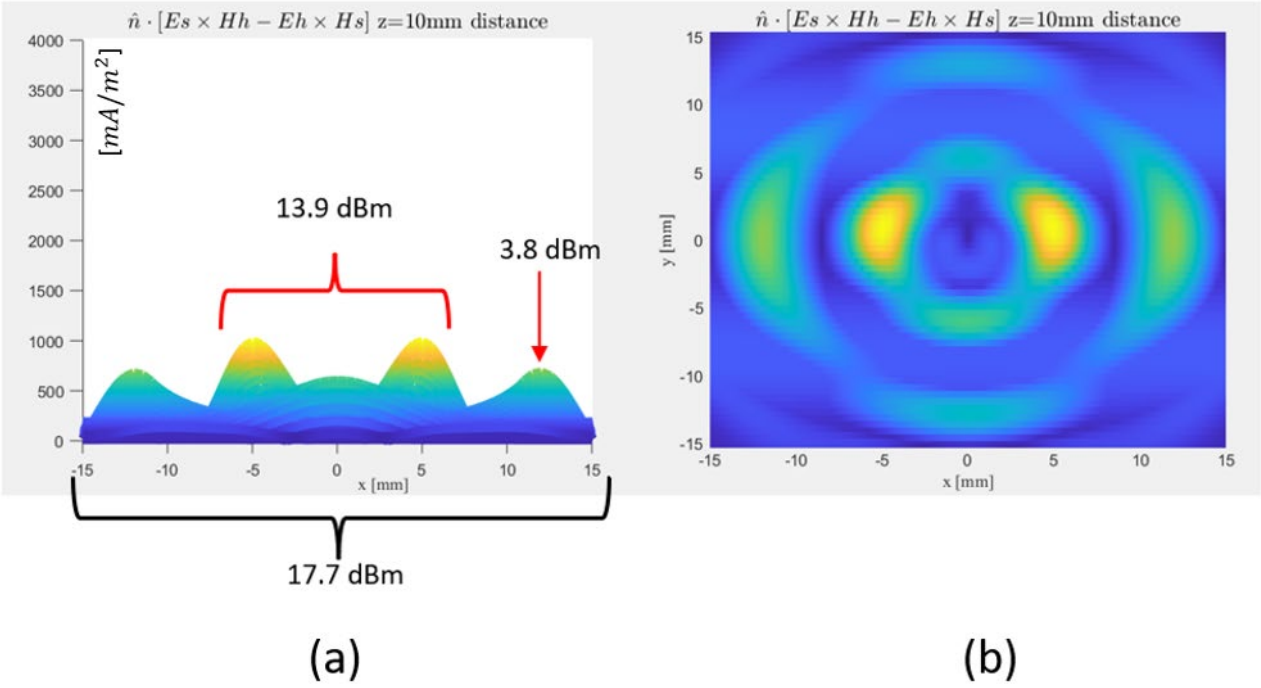

***Figure 3.2.9**: Power distribution at 10 mm distance from the antenna (a) and top view of Jeq distribution at 10 mm distance from the antenna (b) for input power of 27 dBm.*

In Figure 3.2.9, the same procedure is used: as the distance from the antenna increases, the lobes are less and less directive showing a larger area of minimum at the centre. As the distance increases there is a spread of the four lobes and of secondary ring. As a result, the integration area considered for the main lobe is enlarged but it actually has a larger zone of minimum at the centre. At the same time the secondary ring loses significancy for increasing distance. The larger integration area and the attenuation of the secondary ring explains the percentage of increasing power in the main lobe for increasing distance, reported in Table 1.

Up to 20-mm from the antenna, the power is concentrated in the central part, since for increasing distances also the secondary lobes are strongly reduced. For distances overcoming the non-diffraction range, the concept of main lobe and secondary lobe is

lost since the fields do not maintain the typical Bessel-function shape. All the values obtained for the power distribution are listed in Table 1.

Distance	Total Received Power [dBm]	Power from main lobe [dBm]	Power from secondary lobe [dBm]	% Power in main lobe
5mm	19,2 dBm	14,3 dBm	4,9 dBm	74%
10mm	17,7 dBm	13,9 dBm	3,8 dBm	78%
15mm	14,8 dBm	12,2 dBm	2,6 dBm	82%
20mm	11,8 dBm	10,6 dBm	1,2 dBm	89%

***Table 1**: Power distribution of the surface current for different distances from the antenna for input power of 27 dBm.*

3.2.2 Hybrid-TE Bull-Eye Leaky Wave Antenna 3cm radius

The second Bessel Beam launcher analyzed is the one with radius $\rho_{ap} = 3cm$ and that has all the other descriptive parameters of the antenna unchanged.

In figure 3.2.10, the component of the magnetic field Hz is represented as a function of different distances (z [mm]) and spatial coordinates (x [mm]) over the plane y=0. The field is simulated and extracted after a full-wave EM simulation up to 50 mm both in the direction of propagation and in the transversal direction. For a distance up to 1 mm, there are some unusual peaks, therefore those values may be referred to points too close to the antenna surface that are not correctly exported by the full-wave software.

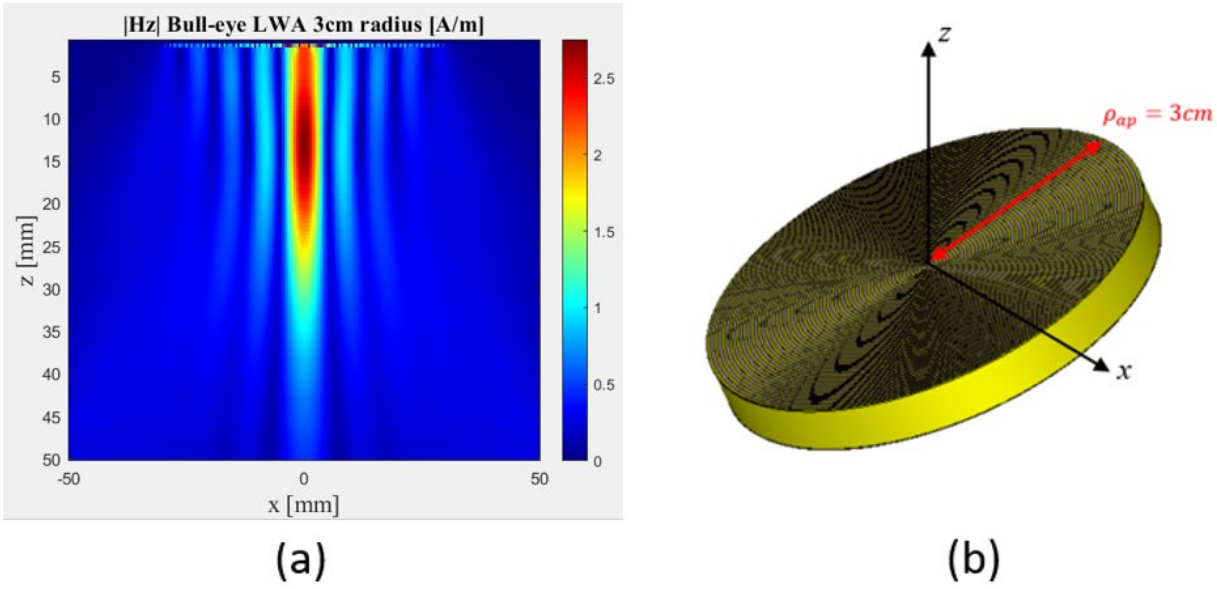

Figure 3.2.10*: Profile of the z-component of magnetic field over the xz-plane (a). Considered antenna of radius 3cm (b).*

The central beam of the H_z component presents maximum intensity for a range of distances going from 10 to 16 mm approximately, after which it starts decreasing, as observed in Fig. 3.2.10. It remains relevant almost up to the predicted theorical non-diffractive range of 40 mm. By comparing the profile of H_z of the Bessel Beam Launcher with different radius, it can be noticed that for the BB LWA of 1.5 cm radius, the z-component of magnetic field is extremely attenuated at 20 mm distance from the antenna (Fig. 3.2.2), whereas, when roughly doubling the radius to 3 cm, the field experiences the same attenuation at 40 mm distance (Fig. 3.2.11), coherently with the predicted nondiffractive range.

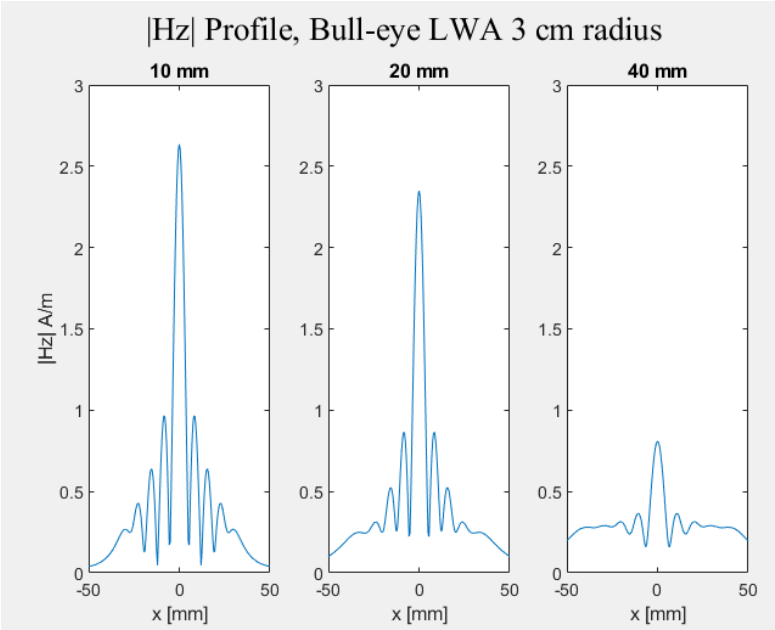

***Figure 3.2.11**: Hz profile for different distances from the antenna.*

Considering the fields of the Bull-Eye LWA with 3 cm radius at the generic distance of z = 5mm, it is visible that now the number of zeros in the Bessel function is increased to four, as shown in Figure 3.2.12 and Figure 3.2.13.

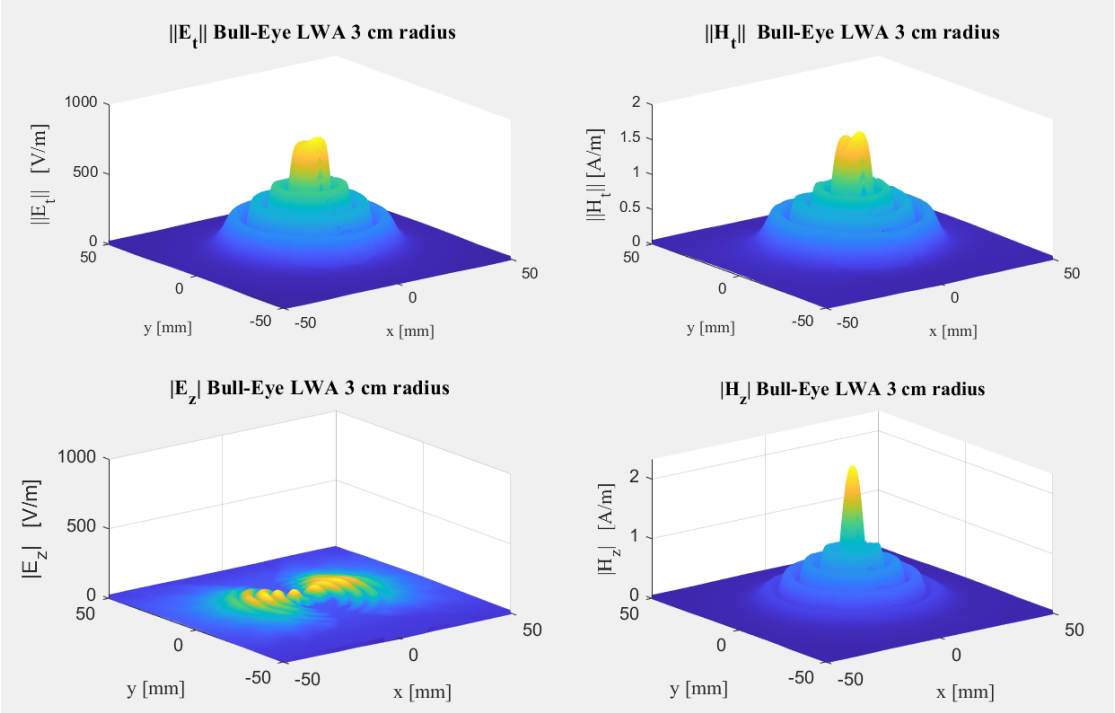

***Figure 3.2.12**- Transversal and Longitudinal fields of BE-LWA of 3 cm radius at 5mm distance (perspective view).*

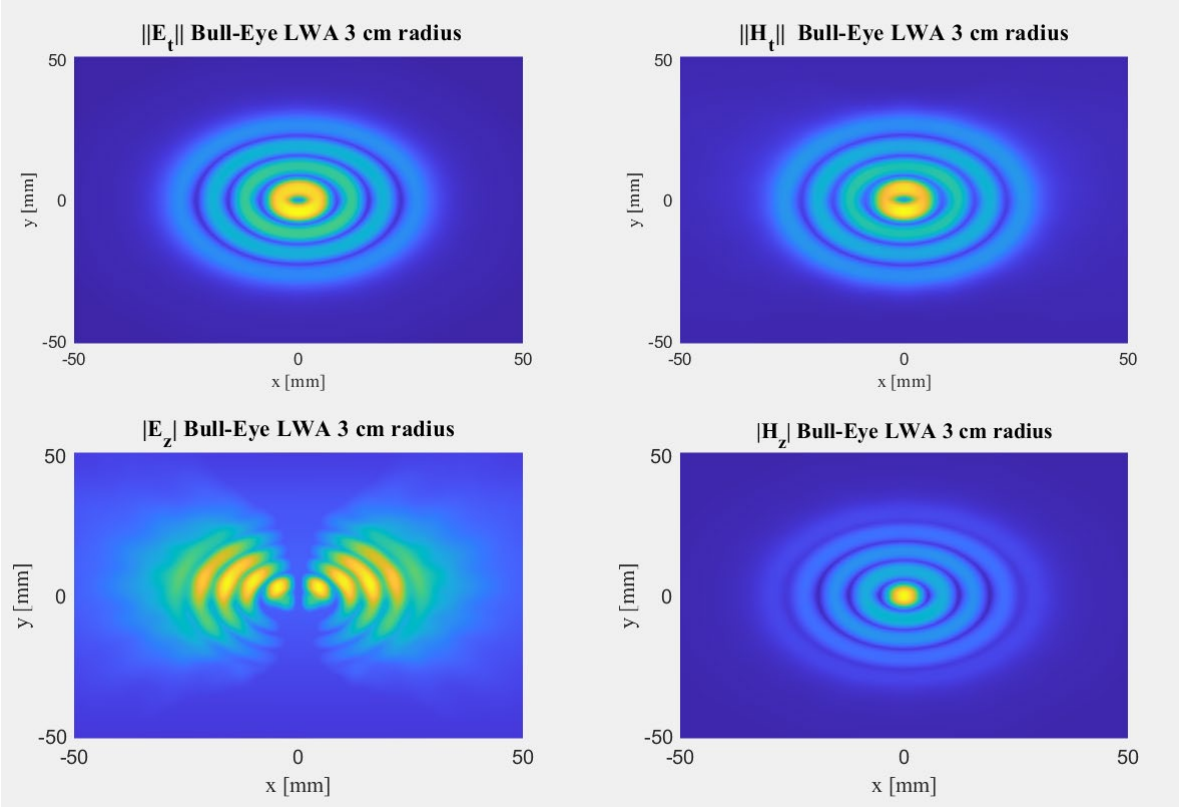

Figure 3.2.13*- Transversal and Longitudinal fields of BE-LWA of 3 cm radius at 5mm distance (top view).*

It is verified even in this case that the excitation with loop antenna does not allow to have a pure TE mode, since the z-component of the electric field which is not exactly zero. Still, this component has one order of magnitude lower with respect to the transversal ones, so it can be considered an Hybrid – TE excitation.

As predicted, the transversal components of the electric and magnetic field behave as $J_1(k_\rho \rho)$ with a zero at the very center of the antenna, whereas the longitudinal

component of the magnetic field follows a $J_0(k_\rho \rho)$ distribution with four zeros. The positions of the zeros are reported in Figure 3.2.14.

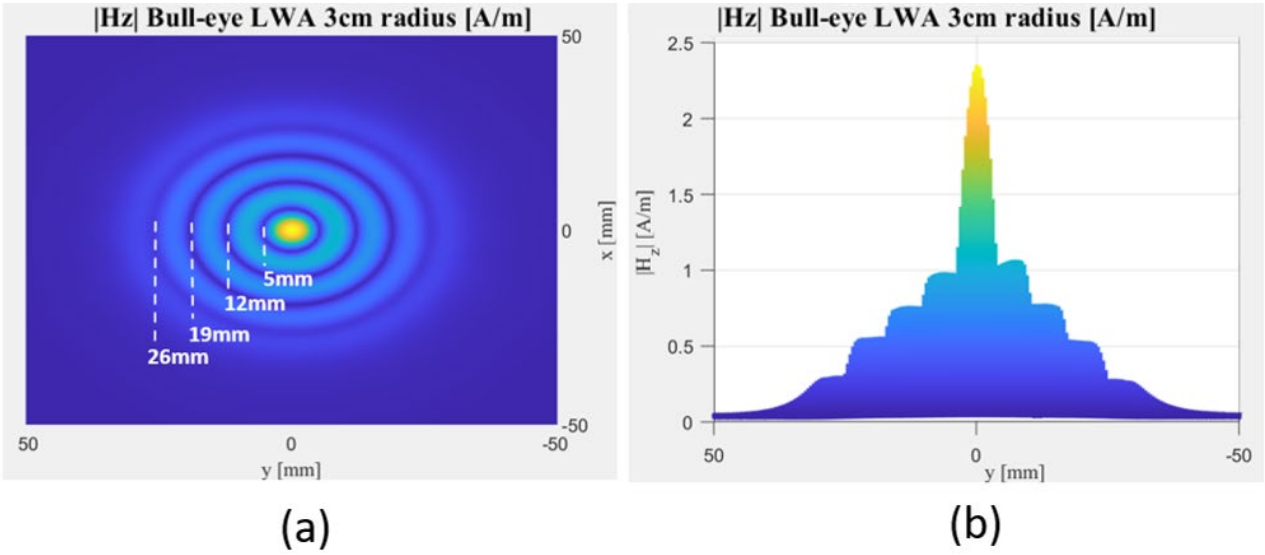

***Figure 3.2.14**: Hz component position of the zeros and top view (a) and front view (b).*

Considering now the distribution of the equivalent current J_{eq} over the xz-plane and over the yx-plane, as reported in Figure 3.2.15, it clearly shows the same shape compared with the one emitted by the smaller Bessel Beam Launcher, but it maintains the focusing up to a larger distance. The drawback is that, having more zeros in the Bessel function, the power lost in secondary rings is larger.

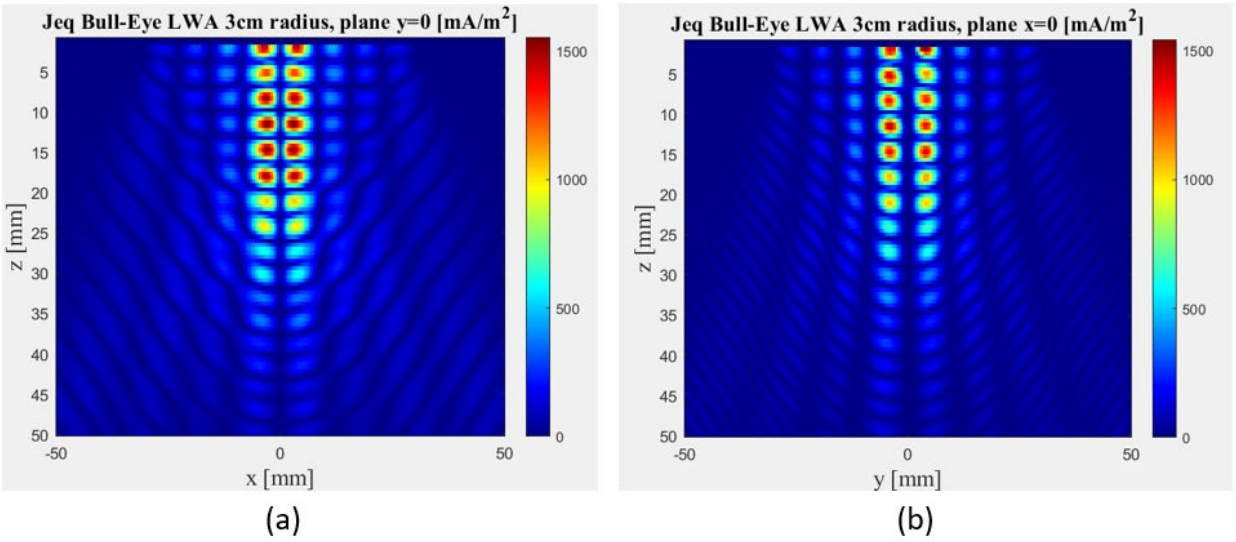

***Figure 3.2.15**: Equivalent current distribution of the BE-LWA with 3 cm radius over the xz-plane (a) and yz-plane(b).*

The components of the equivalent current distribution reported in Figure 3.2.16 are referred to a distance of 5 mm from the antenna and clearly, they follow the distribution of the transversal fields with a larger number of zeros with respect to the smaller Bessel Beam Launcher.

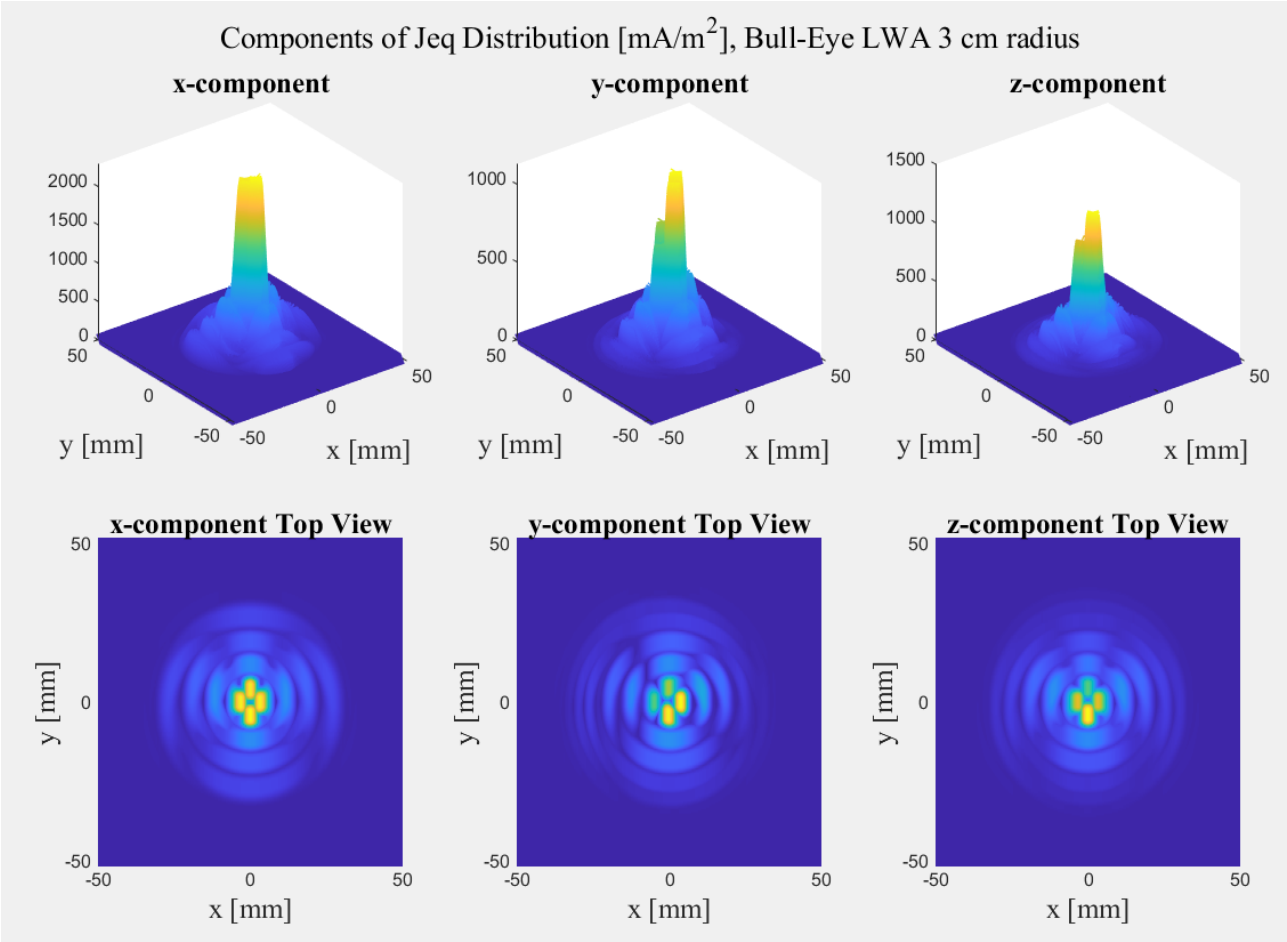

***Figure 3.2.16**: Equivalent current distribution components of BE-LWA 3cm radius from perspective and frontal view at z=5mm distance.*

This distribution with four small lobes comes from the fact that transversal components of both electric and magnetic field are distributed as a first-order Bessel function over the x axis and over y axis. This can be inferred by observing the E_x, E_y, H_x, H_y components at a generic distance of 5 mm from the antenna, as plotted in Fig. 3.2.17 and Fig. 3.2.18.

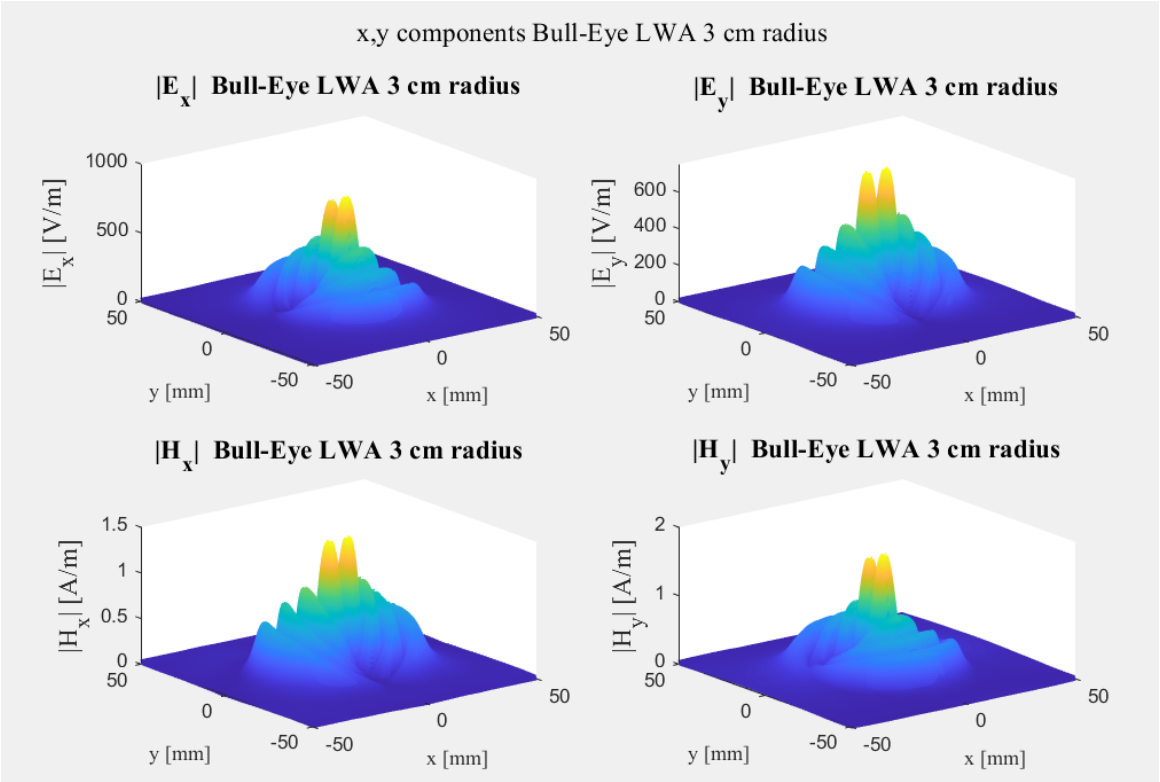

***Figure 3.2.17**: x,y components of the E,H fields considering BB LWA of radius 3cm at z=5mm from the antenna.*

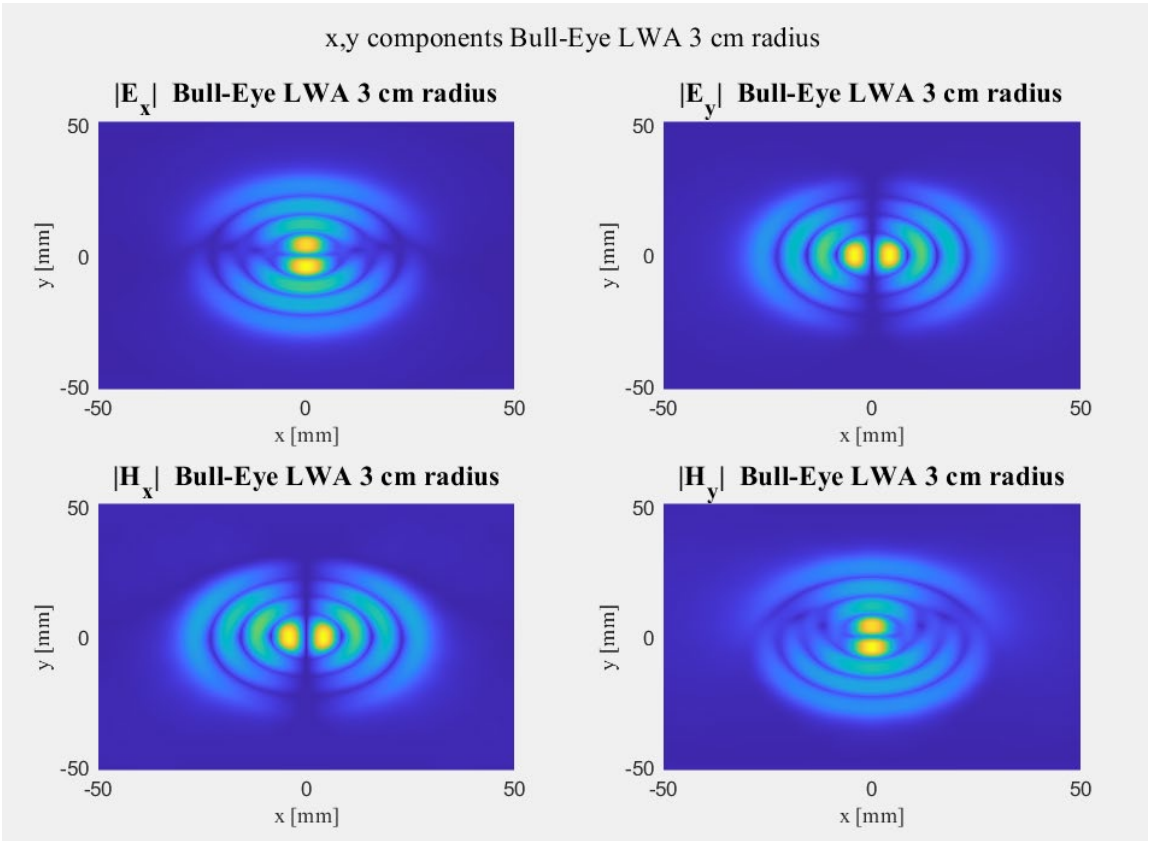

***Figure 3.2.18**: x,y components of the E,H fields considering BB LWA of radius 3cm at z=5mm from the antenna (top view).*

The position of the zeros after combining the fields is slightly changed with respect to the only H_z component. In H_z we have the main lobe at the center of the antenna, and it has a radius of 5 mm. When the fields are combined, most of radiation is concentrated in an overall radius of 8.5mm, as in Figure 3.2.19.

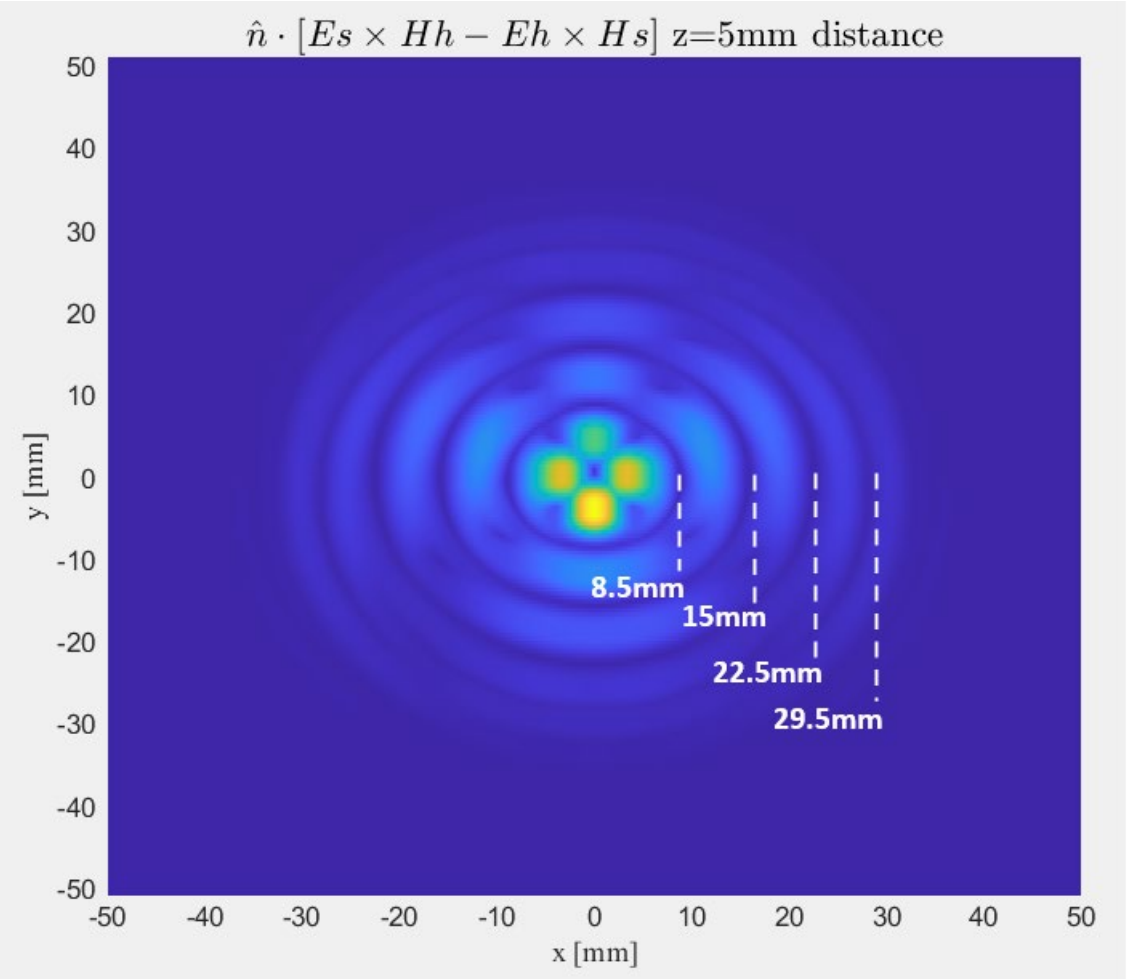

***Figure 3.2.19**: Zeros of equivalent current distribution of BE-LWA of 3cm radius.*

To evaluate the power that comes from the "main" lobe and from the secondary ones, the integration area is changed depending on the position of the zeros. For the Bessel Beam Launcher of radius 1.5 cm, the procedure is straightforward because there is only one main lobe and one secondary lobe. Moreover, in this case, a 27-dBm input

power is provided to the transmitting antenna. Considering a distance of 10mm from the antenna, reported in Figure 3.2.20:

- The main lobe is considered to be the aggregation of the four lobes coming from the J_1 Bessel distribution of transversal fields. The integration area has a 8.5 mm side, according to the position of the zero. The main lobe intended in this way will carry 9.9 dBm of power.
- For the secondary lobe the position of the zero is at 15mm, so the integration is made according to this area and then it is subtracted the contribution of the main lobe obtaining 5.8 dBm power in the secondary lobe.
- The same procedure is carried out for other lobes, each time removing the contribution of internal lobes.

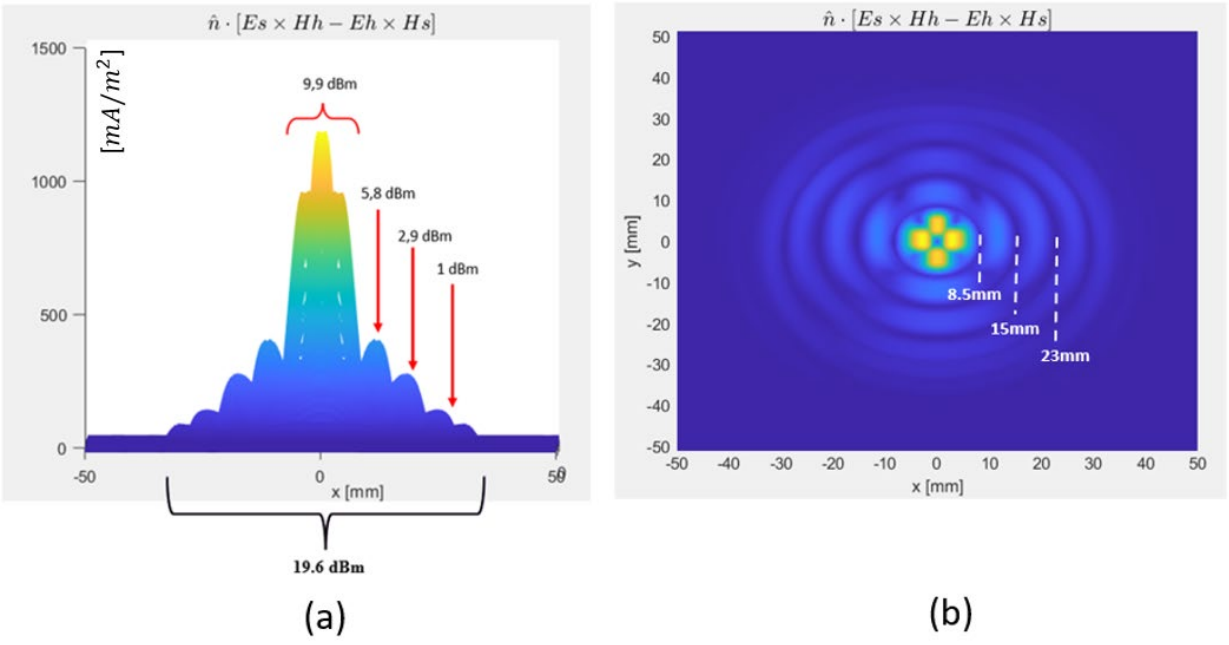

***Figure 3.2.20**: Power distribution at z=10 mm of the BB LWA with radius 3cm (a) and positions of zeros (b) for input power of 27 dBm.*

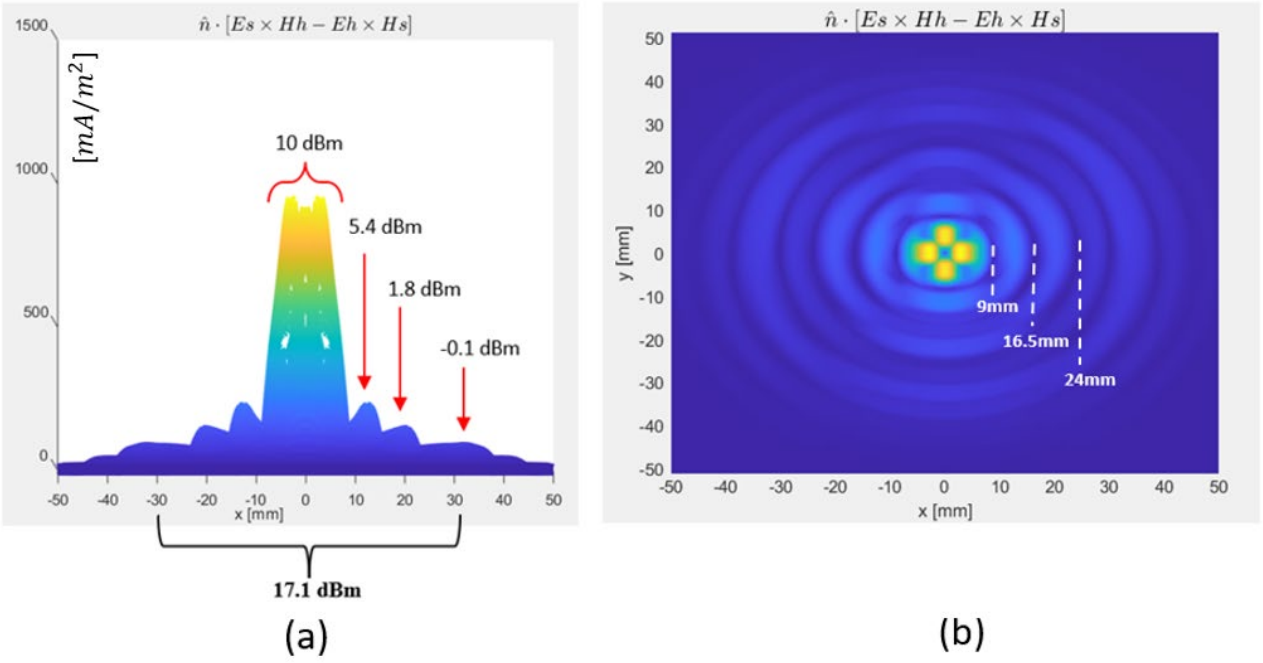

***Figure 3.2.21**: Power distribution at z=20 mm of the BB LWA with radius 3cm (a) and positions of zeros (b) for input power of 27 dBm.*

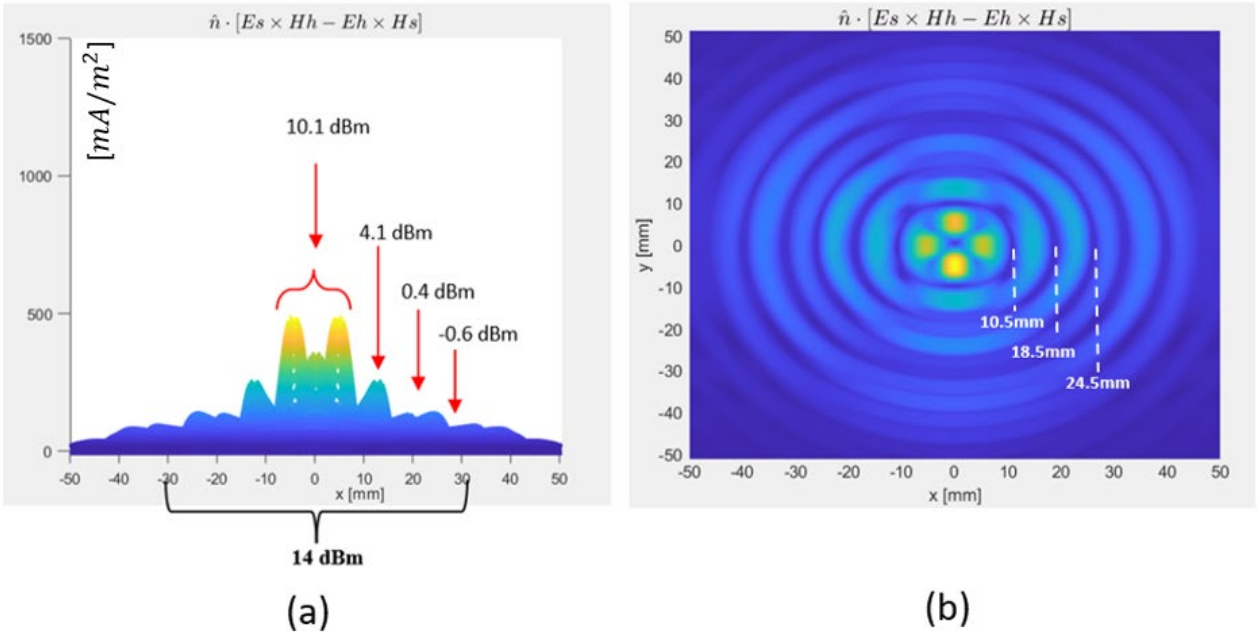

***Figure 3.2.22**: Power distribution at z=30 mm of the BB LWA with radius 3cm (a) and positions of zeros (b) for input power of 27 dBm.*

The power distribution among different rings is reported in Fig. 3.2.20, Fig. 3.2.21, Fig. 3.2.22 respectively, for a distance of 10mm, 20mm and 30mm from the antenna. In general, most of the power is contained in the main lobe. It can be observed that, in the region closer to the antenna, the secondary lobes are more relevant carrying more

power, becoming less and less defined as the distance from the antenna increases. As the distance increases, the main lobe apparently has a lower intensity, but in fact it carries approximately the same amount of power for the three simulated distances. This happens because the radius delimitating the region of the main lobe is slightly enlarged for increasing distances. At the expense of a larger antenna and of an increased portion of power lost in secondary lobes, the directivity is kept constant for a longer distance. In Table 2, the specific percentage of power contained in the main lobe for different distances is summarized.

Distance	Total Received Power [dBm]	Power from main lobe [dBm]	Power from secondary lobes [dBm]	% Power in main lobe
5mm	20,2 dBm	9,8 dBm	10,4 dBm	48%
10mm	19,6 dBm	9,9 dBm	9,7 dBm	50%
15mm	18,2 dBm	9,9 dBm	8,3 dBm	54%
20mm	17,1 dBm	10 dBm	7,1 dBm	58%
25mm	15,2 dBm	9,8 dBm	5,4 dBm	64%
30mm	14 dBm	10,1 dBm	3,9 dBm	72%
35mm	12,7 dBm	9,2 dBm	3,5 dBm	72%
40mm	12,3 dBm	9 dBm	3,3 dBm	73%

***Table 2**: Summary table with power distribution of BB LWA with r=3cm for input power of 27 dBm.*

Chapter 4: Receiving side

In this chapter a complete characterization of a WPT link involving different configurations is presented: firstly, Bessel Beam Launchers are further examined when exploited as transmitter and receiver. Secondly, further investigations have been conducted to replace the Bessel Beam Launcher as receiver in favour of planar solutions with similar performances and reduced dimensions. Finally, for two different final receiver configurations, rectifying circuit is analysed, and results are presented.

4.1 Receivers

Once the structural and power transport properties of Bessel Beam Launchers are fully characterized, it must be investigated their behaviour when they are used in a WPT link. In these first link budgets considered, the Bessel Beam Launchers based on Leaky Radial Waveguide are employed both in transmission and reception. The system transmits and receives propagating Bessel Beams. The radiative near-field (Fresnel region) is investigated, exploiting the diffraction-free zone of Bessel Beam Launchers. It can be stated that this is the case of electromagnetically long antennas, since the physical dimension of the Bessel Beam Launchers under examination is larger than a half-wavelength. For this type of antennas, the difference between near field (radiative or reactive) and far field is given in terms of the Fraunhofer distance:

$$d = \frac{2D^2}{\lambda},$$

with D diameter of the antenna and λ wavelength of the emitted radiation. The Fraunhofer distance define the start of the far field region if $d \gg D$ and $d \gg \lambda$.
The radius of the Bessel Beam Launchers are 1.5 cm and 3 cm, while the wavelength at 30 GHz is approximately 1 cm. Considering the non-diffraction range of the two antennas (respectively about 20 mm and 40 mm), it has been chosen to focus on a range

of distance between 10 and 40 mm. Straightforwardly, the distances taken in consideration belong to the near-field region.

The setup for the link budget is based on the numerical model deeply explained in Chapter 3 and reported in Figure 4.1.1., which evaluates the J_{eq} exploiting the reciprocity and the equivalence theorem. In this analysis the transmitting and receiving antennas are always aligned in their direction of maximum radiation with the evaluation plane in the middle of the twos, and the received power is computed for different distances between the launchers.

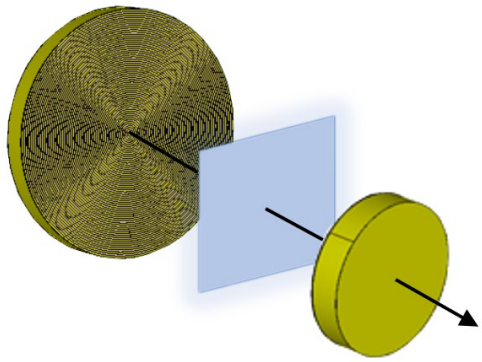

Figure 4.1.1*: Link budget setup for the evaluation of the received power.*

It is always considered an input power given to the transmitting antenna of 27 dBm (0.5 W). The first two link considered are:

- Bessel Beam Launcher of radius 1.5 cm both in transmission and reception.
- Bessel Beam Launcher of radius 3 cm both in transmission and reception.

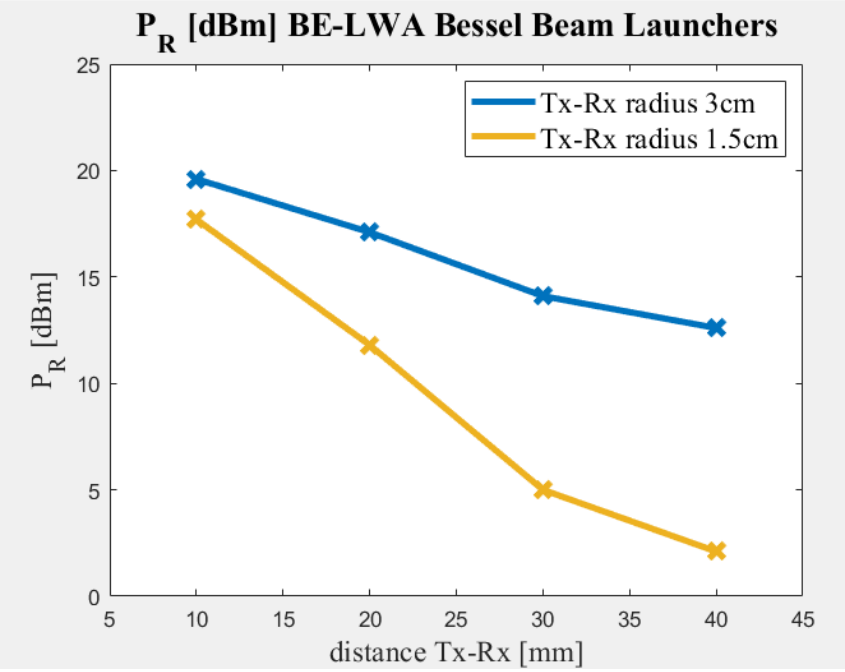

***Figure 4.1.2**: Received power for different distances using links with same transmitter and receiver for input power of 27 dBm.*

Clearly, the smaller Bessel Beam Launcher, having a non-diffraction range of 20 mm, shows a rapidly decay of the received power over the distance, as shown in Figure 4.1.2. By using the Bessel Beam Launcher of radius 3cm both in transmission and reception it is possible to gain almost 10 dBm at distance of 40 mm between transmitter and receiver with respect to the link with smaller antenna. Therefore, can be stated that in order to reach long distance, larger antennas have to be implied.

The second link presents satisfying results in terms of received power, however, when the field of application regards wearable or implantable devices it is unconceivable to use in reception such a space-consuming antenna.

As a trade-off between these two links, a third one is considered: since the constraints regarding the dimensions of the transmitting antenna are more relaxed, it is possible to use the Bessel Beam Launcher of radius equals to 3 cm, while in reception the Bessel Beam Launcher of radius 1.5cm is maintained (for the sake of simplicity, it is referred as 'mixed configuration'). Finally, for the sake of completeness another configuration is considered, using a resonant cavity with a PRS (Partially Reflective Surface). The

design of this Bessel Beam Launcher is not going to be discussed in details, limiting the analysis to the obtained link budget. The structure reported in Fig. 4.1.3 shows a FPC fed by a coaxial cable, whose top layer is substituted with an equivalent impedance sheet (PRS) of value X_S =j25 Ω at 30 GHz. For a TM excitation the z-component of the electric field performs a zeroth-order Bessel function distribution. The radius of this antenna is 1.5 cm. The use of PRS with the proper equivalent impedance sheet is proved to be a reliable method to approximate realistic surfaces and reduce the full-wave simulation computational time.

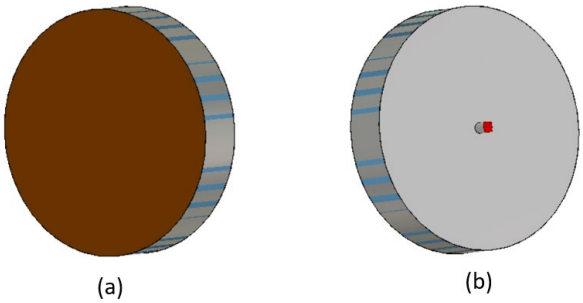

***Figure 4.1.3**: Resonant cavity with PRS (a), excited by a coaxial cable (b).*

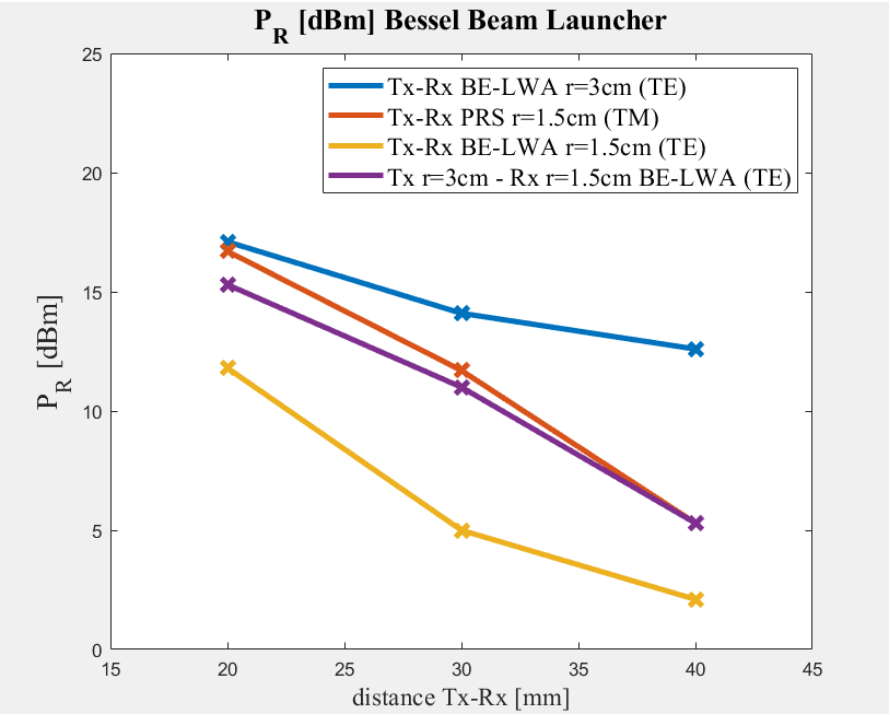

***Figure 4.1.4**: Comparison of received power for different distances of previous links considered and link with mixed configuration of receiver/transmitter for input power of 27 dBm.*

The mixed configuration, whose link budget is reported in Figure 4.1.4, shows intermediate performance when compared to the previous two examined links. This is one possible solution for having reasonable dimension of the received antenna and, at the same time, achieving satisfying results in terms of received power. Although the radius is fixed to 1.5 cm, the Bessel Beam Launcher with PRS exciting a pure-TM mode shows much better performances with respect to the Bull-Eye LWA exciting a Hybrid TE. The BB Launcher with PRS outperforms also the mixed configuration with BE-LWAs. It has to be said that the pure TM Bessel Beam Launcher equipped with the PRS is described by a more ideal configuration with respect to the annular strip grating one. All the specific values of the power received are collected in Table 3.

Distance Tx-Rx	**P_R BE-LWA r=3cm (Tx-Rx)**	**P_R BE-LWA r=1.5cm (Tx-Rx)**	**P_R BE-LWA mixed link**	**P_R PRS (TM) r=1.5cm**
20mm	17,1 dBm	11,8 dBm	15,3 dBm	16,7 dBm
30mm	14,1 dBm	5 dBm	11	11,7 dBm
40mm	12,3 dBm	2,1 dBm	5,3 dBm	5,3 dBm

Table 3: *Table with specific values of power received for the different link configurations for input power of 27 dBm.*

After this link budget evaluation, it can be stated that fundamental element in Bessel Beam Launchers is represented by the non-diffraction range. To give an explicative representation of the geometry behind the non-diffraction range the link with BB Launcher (BE-LWA) of radius 3 cm as transmitter and the one of radius 1.5 cm as receiver is considered in Figure 4.1.5. The link budget evaluation can be seen as a progressive distancing between the two antennas: when the distance between the twos is1 cm for both antennas we are in the region of maximum radiation. Up to 3 cm the two antennas are each other in the region of maximum intensity of the magnetic field and the results are satisfactory. As the distance increase and reaches 4 cm this is no longer true, the two antennas are no longer in the desired range of maximum and the received power decrease more rapidly, losing 5 dBm in the last cm. For this reason,

with this link, it is not convenient to observe over 4 cm between transmitter and receiver.

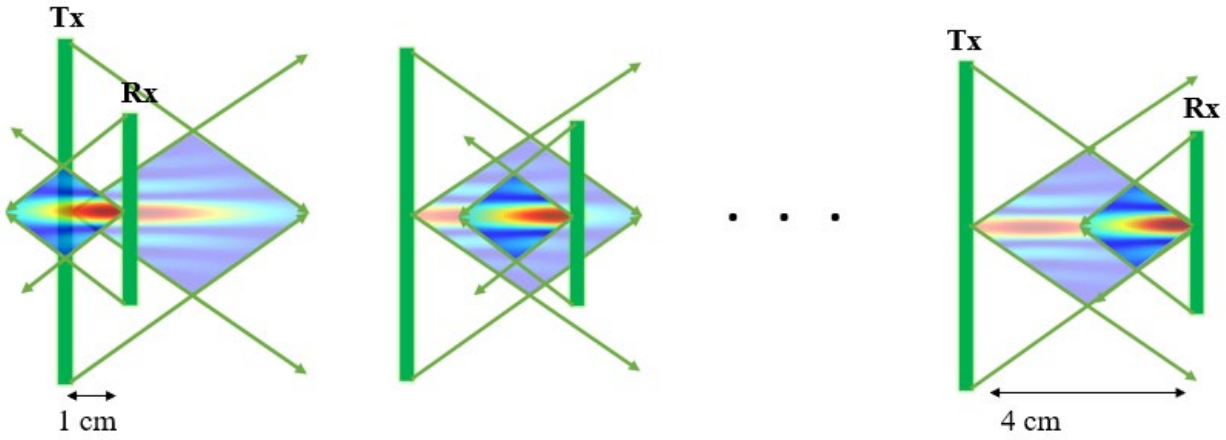

***Figure 4.1.5**: Geometry behind the non-diffraction range. In the link budget the antennas are progressively spaced.*

This geometrical explanation can be generalized to the previous links examined with the proper dimensions of transmitting and receiving antennas.

Finally, it is worth noticing that when Bessel Beam Launchers are used both in transmission and reception the total received power is composed by the contribution not only of the main lobe of Bessel's radiation, but also of the secondary ones.

The efficiency of the link can be evaluated as the ratio between the power accepted by the receiving antenna and the power radiated by the transmitting antenna, as showed in Figure 4.1.6: $\eta_{RF-RF} = P_{RX}/P_{TX}$.

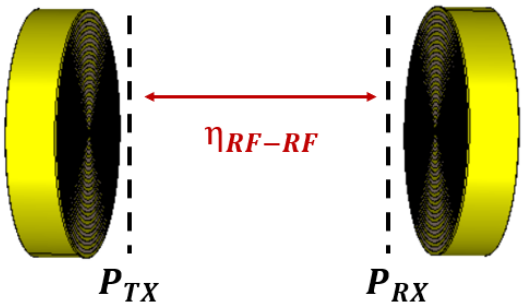

***Figure 4.1.6**: Efficiency of the link considered as the ratio of power entering the receiving antenna and power exiting the transmitting antenna.*

In Figure 4.1.7 the efficiencies for the different links under examination are reported. As predictable, the link with the Bessel Beam launcher of 3 cm radius shows the most performing link efficiency starting from 80% at 10 mm and reaching 15% at 40mm. The mixed link efficiently is not evaluated but straightforwardly will be a compromise among the two of Figure 4.1.7.

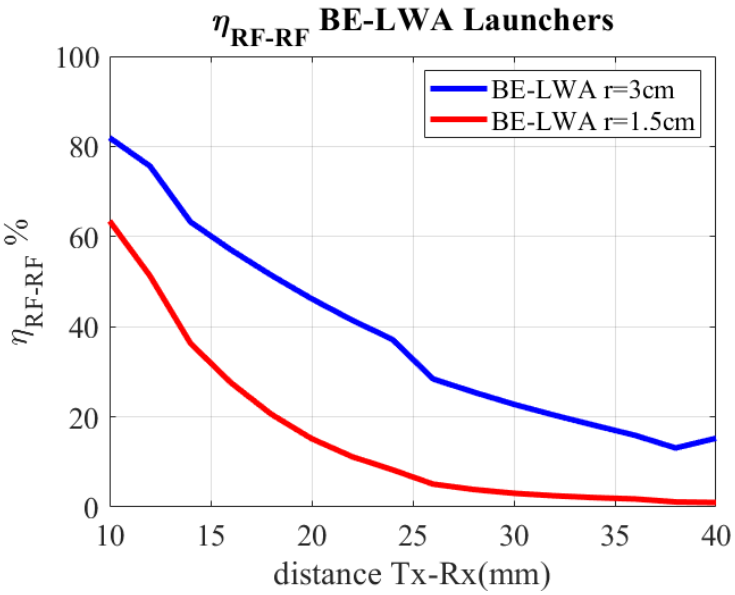

***Figure 4.1.7**: Efficiency of the link evaluated as ratio of power received and power transmitted for the different BE-LWAs.*

The power given in input is 0.5W, but it is not entirely accepted by the antenna.

If the efficiency is evaluated by considering the actual power that is accepted by the antenna as $P_{IN} = 0.5 * (1 - |S_{11}|^2)$, the expression becomes $\eta = P_{RX}/P_{IN}$. This led to a is a degradation of performances reported in Figure 4.1.8.

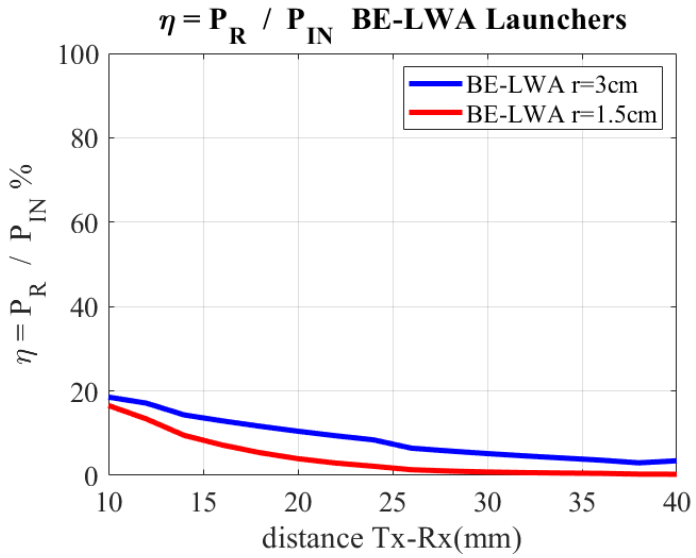

***Figure 4.1.8**: Efficiency of BE-LWAs evaluated as ratio of power received and power accepted by the antenna.*

After the evaluation of link budgets that employ only Bessel Beam Launchers in both transmission and reception, further research on the receiver configuration is performed. For the transmission side, Bessel Beam Launchers shows noticeable properties: they are appealing for focusing application in the radiative near field where the objective is to radiate most of the power in a limited angular section. Thanks to their diffraction-free nature the focusing results to be effective for a large distance corresponding to the non-diffraction range, showing better focusing capabilities with respect to other beam-like solutions. At the same time their use as receiver may not be the best solution when talking about wearable and implantable devices: their rigid structure due to the metallic nature of the waveguide does not allow to think of bendable solutions or something that could adapt its shape better to human tissues. Besides this, being the non-diffractive range directly proportional to the radius of the antenna it is not possible to have a further miniaturization by keeping the same frequency of operation, unless a reduction of the application range is accepted.

A further investigation is performed to search for a better solution in reception in terms of miniaturization, at the expense of reducing the power transfer efficiency. In transmission the best solution among the one presented in this chapter is considered, that is the Bessel Beam Launcher of radius $\rho_{ap} = 3cm$. The main goal for the receiving

antenna is to collect at least the power coming from the main lobe of the Bessel distribution. Therefore, it is accepted to lose the power coming from the secondary lobes in favour of reduced dimension of the receiving antennas.

Therefore, the receiver must full-fill the following requirements:

- It must have dimensions comparable to the area of the main beam coming from the Bessel Beam Launcher, which has a radius of approximately 5mm.
- It must resonate at the same operating frequency of the Bessel Beam Launcher (approximately 31.67 GHz)
- It is needed a strong magnetic field concentrated in the centre of the antenna to increase the interaction with the transmitter.

The most intuitive kind of antenna that shows a strong magnetic field near the antenna and in its central region would be an electrically small loop (with a perimeter $2\pi R < \lambda$). For instance, it is considered a simple configuration such as a square half-wave loop with perimeter equal to $\lambda/2$, as presented in Figure 4.1.9:

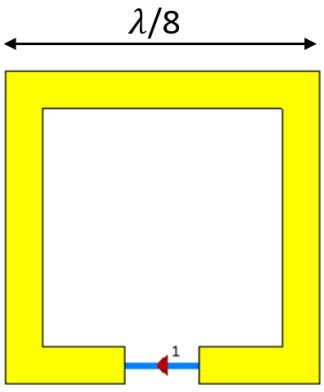

***Figure 4.1.9**: Square half wave loop.*

It can be observed in Fig. 4.1.10 that, since its dimension, the current flows always in the same direction along the loop without experiencing change of phase, generating a strong and uniform magnetic field in the central area.

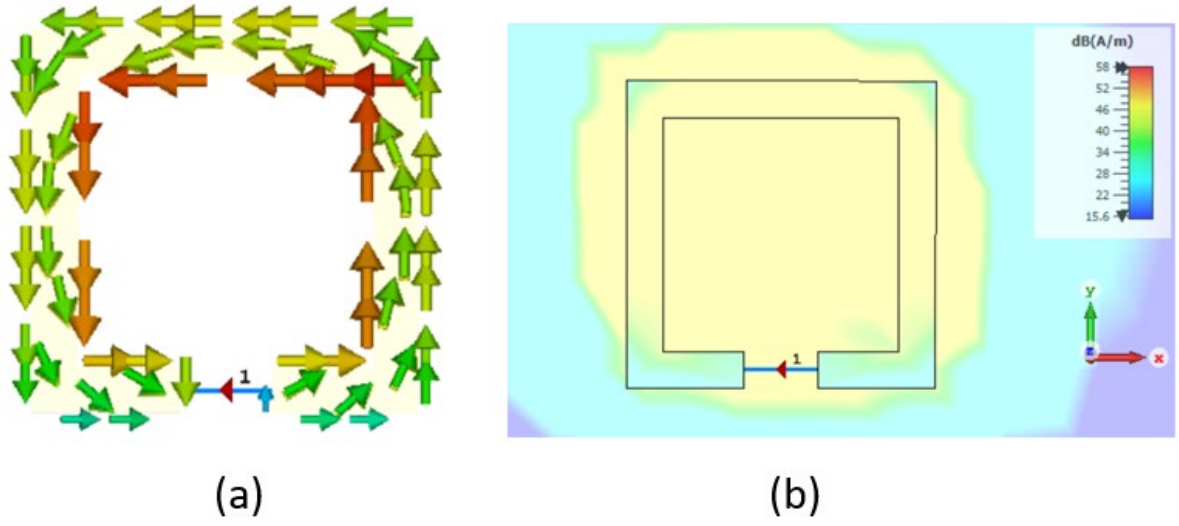

***Figure 4.1.10**: Surface current flowing in a single direction along the loop (a). Magnetic field over the xy-plane showing a large intensity in the centre of the loop (b).*

This is the desired principle of operation for our receiving antenna. However, when the operating frequency is set to 30 GHz, the side of an electrically small antenna becomes extremely small, approximately 1mm, too small compared to the dimension of the main beam from the Bessel distribution and difficult to realize.

Therefore, based on this requirement given by the dimension of the main Bessel Beam, a square loop antenna with 8 mm side is proposed and analysed as receiver apparatus, as presented in Figure 4.1.11 :

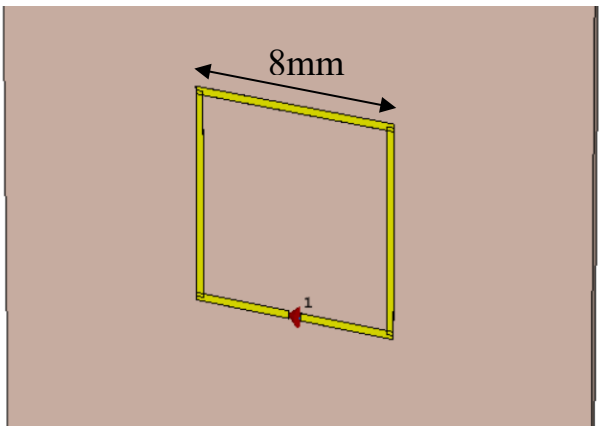

***Figure 4.1.11**: Square loop of side 8mm working at 31.67 GHz.*

The square loop has a thickness of 0.0175 mm with a line width of 0.3mm. It is placed over a Roger RO3003 substrate with 0.256 mm thickness and $\varepsilon_r = 3$. The. The simulations are performed with CST Microwave Studio 2019 and results are presented and discussed. The full-wave EM simulation shows that, with this dimension, the loop antenna is working at the fourth resonance since the perimeter of the loop is approximately 4λ , as shown in Figures 4.1.12

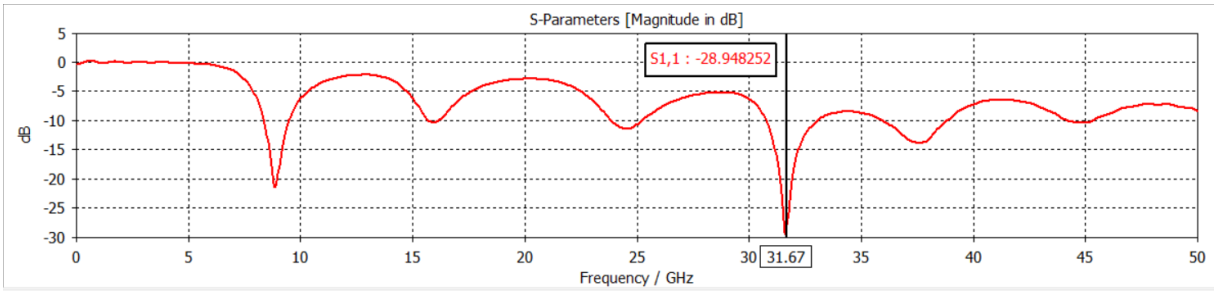

***Figure 4.1.12**: Square loop operating at the fourth resonance. Simulation performed on CST Microwave Studio 2019.*

The surface current experiences a phase inversion after a path of length about $\lambda/2$, as observed in Figure 4.1.13, giving rise to eight points where the current is null. Due to the phase inversions at opposite sides of the square loop, the magnetic fields H_z (along z-direction) interfere destructively. The result is a very weak magnetic field level in the central region, as shown in Figure 4.1.14. For this reason, it is impossible for an electrically large loop of dimensions comparable to the operating wavelength (or greater than) to generate a strong magnetic field in the central area.

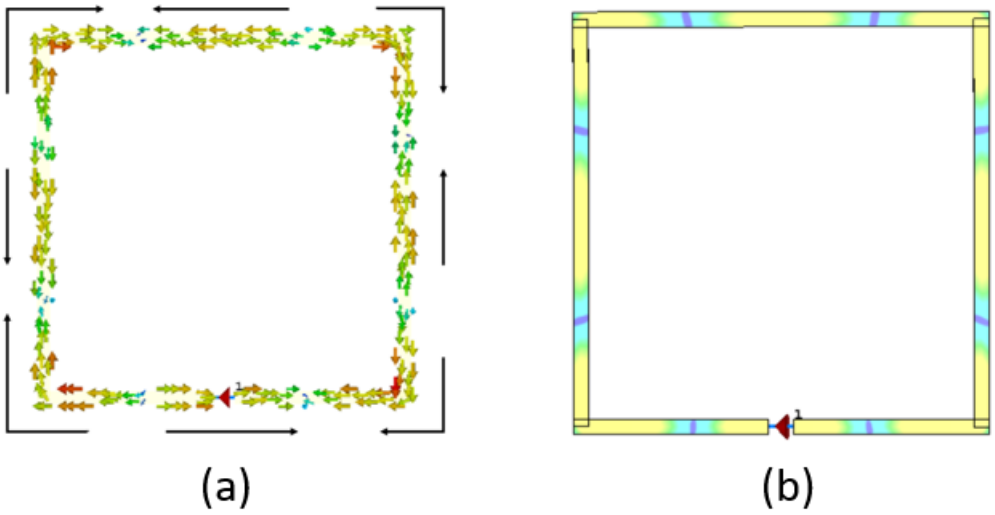

***Figure 4.1.13**: Flow of the current along the square loop (a) and positions of the zeros of the current (b).*

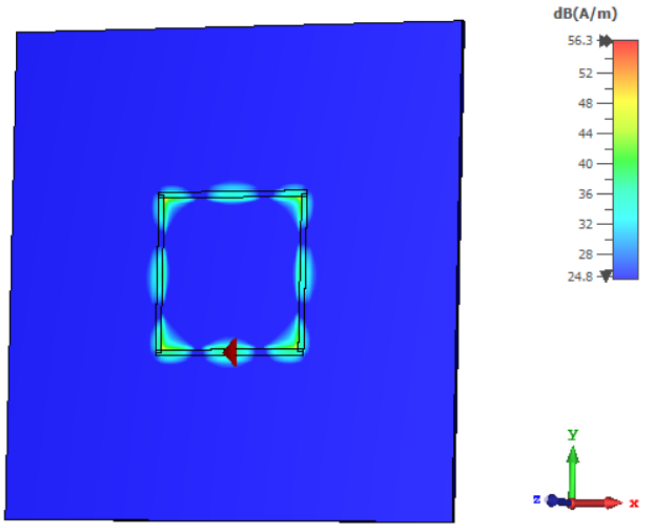

***Figure 4.1.14**: Magnetic field intensity over the xy plane. At the centre the intensity is very low.*

In order to countermeasure this effect and make the loop able to sustain acceptable magnetic field level in central region, defined also ‘interrogation zone’ for near field RFID applications [23], the goal is to provide a current which flows in the same direction along all the loop, in order to ensure the same behaviour of an electrically small loop. As in [23], in literature different works are present regarding the modification of electrically large loop to achieve a uniform magnetic field while keeping large area, especially in near-field RFID (radio frequency identification)

application at ultra-high frequencies UHF (860-960 MHz) and at microwave (2.4 GHz and 5.8 GHz) [24]. All of these are based on the common goal of implementing techniques to maintain constant the direction of the flowing surface current along the loop. Among all, it is deeply analysed the method reported in [23], where different phase shifters are used to compensate for the phase inversion in order to have the surface current along the loop to flow in the same direction, therefore generating a uniform magnetic field in the interrogation zone. The length of a single phase shifters corresponds to the distance between two zeros of the surface current, that is approximately $\lambda/2$, such that the phase inversion is ensured along the shifters and in the successive portion of loop the current flows in the desired direction. Of course, the introduction of the phase shifters enlarges the total electrical length of the loop, and a delicate tuning of the shifters' length is required, especially considering the operating mm-Wave frequencies involved.

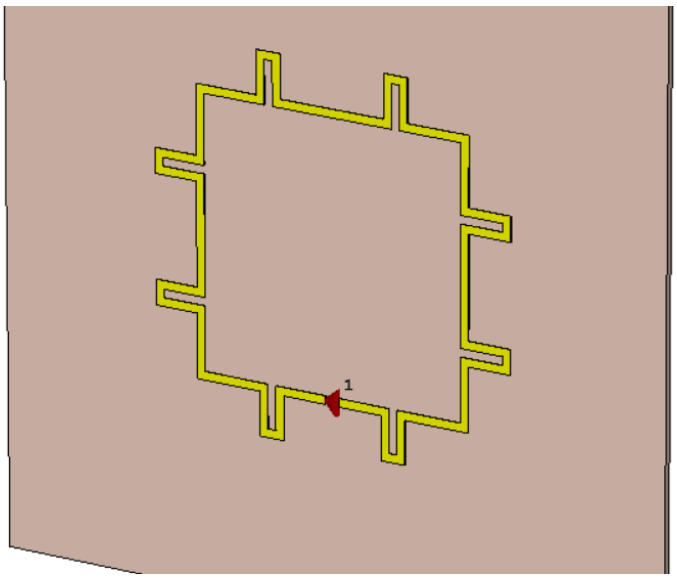

Figure 4.1.15*: Square loop with the stub phase shifters.*

Starting from the electrically large loop presented previously in this chapter, 8 phase shifters , as presented in Figure 4.1.15, in correspondence of the nulls of the current are

inserted for obtaining the desired effect. The design phase shifters parameters are illustrated in Figure 4.1.16.

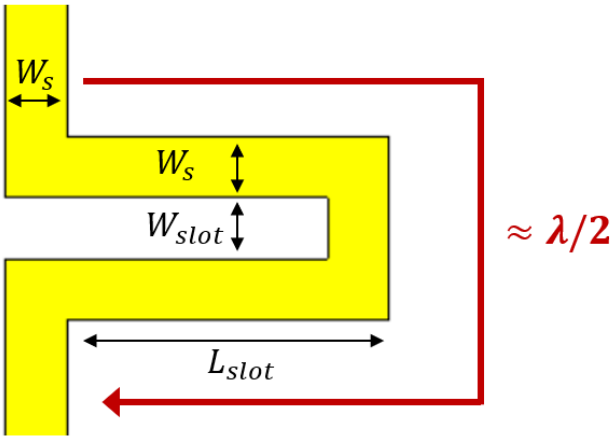

***Figure 4.1.16**: Design parameters of each stub phase shifter.*

The final dimensions of the phase shifters ensuring the best behaviour in terms of resonance and current flow are listed in Table 4.

Parameter	Value
L_{slot}	$1.57\ mm$
W_{slot}	$0.3\ mm$
W_s	$0.3\ mm$

***Table 4**: Parameters values obtained from full-wave simulation.*

As soon as the phase shifters are introduced, the electrical length of the antenna is increased from 4λ to 8λ, as shown in Figure 4.1.17.

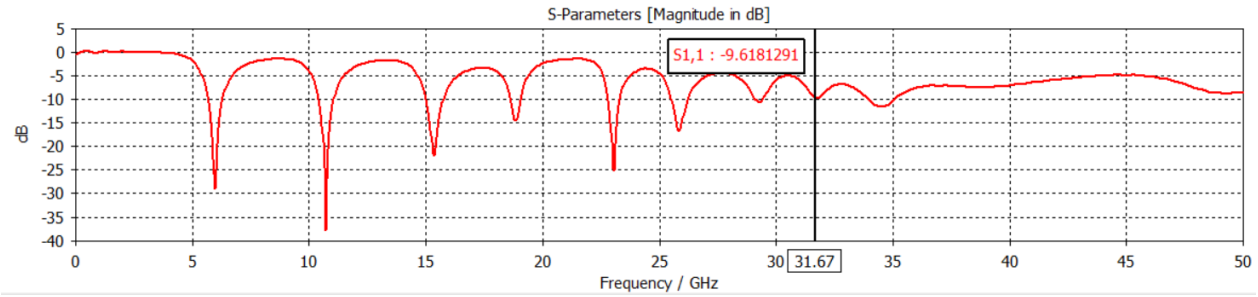

***Figure 4.1.17**: Frequency of operation at 8th resonance after the introduction of the slots.*

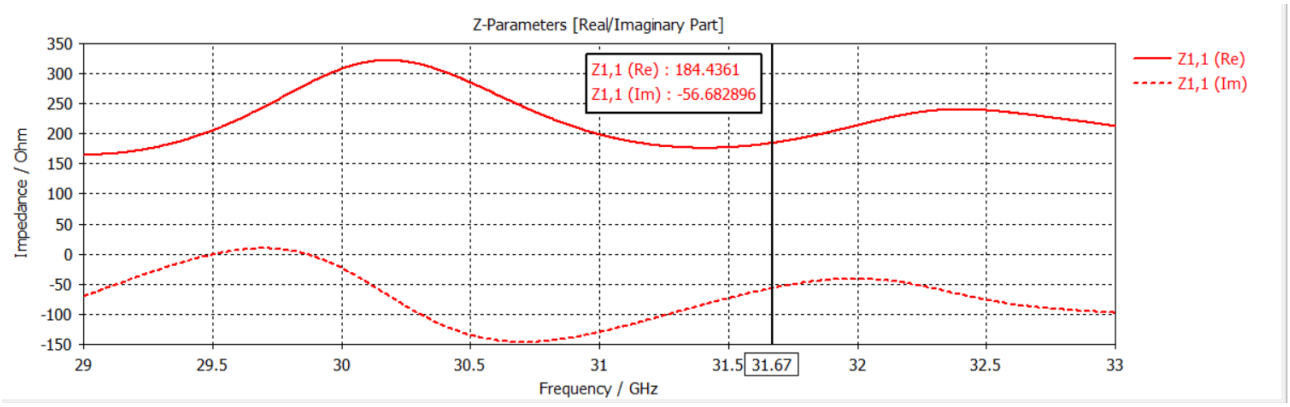

***Figure 4.1.18**: Impedance of the square loop at the operating frequency of 31.67 GHz.*

The antenna shows an $S_{11} = -9\ dB$ at the frequency of interest and an impedance of $Z = 184 - j56$, reported in Figure 4.1.18, therefore a matching network is necessary when a rectifier circuit will be considered. It must be stated that the position of the phase shifters has fundamental importance during the tuning phase, as can be observed in Figure 4.1.19. In fact, by chancing it, the intensity of the surface current changes drastically and rapidly moving far away from the best solution. After the tuning of all the design parameters a correct flowing and a uniform intensity of the surface current is finally obtained.

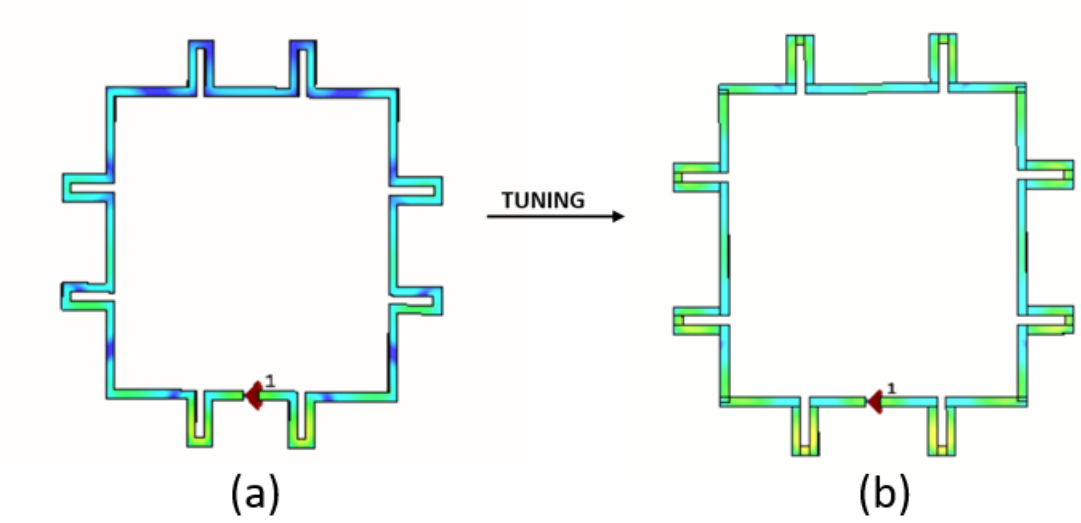

***Figure 4.1.19**: Current intensity (dB) along the loop before (a) and after (b) the tuning.*

As can be observed by the Figure 4.1.20, the collocation of the correct phase shifters has replicated the effect of electrically small loop: the surface current flows always in the same direction along the loop and in the interrogation zone the magnetic field results acceptable in terms of intensity. The asymmetries in its behaviour (present mainly in the lower part of the antenna) are imputable to the presence of the port.

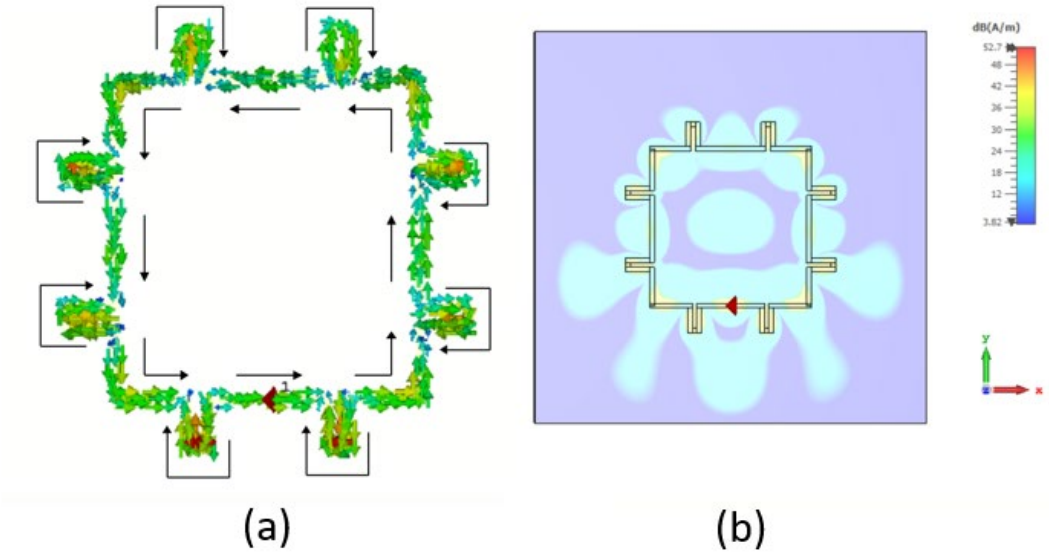

***Figure 4.1.20**: Current flow after the tuning of the phase shifters (a). Magnetic field intensity increased in the centre of the loop (b).*

For the sake of reliability, it is also verified that this antenna at the first resonance located at 6 GHz behaves as a full-wave loop. Finally, since at high frequencies of operation the steep edges may be a source of issues because of their radiation properties, it has been introduced a slight bending of 0.1 mm, that does not significantly affect the behaviour of the antenna, as showed in Figure 4.1.21.

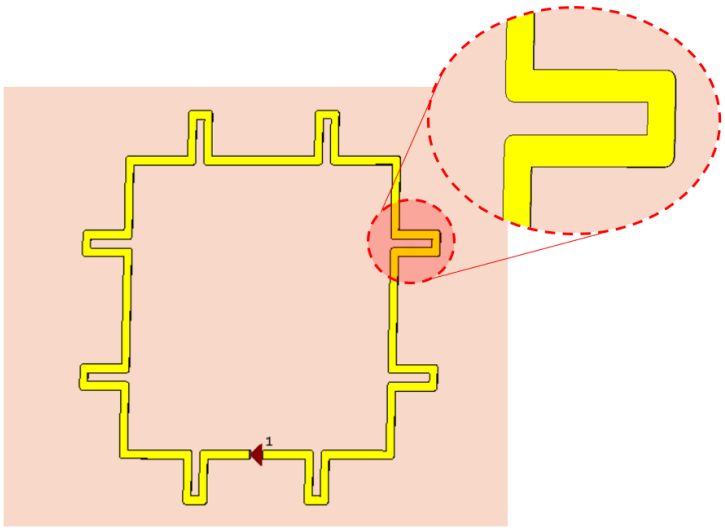

***Figure 4.1.21**: Square loop with blended edges.*

The fields emitted by this antenna are reported in Figure 4.1.22 and 4.1.23 and result to be similar enough to the fields radiated by the Bessel Beam Launcher. In particular, the z-component of the magnetic field H_z shows the desired maximum exactly in the centre of the antenna. The radius of the central beam generated by the square loop antenna is of 5 mm, big enough to capture at least the main lobe coming from the Bessel Beam Launcher.

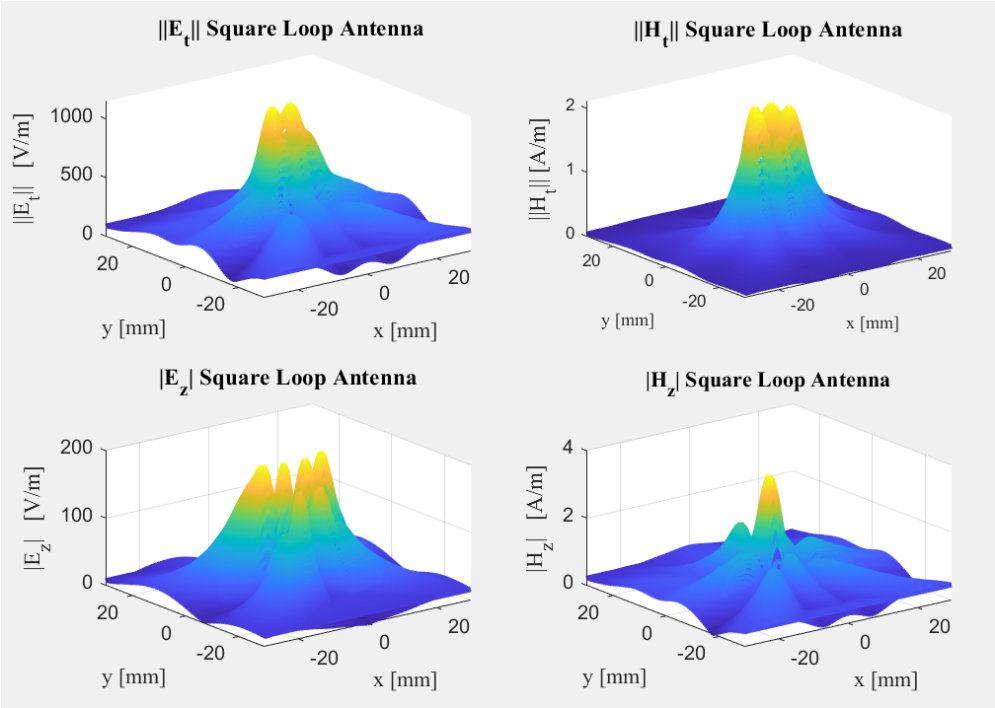

***Figure 4.1.22**: Fields of the square loop antenna at an arbitrary distance of 5mm.*

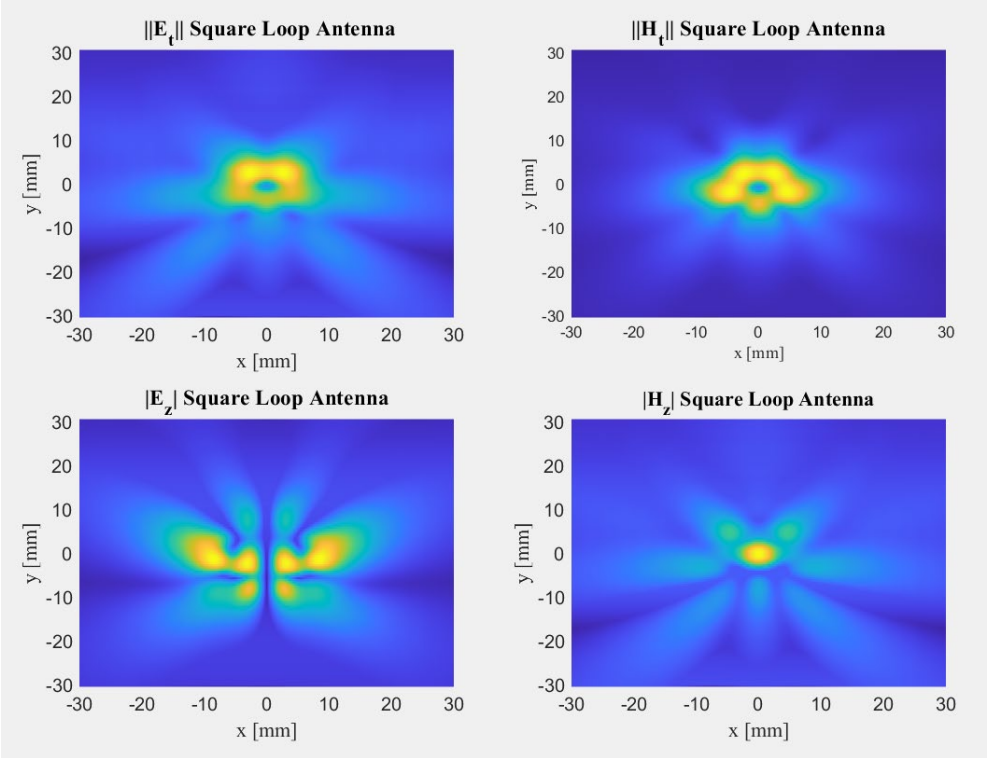

***Figure 4.1.23**: Fields of the square loop antenna from a top view.*

The z-component of the magnetic field, reported in Figure 4.1.24, shows a relevant intensity in the interrogation zone for a range of distances up to 5mm.

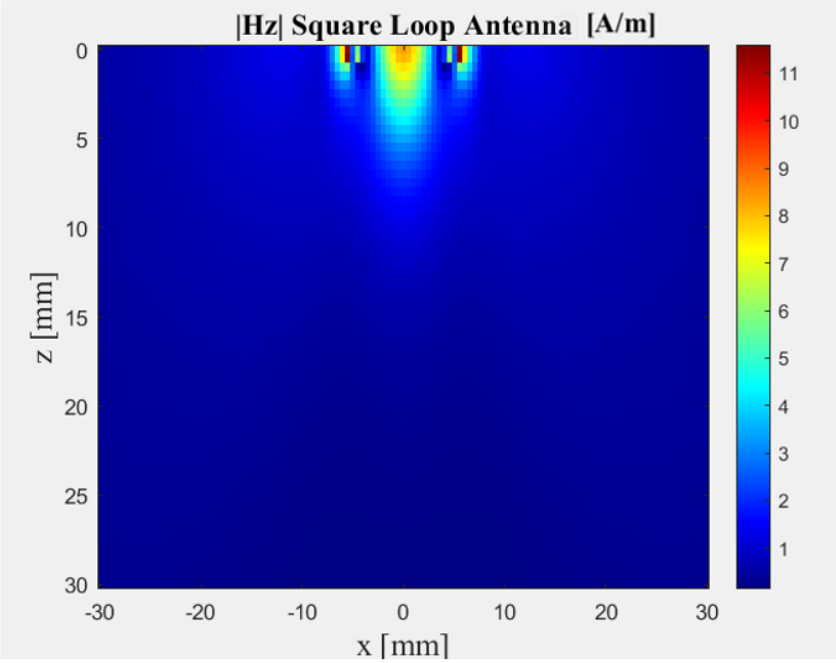

***Figure 4.1.24**: z-component of the magnetic field emitted by the square loop with phase shifters over the xz-plane.*

To evaluate the performance of the square loop in reception the link budget is computed considering as transmitting antenna the Bessel Beam Launcher of radius 3cm.

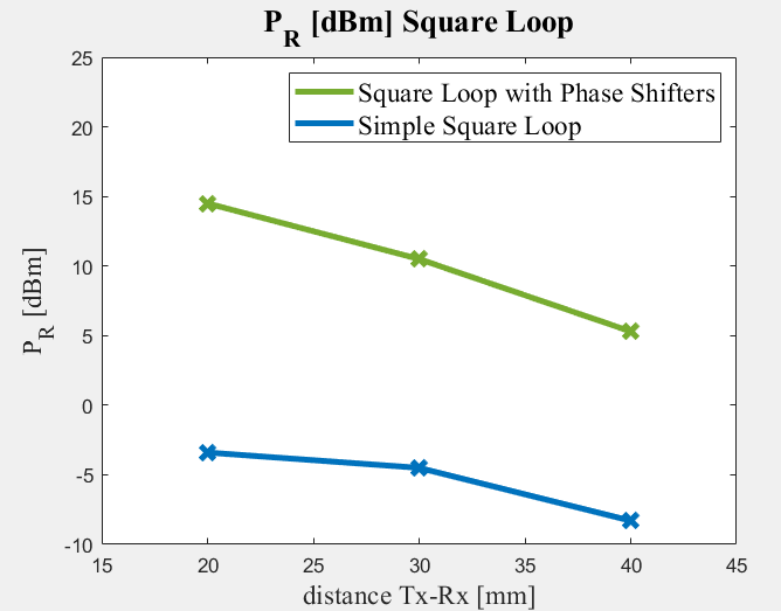

***Figure 4.1.25**: Comparison of Link Budget using in transmission the BE-LWA of r=3cm and in reception the square loop before and after the insertion of phase shifters.*

The link budget is evaluated by using in reception the simple square loop and the square loop after the insertion of phase shifters: from Fig. 4.1.25 can be observed an increase of almost 20 dBm in the received power by using phase shifter to generate a strong magnetic field in the interrogation zone. The behaviour of the square loop in reception is comparable in terms of received power with the one of the smaller Bessel Beam Launcher, as inferred from the results of Figure 4.1.26. This validates the use of the square loop with phase shifters as receiving antenna, since it offers a higher level of miniaturization and an easier fabrication.

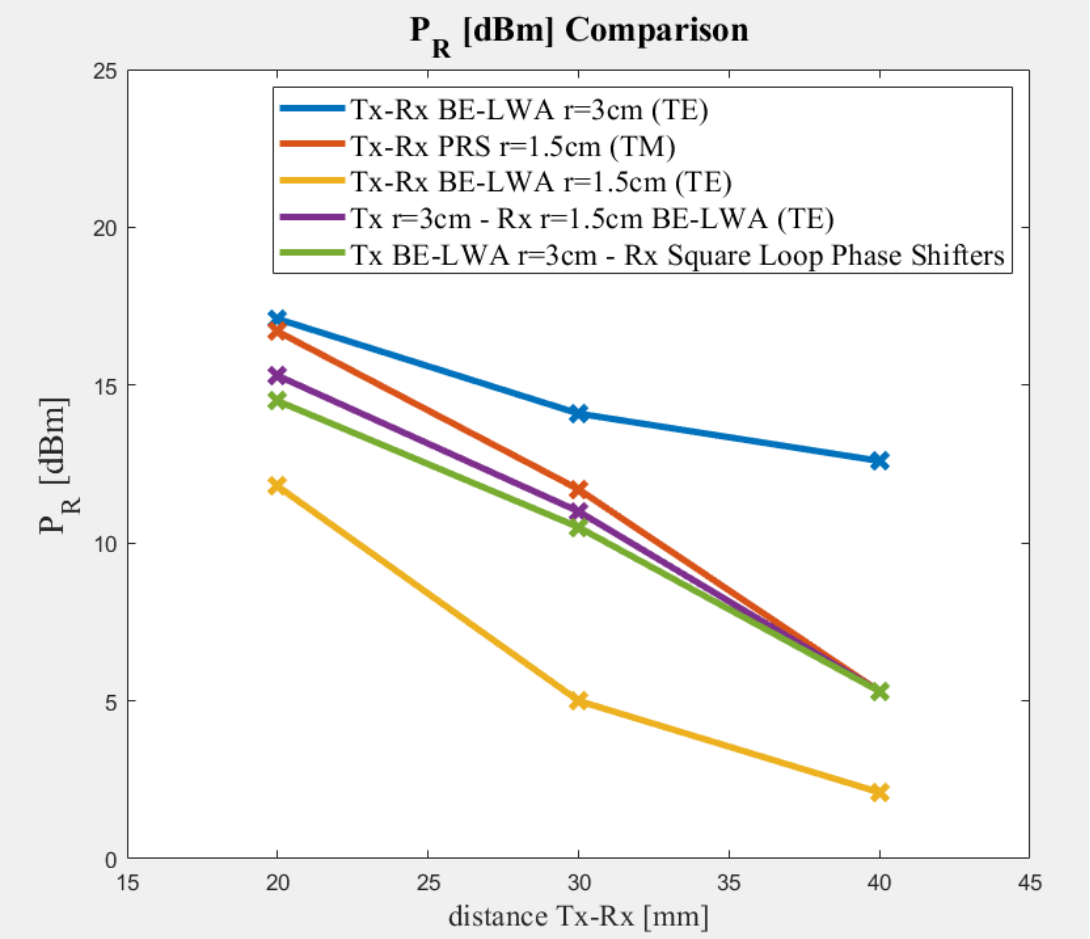

***Figure 4.1.26**: Received power comparison for all the configurations of link considered.*

These results are obtained under a conjugate matching condition and with an input power to the transmitting antenna of 27 dBm.

Finally, through full-wave EM simulator, the square loop antenna is simulated when placed over biological tissues to evaluate its reliability for wearable applications. In particular behind the antenna are added:

- A layer of skin, represented with a substrate of $\varepsilon_r = 14.8$ and $\tan\delta = 1.0807$ at 31.67 GHz, with a thickness of 2 mm.
- A layer of fat, represented with a substrate of $\varepsilon_r = 3.6$ and $\tan\delta = 0.2956$ at 31.67 GHz, with a thickness of 8 mm.
- A layer of muscle, represented with a substrate of $\varepsilon_r = 22.2$ and $\tan\delta = 0.946$ at 31.67 GHz, with a thickness of 10 mm.

The antenna results to be extremely sensitive to biological tissues, showing a shift of the resonance point that consequently has an impact on the current flow. The maximum intensity of magnetic field in the interrogation zone is lost, as well as the correct compensation of phase implemented through phase shifters, as shown in Figure 4.1.27.

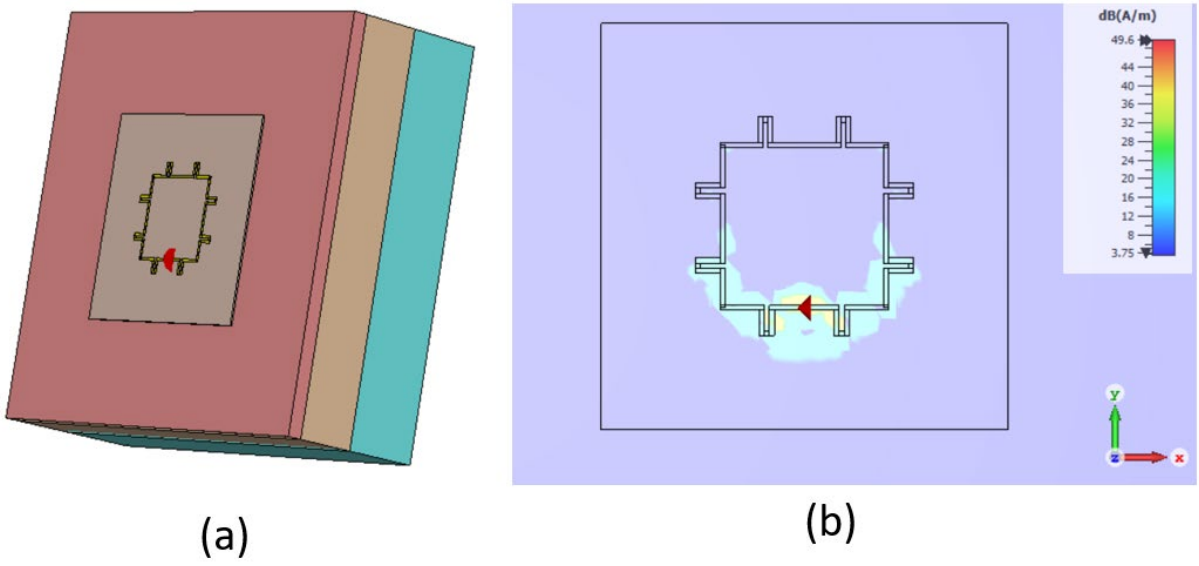

***Figure 4.1.27**: Square loop antenna placed on biological tissues (a). The magnetic field intensity over the interrogation zone becomes very low (b).*

For the sake of evaluating the sensitivity of the square loop antenna, the Rogers RO3003 substrate thickness is increased from 0.256 mm to 1mm. A thicker substrate could reduce the extreme sensitivity of the antenna to human tissues. However, as observed in Fig. 4.1.28, even in this case there is an impact over the magnetic field distribution.

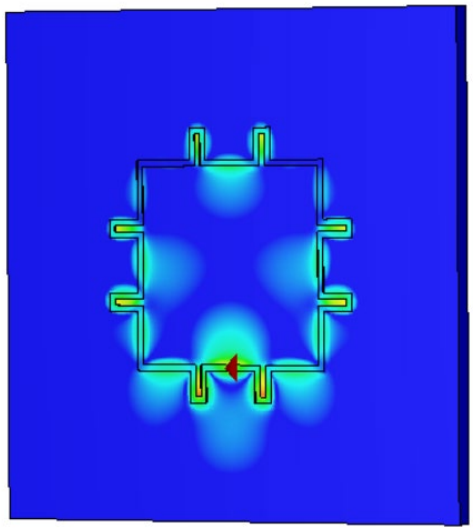

Figure 4.1.28*: Magnetic field intensity reduced in the interrogation zone due to the increase to h=1mm of the substrate thickness.*

4.2 Rectification

After the quantification of the received power for the different configurations of the link, a proper rectifier must be designed and optimized. The rectifier is based on nonlinear components therefore, it is designed by means of harmonic balance simulations. The receiving antenna, represented with its Thevenin equivalent circuit, is followed by a linear subnetwork called matching network to perform impedance matching between the antenna and the rectifier, in order to maximize the power transfer flowing into the rectifier. The whole circuitry is implemented on a Rogers RO3003 substrate with $\varepsilon_r = 3$ and $\tan\delta = 0.001$ at 10 GHz with a thickness of 0.256mm.

It is well-known that performing rectification at mm-Waves is not trivial: at high frequencies, in fact, the package parasitic effects become very relevant. A type of diode performing efficiently at mm-Waves is the Schottky diode, extensively used in WPT

applications. Schottky diodes are formed by the junction of a semiconductor with a metal and compared to the classical p-n diodes, they offer faster switching time and lower voltage drops. The lower threshold voltage allows to reduce the dissipated power and keep higher levels of current with respect to a p-n diode with the same junction area. The diode used is a GaAs (gallium arsenide) beam led Schottky diode (Macom MA4E2038), that is chosen for its remarkable properties:

- Low series resistance R_S.
- Low junction capacitance C_j.
- High Cut-Off frequency f_C.

Gallium arsenide offers a high carrier mobility, resulting in a low series resistance that minimizes not only the noise figure and the conversion losses, but also the switching time $\tau = R_S C_j$. The minimized junction capacitance allows to have a cut-off frequency $f_C = 1/R_j C_j$, making these diodes efficient for rectification at mm-Waves. In the circuital software, the Advanced Design System, itis possible to represent the diode through its Spice parameters, that are found in its datasheet and reported in the table of Table 5.

Parameter	Units	Macom MA4E2038
B_V	V	7
C_{j0}	pF	0.02
E_G	eV	1.43
I_{BV}	mA	0.01
I_S	fA	10
R_S	Ω	9
N		1
T_t	ns	0.01
V_j	V	0.7
M		0.26
X_{ti}		2

***Table 5**: Spice parameters of the Macom MA4E2038.*

Figure 4.2.1 shows the Macom MA4E2038 Schottky diode model with the corresponding parasitic components. The parasitic effects are related to the package, the internal junction surface and to the leads. Parasitic components are frequency dependant and become more and more relevant for increasing frequencies.

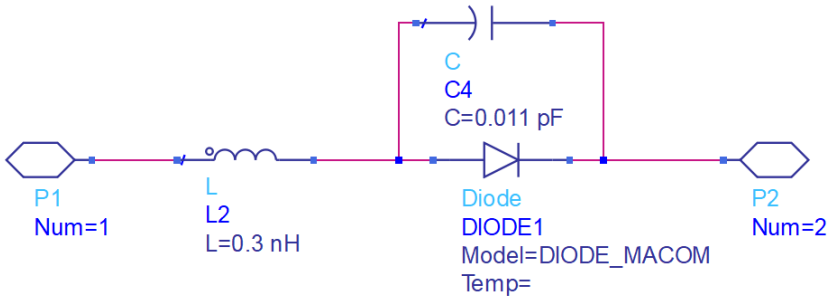

***Figure 4.2.1**: Macom MA4E2038 diode model with parasitic components.*

The rectifying circuit must be optimized according to the input power range, that in the presented case will be referred as the power received by the antenna for the different operating distances. Assuming that the 3-cm Bessel Beam launcher is always used as transmitter, due to its best performance, the range of received power for the two tested receivers is almost the same:

- When the 1.5-cm BB Launcher is used as receiver, received power goes from 17,4 to 5,3 dBm in the range of 10-40mm.
- When the square loop antenna is used as receiver, the received power goes from 15 to 5,3 dBm in the range of 10-40mm.

The power received from the antenna are given as input to the rectifier.

All the parameters of the matching network and of the rectifier are optimized with the goal of maximizing the conversion efficiency $\eta_{RF-to-DC}$, defined as the ratio between the DC power delivered to the load and the power available at the receiving antenna. The latter is intended as the power incident to the antenna, represent in ADS Keysight with its Norton equivalent circuit.

The first rectifier described considers the Bessel Beam Launcher of r=1.5cm as receiving antenna. In order to include the proper range of powers, the harmonic balance simulation is performed for an input power sweeping from 4 dBm to 18 dBm.

The matching network between the antenna and the rectifier is composed of two microstrip line and one microstrip open-circuited stub combined in the typical T-shape, as shown in Figure 4.2.2. For the rectification a full-wave rectifier is used, implying the use of two Schottky diodes.

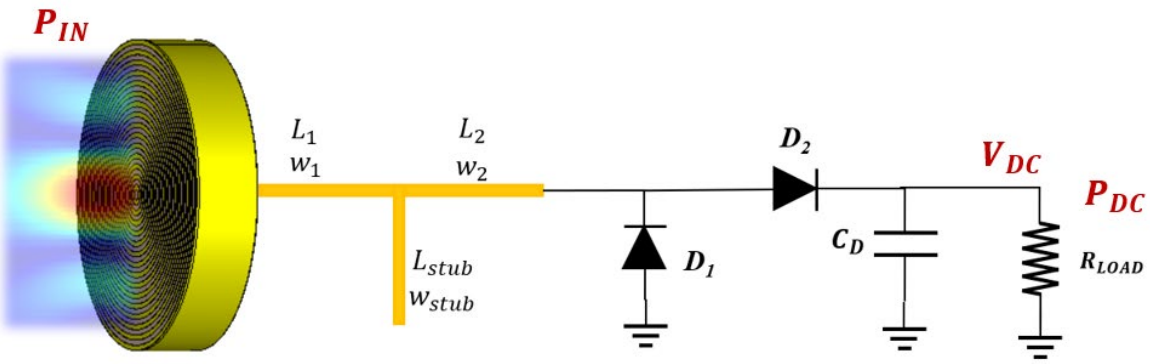

***Figure 4.2.2**: BB Launcher of radius r=1.5cm as receiving antenna with matching network and rectifying circuit.*

The optimized values that maximize the power conversion efficiency are reported in Table 6.

Component	Value
L_1	1 mm
w_1	1 mm
L_2	3.8 mm
w_2	1.5 mm

Component	Value
L_{stub}	8 mm
w_{stub}	1.6 mm
C_D	100 pF
R_{Load}	400 Ω

***Table 6**: Optimized values for the different components.*

The rectification efficiency is defined as $\eta_{RF-to-DC} = \frac{P_{DC}}{P_{IN}}$, with powers defined in Figure 4.2.2. Observing the rectification efficiency in Figure 4.2.3: at 10 mm distance between transmitter and receiver the efficiency is of the order of 30%, however it is not safe to work at such high level of received power because, as it can be seen from the graph, we would operate close to the diode breakdown voltage. In this case, a slightly lower level of input power should be transmitted. Spacing the transmitter and the receiver of 20 mm the efficiency is kept almost at 30%, decreasing to 25% and 15% for 30 and 40 mm distance, respectively. In Figure 4.2.3, also the DC- output voltage is reported for different input power levels.

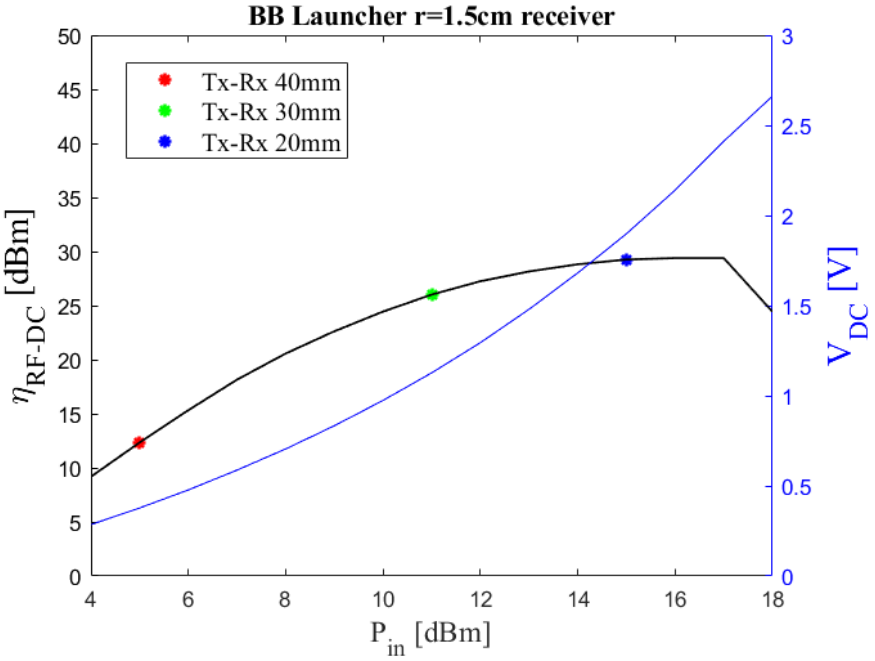

***Figure 4.2.3**: RF-DC power conversion efficiency and DC output voltage for different values of input power.*

In terms of rectified DC-output power, the circuit manages to provide approximately 1 mW for an input power corresponding to a 30% RF-to-DC efficiency, as shown in Figure 4.2.4.

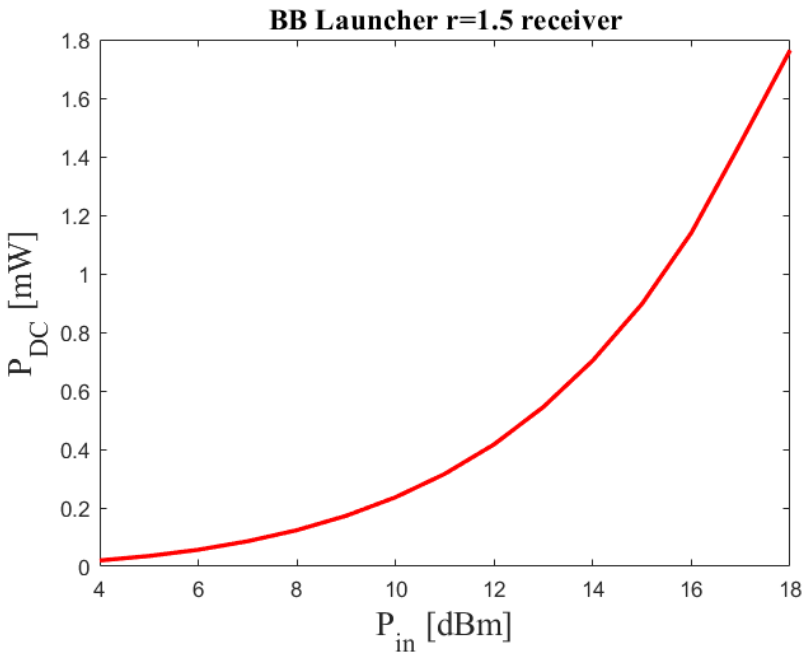

***Figure 4.2.4**: DC output power in mW for different values of input power.*

The second rectification circuit uses the 8-mm side square loop antenna as receiver. The matching network is composed of a series capacitance, one microstrip open-circuited stub followed by a microstrip line, as showed in Figure 4.2.5. Also in this case, a full-wave rectifier is implemented.

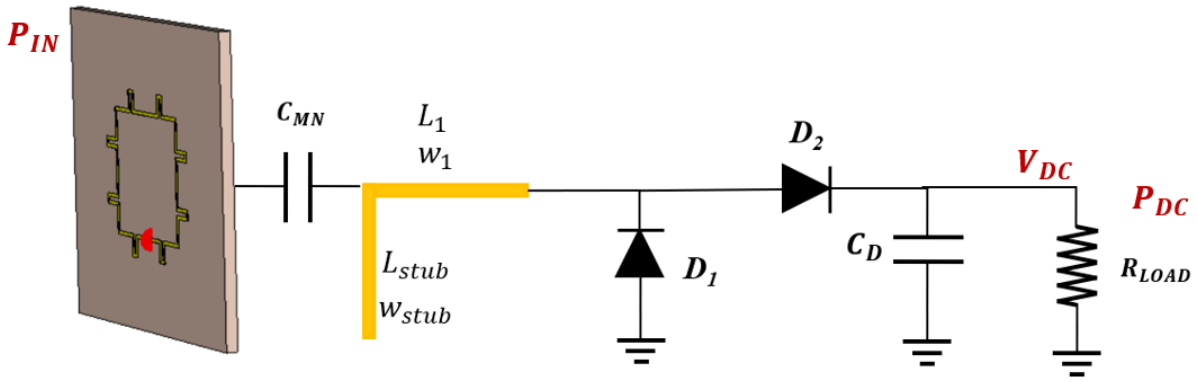

***Figure 4.2.5**: Square loop antenna in reception followed by the matching network and the rectifying circuit.*

Being the system of transmitting and receiving antenna a linear system, the input power can be slightly reduced in order to allow a receiver power range that falls within the diode operating power range, avoiding to work close to its breakdown voltage.

The evaluation of the rectifier power conversion efficiency is performed by considering an input power sweeping from -2 to 11 dBm.

A new optimization of the circuit parameters is performed with the new values reported in Table 7.

Component	Value
L_{stub}	8.5 mm
w_{stub}	1.9 mm
C_D	100 pF
R_{Load}	2300 Ω

Component	Value
C_{MN}	840 pF
L_1	4 mm
w_1	2 mm

***Table 7**: Optimized values of the matching network and rectifying circuit.*

The power conversion efficiency is shown in Figure 4.2.6 together with the DC - output voltage: with the square loop as receiving antenna, the efficiency is 40% with 20 mm distance between transmitter and received, lowering to 27% and 15% for 30 and 40 mm distances respectively.

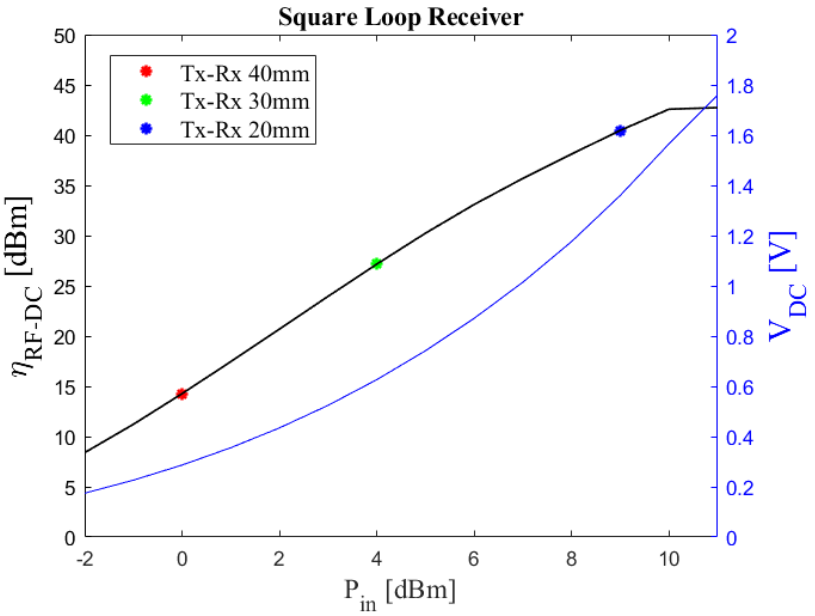

***Figure 4.2.6**: Power conversion efficiency and DC output voltage for different input powers.*

This rectifier is able to deliver 0.5 mW of rectified DC-output power for an input power corresponding to a 40% efficiency, as shown in Figure 4.2.7.

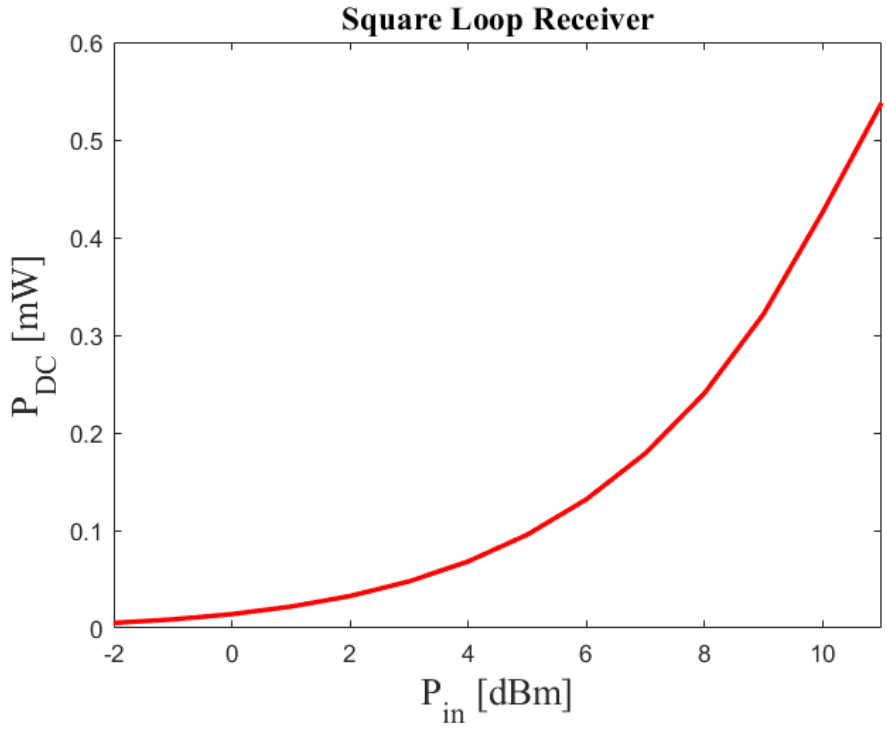

***Figure 4.2.7**: DC output power [mW] for different input power levels.*

Chapter 5: Conclusions and future prospects

The thesis project has described the implementation of a Wireless Power Transfer link working at mm-Waves. The radiative near-field is investigated exploiting the so-called Bessel Beam Launchers. These antennas are chosen for their remarkable properties such as focusing and self-healing, as well as their capability to generate a non-diffractive beam following a zeroth-order Bessel function. A Bull-Eye Leaky Wave Antenna, realized with a FPC-cavity structure with an annular metal strip grating surface on top, is proposed. A great focusing capability is reported, with a main beam centred in a region of radius 5 mm. The antenna is designed to work at 30 GHz, with an initial radius of 1.5cm, allowing for non-diffractive range of 20 mm. This nondiffractive range is then incremented to 40 mm by roughly doubling the radius of the antenna to 3 cm. The two BB Launcher are analysed under a power transport point of view, finding out that the BB with radius 1.5 cm transports more power in its main

lobe ($\approx 80\%$) at the expense of lower operating distances. The 3-cm BB Launcher keeps its directivity for longer distances, although the power contained in its main lobe is lower ($\approx 50\%$).

In the perspective of using this kind of antennas for wearable or implantable applications, two miniaturized receivers are considered. First, the BB Launcher of radius 1.5 cm. Subsequently, a further research regarding the receiving side is performed. A square loop antenna of side 8 mm, modified with some phase shifters, is found to provide satisfactory results. The two receivers are finally attached to a matching network and to a rectifier, achieving a 30% rectification efficiency, for the 1.5-cm BB launcher, and 40% efficiency when the square is considered. Although designing a rectifier working efficiently at mm-waves is indeed a challenge, the obtained results are promising. Regarding future perspectives, prototypes of the designed Bessel Beam launchers could be realized to compare measured and simulated results. Also, for an accurate performance in the warble context, i the effect of biological tissues must be dimensioned and quantified. The Bessel Beam Launcher, thanks to the metallic rim is expected to be less sensitive to biological tissues, whereas the square loop antenna, that is not equipped with a ground plane, is found to be deeply impacted when substrates simulating human tissues are added. In the next future, improvements on the antenna design can be investigated and performed in order to make this design as less sensitive as possible to the presence of biological tissues, leading to a thorough system that combines miniaturization and performance in the most efficient way.

Bibliography

[1] A. Costanzo and D. Masotti, "Energizing 5G: Near- and Far-Field Wireless Energy and Data Transfer as an Enabling Technology for the 5G IoT," in *IEEE Microwave Magazine*, vol. 18, no. 3, pp. 125-136, May 2017, doi: 10.1109/MMM.2017.2664001.

[2] M. Wagih, A. S. Weddell and S. Beeby, "Millimeter-Wave Power Harvesting: A Review," in *IEEE Open Journal of Antennas and Propagation*, vol. 1, pp. 560-578, 2020, doi: 10.1109/OJAP.2020.3028220.

[3] M. Nariman, F. Shirinfar, A. Papió Toda, S. Pamarti, A. Rofougaran and F. De Flaviis, "A Compact 60-GHz Wireless Power Transfer System," in *IEEE Transactions on Microwave Theory and Techniques*, vol. 64, no. 8, pp. 2664-2677, Aug. 2016, doi: 10.1109/TMTT.2016.2582168.

[4] J. Garnica, R. A. Chinga and J. Lin, "Wireless Power Transmission: From Far Field to Near Field," in *Proceedings of the IEEE*, vol. 101, no. 6, pp. 1321-1331, June 2013, doi: 10.1109/JPROC.2013.2251411.

[5] D. R. Smith, V. R. Gowda, O. Yurduseven, S. Larouche, G. Lipworth, Y. Urzhumov, and M. S. Reynolds, “An analysis of beamed wireless power transfer in the Fresnel zone using a dynamic, metasurface aperture,” J. Appl. Phys., vol. 121, no. 1, p. 014901, 2017

[6] J. D. Heebl, M. Ettorre, and A. Grbic, “Wireless links in the radiative near field via Bessel beams,” Phys. Rev. Appl., vol. 6, no. 3, p. 034018, 2016.

[7] M. Ettorre and A. Grbic, “Generation of propagating Bessel beams using leaky-wave modes,” IEEE Trans. Antennas Propag., vol. 60, no. 8, pp. 3605–3613, 2012.

[8] W. Fuscaldo, G. Valerio, A. Galli, R. Sauleau, A. Grbic, and M. Ettorre, “Higher-order leaky-mode Bessel-beam launcher,” IEEE Trans. Antennas Propag., vol. 64, no. 3, pp. 904–913, Mar. 2016

[9] F. Benassi, W. Fuscaldo, D. Masotti, A. Galli and A. Costanzo, "Wireless Power Transfer in the Radiative Near-field Through Resonant Bessel-Beam Launchers at Millimeter Waves," *2021 IEEE Wireless Power Transfer Conference (WPTC)*, 2021, pp. 1-4, doi: 10.1109/WPTC51349.2021.9458226.

[10] Fuscaldo, W., Benedetti, A., Comite, D., Baccarelli, P., Burghignoli, P., & Galli, A. (2020). Bessel-Gauss beams through leaky waves: focusing and diffractive properties. *Physical Review Applied*, *13*(6), 064040.

[11] Lu, P., Voyer, D., Bréard, A., Huillery, J., Allard, B., Lin-Shi, X., & Yang, X. S. (2017). Design of TE-polarized Bessel antenna in microwave range using leaky-wave modes. *IEEE Transactions on Antennas and Propagation*, *66*(1), 32-41.

[12] Pfeiffer, C., & Grbic, A. (2014). Controlling vector Bessel beams with metasurfaces. *Physical Review Applied*, *2*(4), 044012.

[13] A. A. Oliner, “Leaky-Wave Antennas”, in *Antenna Engineering Hand- book*, R. C. Johnson, Ed., New York: McGraw-Hill, 1984, ch. 10

[14] F. Xu and K. Wu, "Understanding Leaky-Wave Structures: A Special Form of Guided-Wave Structure," in *IEEE Microwave Magazine*, vol. 14, no. 5, pp. 87-96, July-Aug. 2013, doi: 10.1109/MMM.2013.2259400.

[15] Walter Fuscaldo. Advanced radiating systems based on leaky waves and nondiffracting waves. Electronics. Université Rennes 1, 2017. English. NNT : 2017REN1S015 .

[16] D. R. Jackson, C. Caloz and T. Itoh, "Leaky-Wave Antennas," in *Proceedings of the IEEE*, vol. 100, no. 7, pp. 2194-2206, July 2012, doi: 10.1109/JPROC.2012.2187410.

[17] V.Rizzoli, A. Lipparini, «*Propagazione Elettromagnetica Guidata (Parte prima)»,* Esculapio.

[18] F. Benassi, F. Walter, N. Edoardo, P. Giacomo, A. Elisa, M. Diego, B. Paolo, G. Alessandro, and C. Alessandra, “Comparison between Hybrid and TM-polarized Bessel-beam launchers for wireless power transfer in the radiative near-field at millimeter waves,” in *Eur. Microw. Conf. (EuMC 2021)*, 2022, p. [Accepted paper]

[19] A. Costanzo *et al*., "Wireless Power Transfer for Wearable and Implantable Devices: a Review Focusing on the WPT4WID Research Project of National Relevance," *2021 XXXIVth General Assembly and Scientific Symposium of the International Union of Radio Science (URSI GASS)*, 2021, pp. 1-4, doi: 10.23919/URSIGASS51995.2021.9560425.

[20] W. Fuscaldo, “Rigorous evaluation of losses in uniform leaky-wave antennas,” *IEEE Trans. Antennas Propag.*, vol. 68, no. 2, pp. 643–655, Feb. 2020.

[21] A. Costanzo , D. Masotti , V. Rizzoli, and N. Arbizzani, "CAD procedure for predicting the energy received by wireless scavenging systems in the near- and far-field regions," *2010 IEEE MTT-S International Microwave Symposium*, 2010, pp. 1768-1771, doi: 10.1109/MWSYM.2010.5517916.

[22] Costanzo, Alessandra, et al. "RF/baseband co-design of switching receivers for multiband microwave energy harvesting." *Sensors and Actuators A: Physical* 179 (2012): 158-168.

[23] Chen, Z. N., Goh, C. K., & Qing, X. (2010, April). Loop antenna for UHF near-field RFID reader. In *Proceedings of the Fourth European Conference on Antennas and Propagation* (pp. 1-4). IEEE.

[24] P. V. Nikitin, K. V. S. Rao and S. Lazar, "An Overview of Near Field UHF RFID," *2007 IEEE International Conference on RFID*, 2007, pp. 167-174, doi: 10.1109/RFID.2007.346165.